Solar wind drivers of energetic electron precipitation

Josephine A. Salice

2020-06-16

Master Thesis in Space Physics

Supervisor: Dr. Hilde Nesse Tyssøy
Co-supervisor: Dr. Christine Smith-Johnsen

Department of Physics and Technology
University of Bergen

Abstract

Energetic electron precipitation (EEP) into the Earth's atmosphere can collide with gases and deposit their energy there. The collisions between electrons and atmospheric gasses initiate several chemical reactions which can reduce the ozone concentration. Ozone is critically important in the middle atmosphere energy budget as changes in the ozone concentration impact temperature and winds. EEP is not fully understood in terms of how much energy is being deposited and what the associated drivers are. An accurate quantification of EEP has limitations due to instrumental challenges and therefore imposes limitations of the associated EEP parameterization into climate models. A solution to this problem is a better understanding of the driver processes of energetic electron acceleration and precipitation, alongside optimized measurements. In this study the bounce loss cone fluxes are inferred from EEP measurements by the Medium Energy Proton and Electron Detector (MEPED) on board the Polar Orbiting Environmental Satellite (POES) and the Meteorological Operational Satellite Program of Europe (METOP) at tens of keV to relativistic energies. It investigates EEP in contexts of different solar wind structures: high-speed solar wind streams (HSSs) and coronal mass ejections (CMEs), as well as geomagnetic activity and energy transfer within the magnetosphere. The study is limited to the year 2010. CME- and CIR-driven geomagnetic storms have different effects on EEP where combined solar wind structures are most effective. Geomagnetic indices and their correlation to EEP is dependent on solar wind drivers. Generally the correlations are highest during CME-associated storms. The epsilon parameter alone is not sufficient in predicting EEP responses and the estimated energy lost through particle precipitation needs to be improved. Today's chemistry climate models and estimations of energy transfer and sinks only provide snapshots of EEP, independent of context. The results of this thesis suggest, however, that solar wind structures and pre-storm conditions must be taken into account to accurately predict EEP responses.

Acknowledgement

First and foremost, my gratitude goes to my supervisor and team leader of the particle precipitation group at BCSS, Hilde Nesse Tyssøy. Her door stood always open for advice and guidance, which without, this thesis would not have been possible. The many post-it notes were of great help.

I want to thank my co-supervisor, Christine Smith-Johnsen, who was extremely helpful with all Matlab-related issues. She kept me motivated and helped point me in the right direction when I found myself a bit lost. I would also like to thank Eldho for making every day at the office a laugh. To the other master students, especially Ingrid, thank you for the discussions (about everything and nothing) and for sharing both the ups and downs throughout this experience. To the entire Space Physics group, thank you for your kindness and warmth. You are all amazing.

I thank my family and friends, but especially my parents (all of you) for being my role models and for supporting me. I do not know what I would do without you. A special thanks to my mom, Sonia, who was there for me whenever I needed to discuss my thesis or just simply vent. I also want to thank Synøve for being a grammar police. All the love is highly appreciated.

For the data in this study I acknowledge OMNIWeb for solar wind and geomagnetic data, NOAA's National Geophysical Data Center for providing the NOAA particle data, Ian Richardson of the University of Maryland and NASA Goddard Space Flight Center for the solar wind classifications, the SuperMAG collaborators for the epsilon parameter, and the Heliospheric Shock Database, generated and maintained at the University of Helsinki, for the interplanetary shocks list.

Contents

1 Introduction

Breakthrough discoveries and sensational inventions throughout human history, from inventing the wheel to passenger-capable spacecrafts, have one very important thing in common: They are the result of curiosity. Curiosity is what drives us to seek new information and what leads us into the unknown. The greatest unknown, and cause of questions such as "are we alone?", is the boundless extent surrounding Earth, called Space. Though we might be far away from answering such questions, we do have the opportunity to learn more about near-Earth space. The relationship between Earth and Space is fundamental for the study of space weather and has important implications in not only understanding the universe, but also for practical everyday life, including the operations of communications and weather satellites, and atmospheric dynamics. In order to better understand the coupling of Earth to Space, the Birkeland Centre for Space Science (BCSS) has identified three ongoing areas of research: Dynamics of the asymmetric geospace, particle precipitation and hard radiation from thunderstorms. The topic of this thesis is particle precipitation.

The aurora is a spectacular phenomenon caused by energetic particles once originating from the Sun that end their journey by precipitating into the Earth's atmosphere and depositing their energy there. The dancing aurora visible on the polar night sky marks only the beginning of the effects particle precipitation has on the atmosphere. The context for this thesis goes beyond what first meets the eyes, namely the atmospheric chemical and dynamical impact of particle precipitation. Recently, it has become known that when energetic particles precipitate, they cause chemical changes in the upper atmosphere, e.g., the creation of NO_x and HO_x gasses. In particular, the increase of NO is important due to its long lifetime during high-latitude winter darkness which allows for downward transportation and depletion of stratospheric ozone. Ozone is known for its major role in stabilizing the Earth's radiation balance and climate system by absorbing incoming solar-wave and emitting long-wave infrared radiation. Changes in ozone will cause changes in the atmospheric temperature profile and lead to changes of atmospheric circulation that can map down onto surface climate. The strength of this effect is highly dependent on the number, type, and energy of the particles reaching the atmosphere.

Short term variations of the Earth's magnetic field, known as geomagnetic activity, have been studied since the mid-nineteenth century and is caused by interactions between the solar wind and its accompanied interplanetary magnetic field (IMF) and the Earth's magnetic field. This coupling leads to a transfer of energy from the solar wind, into the magnetosphere. The most severe disturbances of near-Earth space are predominantly driven by two types of solar wind structures: coronal mass ejections (CMEs) and corotating interaction regions (CIRs) and their associated high speed solar wind streams (HSSs). As the solar wind properties of CMEs and CIRs/HSSs are very different, so is the geomagnetic activity they drive. An important aspect of these space disturbances is the acceleration of charged particles to high energies in the inner magnetosphere. During periods of high geomagnetic activity, a vast number of energetic particles penetrate the Earth's atmosphere and deposit their energy by ionizing molecules. The relatively low energy particle precipitation ($< 30keV$) from the plasma sheet, which is known to cause aurora, has been extensively studied over the last century, while the more energetic electron precipitation (EEP) ($> 30keV$) from the radiation belts has been harder to capture due to limited knowledge and technical access. An illustration of the origin and precipitation of auroral and radiation belt electrons and the impact of particle precipitation on the atmosphere is presented in Figure 1.1.

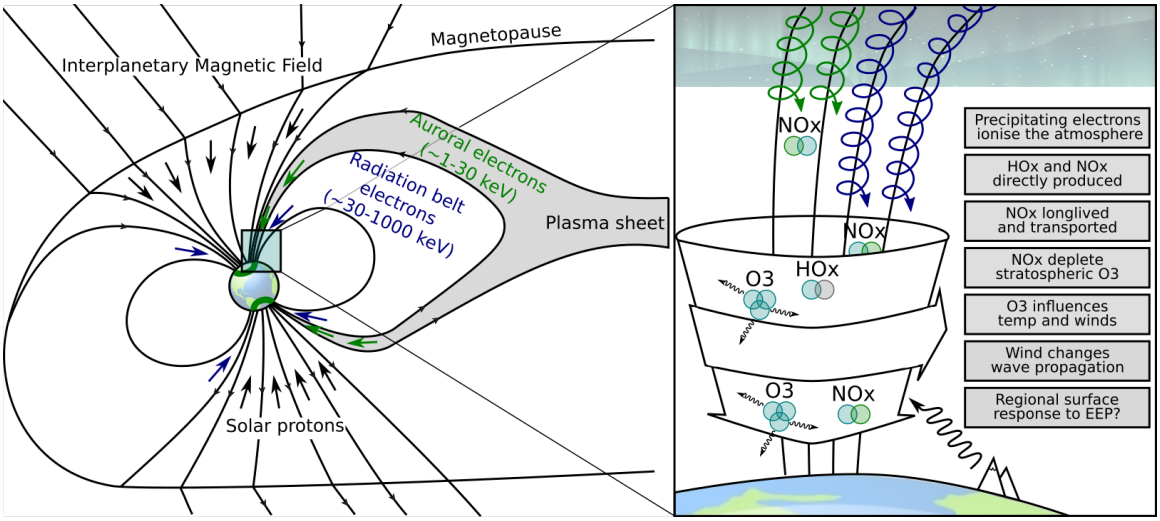

Figure 1.1: Magnetospheric electrons (auroral green and radiation belt blue) spiraling along Earth's magnetic field lines, precipitating into the Earth's atmosphere and ionizing it. The following chain of events are illustrated to the right. Based on *Thorne* [1980] (left) and *Seppälä et al.* [2014] (right), adapted by Linn-Kristine Glesnes Ødegaard and Christine Smith-Johnsen.

Knowledge of the characteristics of radiation belt EEP is important in order to quantify their impact on the middle atmosphere. While atmospheric climate models today typically predict EEP fluxes based on one geomagnetic index, this thesis aims to find more accurate predictors by looking at different solar wind structures, different geomagnetic indices and the energy budget in the magnetosphere. The following questions are addressed:

- To what extent do different solar wind structures (both isolated and combined CMEs and CIRs/HSSs) and their associated shocks affect EEP?
- How do geomagnetic indices predict EEP and is the correlation dependent on solar wind structure?
- How does the energy transfer to the magnetosphere and the distribution within scale to EEP variations?

The scope of this thesis is predicting how bounce loss cone EEP fluxes, measured by the Medium Energy Proton and Electron Detector (MEPED) on board the National Oceanic and Atmospheric Administration (NOAA)/Polar Orbiting Environmental Satellite (POES) and the European Organization for the Exploitation of Meteorological Satellites (EUMETSAT)/Meteorological Operational Satellite Program of Europe (METOP), respond to different solar wind structures, through looking at geomagnetic indices and energy transfer to and within the magnetosphere. The study is limited to the year 2010. We choose to study this year as it starts the inclining phase of solar cycle 24. This leaves storms driven by different solar wind structures occurring in 2010 relatively isolated which allows for examination of isolated features.

2 Theoretical Background

2.1 The Sun and the solar wind

The Sun is the Earth's main source of energy. The largest part of this energy comes in the form of solar radiation and sustains an inhabitable planet. A second part of the energy input from the Sun is in the form of a magnetized plasma, called the solar wind. Incoming particles from the solar wind and their effects on the atmosphere, climate, and technological systems are an important area of research.

2.1.1 Solar properties

The Sun is a yellow dwarf star located at the center of our solar system. It is a ball of gas consisting of $\sim$ 70.6% hydrogen and $\sim$ 27.4% helium as well as a small number of heavier elements. Its radius of roughly 700 thousand kilometers exceeds the Earth's radius by a factor of $\sim$ 100 and its volume is roughly 1.3 million times that of the Earth. The Sun is divided into six regions: the core, the radiative zone, the convective zone, the photosphere, the chromosphere, and the corona. The photosphere is known as the surface of the Sun and is where most of the solar energy escapes and is detected as sunlight.

The Sun rotates with an axial tilt of 7.25 degrees with respect to the plane of the planets' orbits. Because the Sun is not a solid body, the rotation rate differs with latitude. At the equator, the rotation rate is $\sim$ 25 Earth days, while at the poles the rotation rate is $\sim$ 36 Earth days. The Sun has a complex magnetic field that is generated by currents within the Sun. The difference in the Sun's rotation rate leads to a distortion of its magnetic field.

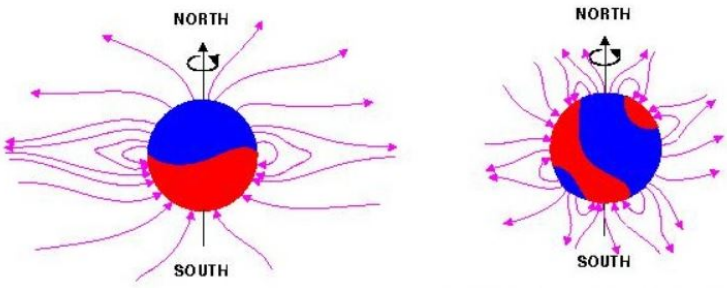

Figure 2.1: The solar magnetic field topology for solar minimum (left) and solar maximum (right). From [*Forsyth*, 2001]

The distortion of the Sun's magnetic field causes a change in solar activity that can be described by the solar cycle. Approximately every 11 years the Sun's geographic poles change their magnetic polarity. Throughout the solar cycle, the activity in the photosphere, chromosphere and corona goes from a quiet and calm state to a highly active one, and then relaxes back again. When the activity is at its lowest, it is known as the solar minimum. During solar minimum, the Sun's magnetic field resembles a dipole configuration. As the field becomes more and more distorted, the activity increases until it reaches its maximum level, known as solar maximum. It is worth noting that for the magnetic field configuration, a complete cycle would take 22 years, as solar maximum occurs with alternating magnetic polarity. A sketch of the Sun's magnetic field during solar minimum and solar maximum is shown in Figure 2.1. There are two types of magnetic field lines, open and closed. Open field lines are when the magnetic field only has one end attached to the Sun, and closed are when both ends are attached to the Sun.

2.1.2 Sunspots and coronal holes

Different phenomena that occur on the Sun are illustrated in Figure 2.2. Coronal holes occur in regions where the Sun's magnetic field lines are open to interplanetary space. When taking a soft x-ray or extreme ultraviolet image of the Sun, they are visible as large dark regions on the corona. The dark appearance is due to coronal holes being cooler and less dense than the surrounding plasma. The structure of the magnetic field lines allows solar wind to escape more readily into space, resulting in a relatively fast solar wind flow referred to as high speed solar wind streams (HSS). The size and number of coronal holes vary within the solar cycle where they are most common and persistent towards solar minimum. Persistent coronal holes can last long enough to reoccur during several solar rotations giving them a recurrence rate of ~ 27 days. Coronal holes typically cover large areas of the Sun's poles, but during the declining phase they often extend to low heliospheric latitudes [*Bame et al.*, 1976].

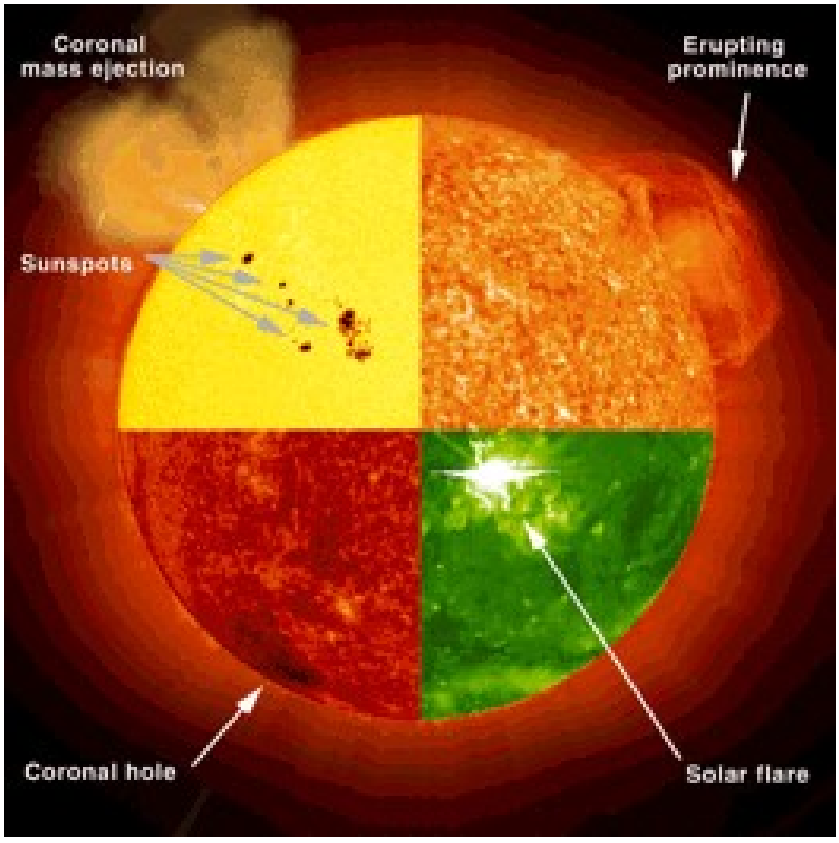

Figure 2.2: A composite image illustrating the different phenomena that occur on the Sun and that can result in geomagnetic activity on Earth: sunspots and a CME (top left), erupting prominence (top right), a coronal hole (bottom left), and a solar flare (bottom right). Courtesy of SOHO (NASA/ESA).

Towards solar maximum, the magnetic field flux increases around the equator due to the twisting of the Sun's magnetic field. The magnetic field lines may then bulge under the increasing pressure and extend through the photosphere. These concentrations of magnetic flux can be seen on the Sun's photosphere as dark spots known as sunspots. The darker color occurs because of reduced surface temperature due to the suppression of convection. The solar cycle is often quantified according to the sunspot number, also known as solar activity. This means that solar maximum is the point of highest sunspot activity, and the solar minimum is the point of lowest activity. Sunspots can last anywhere from a few days to a few months and are usually found moving towards the equator as

the cycle approaches maximum.

Sunspots, being regions with intense magnetic activity, can accompany secondary phenomena such as solar flares and coronal mass ejections (CME). When the magnetic pressure on sunspot field lines becomes too stressed, the field lines with opposite magnetic polarity will reconnect and reconfigure. This process is called magnetic reconnection and can result in a sudden release of electromagnetic energy known as a solar flare. Solar flares release photons in almost every wavelength of the spectrum and are observed as bright areas on the Sun [*Zell*, 2015a]. Primarily, solar flares are monitored in x-ray and optical light. Magnetic reconnection of the Sun's magnetic field lines can also result in an explosive acceleration of plasma and magnetic field from the corona known as CMEs. CMEs can also occur in regions where relatively cool and more dense plasma is trapped and suspended by magnetic flux extending up to the inner corona [*Zell*, 2015b]. As CMEs are closely related to sunspots, they occur most frequently during solar maximum.

2.1.3 The solar wind

The solar wind is a highly conducting plasma emitted from the Sun at supersonic speeds of about $500km/s$ [*Baumjohann and Treumann*, 1996]. It consists mainly of electrons and protons and is a result of the solar corona supersonic expansion [*Baumjohann and Treumann*, 1996]. Embedded in the solar wind is the Sun's magnetic field. The magnetic field is frozen into the plasma due to the high conductivity and is drawn outward into interplanetary space by the solar wind. The interplanetary magnetic field (IMF) is of the order of $5nT$, and typical values for the electron density and temperature in the solar wind near Earth are $n_e \approx 5cm^{-3}$ and $T_e \approx 10^5 K$ [*Baumjohann and Treumann*, 1996].

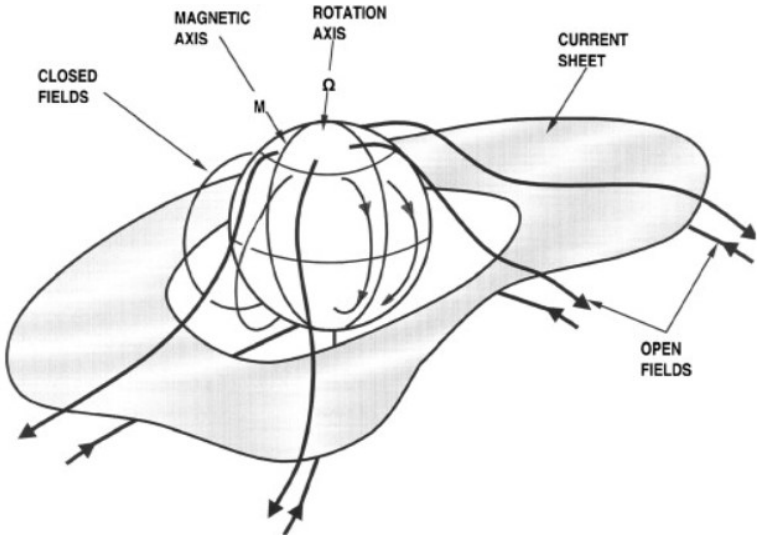

Figure 2.3: Schematic of magnetic field lines and the Heliospheric current sheet near the Sun. From *Smith* [2001]

The heliospheric current sheet (HCS) is defined as the boundary encircling the Sun that separates opposite directed open magnetic field lines that originate from the Sun [*Smith*, 2001]. It is a distinctive feature of the solar wind and its properties. An illustration of the HCS is shown in Figure 2.3. There could be several current sheets surrounding the Sun, but because the underlying heliospheric magnetic field is dipole-like, the HCS is unique and represents the magnetic equator of the global heliosphere [*Smith*, 2001]. Due to the Sun's rotation and rotation axis, the IMF embedded in the solar wind gets wrapped into Archimedes spirals and oscillates about the heliographic equator

forming a series of peaks and troughs. In three dimensions the HCS resembles a "ballerina skirt" as shown in Figure 2.3.

The geocentric solar magnetospheric coordinate-system (GSM-system) is a coordinate system used when studying the effects of the IMF and solar wind on the terrestrial field. It is oriented with the x-axis pointing from the center of the Earth to the center of the Sun, the z-axis along the magnetic dipole axis pointing north, and the y-axis pointing in the opposite direction of the Earth's orbit around the Sun. An illustration of the GSM coordinate system is shown in Figure 2.4.

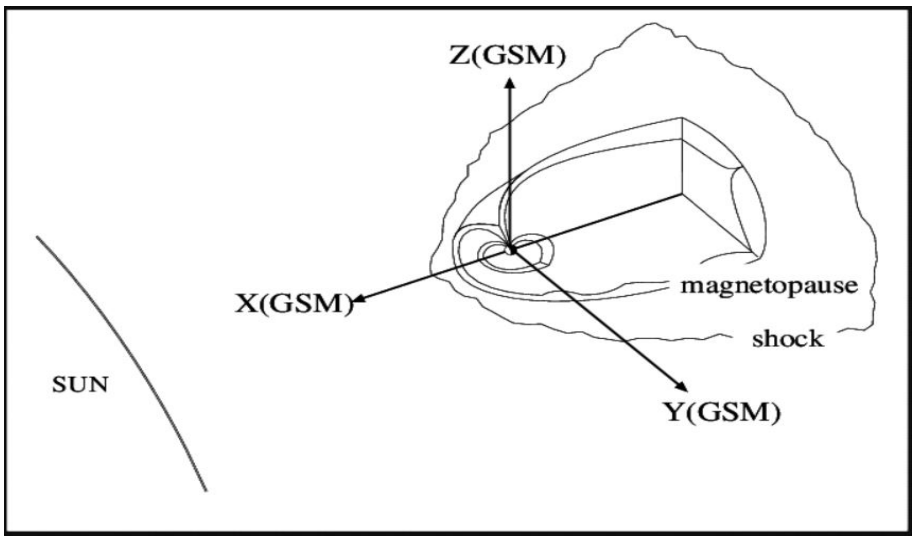

Figure 2.4: An illustration of the geocentric solar magnetospheric coordinate-system (GSM-system). From *Tanskanen and Ilmatieteen laitos (Finland)* [2002].

2.2 The magnetosphere

To understand how solar activity affects the Earth, the interaction between the solar wind and IMF with the Earth's magnetic field is a key factor. This section will focus on near-Earth space and aim to describe this interaction and some of the processes that result thereafter, e.g., the convection of plasma and particle precipitation.

2.2.1 The geomagnetic field

The Earth's magnetic field, known as the geomagnetic field or terrestrial field, is generated in the Earth's interior and extends out into space. The processes in the core are best described by the dynamo model where mechanical energy is converted to electrical energy [*Carrigan and Gubbins*, 1979]. The model describes how an electrically conductive fluid can generate a long-lived magnetic field in astrophysical bodies through convection, rotation, gravity, and magnetism [*Carrigan and Gubbins*, 1979]. When considering the Earth, this fluid is liquid iron in the Earth's outer crust. The field generated can, as an approximation, be modeled as a dipole field.

The dipole model of the Earth's magnetic field is only valid for low L-shell values. The L-shell parameter or L-value is described as the radial distance to a specific field line in the Earth's equatorial plane, r_{eq}, divided by the Earth's radius, $R_E = 6371km$:

$$L = \frac{r_{eq}}{R_E} \tag{1}$$

[*Baumjohann and Treumann*, 1996]. The field lines loop around the Earth, diverging near the Geographic South Pole and converging near the Geographic North Pole. Therefore, the North Magnetic Pole roughly corresponds to the South Geographic Pole and vice versa. The magnetic axis is tilted compared to the rotational axis at an angle of about 11°. The magnetic poles are defined as the location where the inclination of the magnetic field lines are at a 90° angle downward or upward depending on if the measurements are done at the North or South Magnetic Pole, respectively. It can also be defined using a mathematical model, where a line through the center of the Earth parallel to the best fitting magnetic dipole is used to find the two poles. The two magnetic poles are not directly opposite each other and asymmetries do occur.

2.2.2 Energy transfer to the magnetosphere

The Earth's magnetic field works as a shield against the solar wind. The topography of the solar-terrestrial environment is shown in Figure 2.5. When the supersonic solar wind hits the terrestrial magnetic field, a bow shock is generated where the plasma is slowed down, and a considerable amount of the particles' kinetic energy is converted into thermal energy [*Baumjohann and Treumann*, 1996]. Behind the bow shock is a region called the magnetosheath. The plasma in the magnetosheath is denser, hotter and with higher magnetic field values compared to the solar wind plasma [*Baumjohann and Treumann*, 1996].

The solar wind in the magnetosheath is mostly deflected around the terrestrial magnetic field leaving a cavity called the magnetosphere (see Figure 2.5). The boundary between the magnetosheath and the magnetosphere is called the magnetopause. The occurrence of this cavity is due to the IMF lines, and the solar wind particles that are frozen into it, not being able to penetrate the terrestrial field lines. The kinetic pressure from the solar wind plasma leads to a distortion of the terrestrial dipolar field. On the day-side, the terrestrial field is compressed while on the night-side it is stretched out into a long magnetotail (see Figure 2.6).

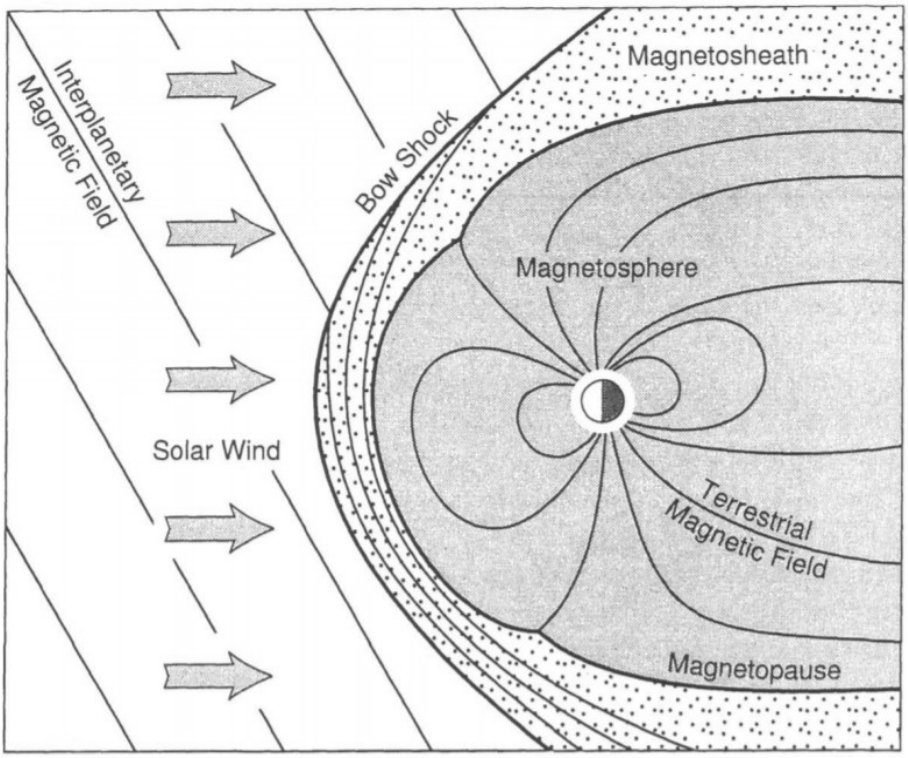

Figure 2.5: Topography of the solar-terrestrial environment. From *Baumjohann and Treumann* [1996]

2.2.3 The convection of plasma

The drift of the plasma and magnetic field lines is often called convection [*Baumjohann and Treumann*, 1996]. The main source of magnetospheric convection is the solar wind flow. When the IMF has a southward component, reconnection between the IMF and the day-side terrestrial field occurs. The merging, reconnection, and convection of the IMF and terrestrial field is sketched in Figure 2.6. The southward directed IMF, denoted by (1), merges with the terrestrial field line (1) which has both footpoints on Earth and is being transported towards the magnetopause. As the two field lines merge and reconnect, they will split into two open field lines marked by (2). These field lines have one footpoint on Earth and one stretching out into the IMF.

The footpoints of the open field lines lie in the ionosphere. Here conductivity is high and mobility of the field lines low due to friction by collisions with local ions. The open field lines are bent towards the night-side due to the solar wind flow (visible in points (5) and (6)). When the magnetic stress of the curvature exceeds the friction in the ionosphere, the footpoint of the magnetic field lines will be dragged towards the night-side.

Far out on the night-side, around $100 - 200R_E$, the open field lines will meet and reconnect again. This leaves a closed but stretched terrestrial field line and an open solar wind field line down-tail of the magnetosphere (both denoted by (8)). The stretched terrestrial field line will start to relax back towards Earth and into a more dipolar-like structure due to the magnetic tension in the stretched tail. As this happens the footpoints on Earth will move towards lower latitudes. The plasma is still frozen into the magnetic field, meaning the transport of plasma follows the relaxation of the magnetic field lines. Eventually, the field lines will be transported back to the day-side magnetosphere and replace the terrestrial field lines there. This cycle, often referred to as the Dungey cycle, can then be repeated provided that the IMF has a southward component.

The magnetic field depicted in Figure 2.6 is a simple model used to describe the interaction between the IMF and the terrestrial field. In reality, the day-side magnetic field is confined to about $10R_E$, while the night-side stretches out to hundreds of R_E. The reconnection rate and efficiency of energy transfer are highest during strong southward IMF, but reconnection can also happen with northward IMF at higher latitudes [*Onsager et al.*, 2001]. Asymmetries of the terrestrial field occur due to the tilt of the dipole axis with respect to the ecliptic plane and the angle at which the solar wind hits the bow shock. This means that the convection of plasma in the magnetosphere is much more complicated.

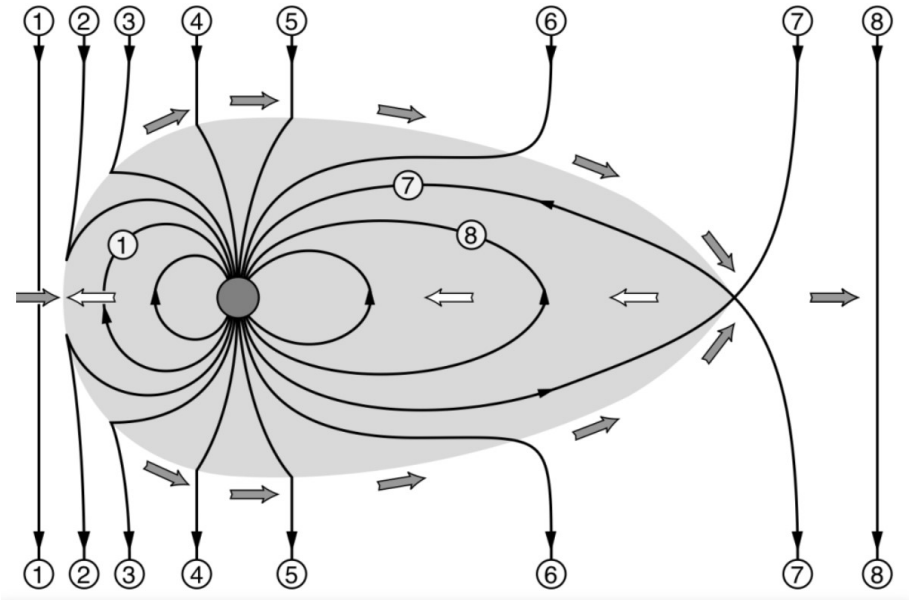

Figure 2.6: Sketch of the merging, reconnection and convection of the IMF and terrestrial magnetic field. The numbers indicate the movement of a magnetic field line. From *Baumjohann and Treumann* [1996]

2.2.4 The radiation belts

The plasma in the magnetosphere consists mainly of electrons and protons originating from the solar wind and the terrestrial ionosphere. It is also possible to find small fractions of He^{++} ions, originating from the solar wind, and He^{+} and O^{+} ions of ionospheric origin [*Baumjohann and Treumann*, 1996]. The plasma inside the magnetosphere is not evenly distributed and is therefore grouped into different regions with different densities and temperatures. Figure 2.7 shows some of these regions and currents.

The plasmasphere is the closest region to Earth. It contains a cool/low-energy, dense plasma. The particles found in the plasmasphere originate from the top of the Earth's atmosphere and are trapped on closed and almost dipolar magnetic field lines. The outer boundary of the plasmasphere is called the plasmapause and extends out to about $4R_E$ [*Baumjohann and Treumann*, 1996].

The radiation belts, or the Van Allen belts, are regions where energetic charged particles are trapped in the Earth's magnetic field [*Horne et al.*, 2005]. The radiation belts are separated into two regions known as the inner and outer radiations belts. The inner radiation belt is embedded in the plasmasphere and is stable on long time scales. It mainly consists of trapped high-energy protons between $0.1 - 40MeV$, where the maximum flux is found around $2R_E$. The outer radiation belt is

dominated by electrons ranging from hundreds of keV to more than $10MeV$. It is highly variable in location and intensity, but the inner edge is approximately at the same location as the plasmapause. The approximate locations of the radiation belts and plasmapause are shown in Figure 2.8. The inner and outer radiation belts map down to $\sim 60° - 75°$ and $\sim 45° - 55°$ geomagnetic latitude, respectively. The shaded region in the figure illustrates the plasma sheet, which is where most of the magnetotail plasma is concentrated. Low-energy particles precipitating from this region down into the Earth's atmosphere can produce aurora.

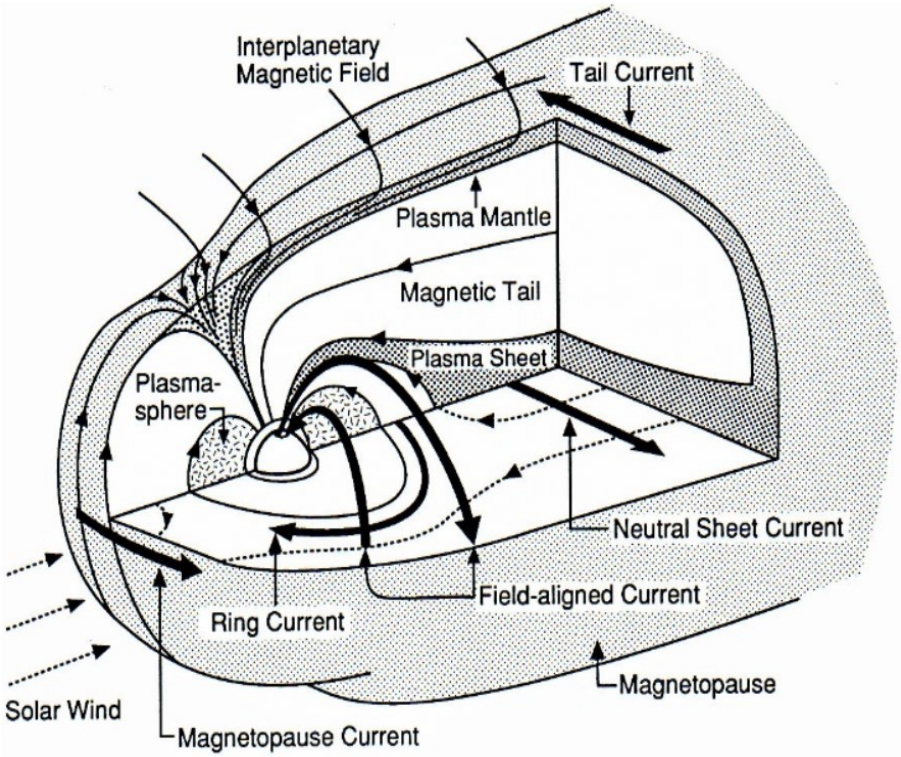

Figure 2.7: Display of currents and plasma regions in the magnetosphere adapted from *Russell* [1993].

The trapped energetic electrons and ions in the radiation belts move in three ways; they gyrate around the magnetic field line; they oscillate back and forth, or bounce, between the two hemispheres along the field line; and they drift around the planet on paths of constant magnetic field strength. Associated with each type of motion adiabatic invariants are defined. The gyration of the particles is associated with the magnetic momentum, the bounce motion with the longitudinal invariant, and the drift with the drift invariant. The drift of the particles around the Earth is due to the increasing gradient in the terrestrial magnetic field as the particles accelerate from the night-side reconnection towards the planet. The gradient drift causes the electrons to drift eastward and ions westward. The opposite drift directions of the electrons and ions lead to a current known as the ring current (see Figure 2.7) [*Baumjohann and Treumann*, 1996]. Adiabatic invariants are not absolute constants but may vary in both space and time. If the magnetic field is constant or close to constant within the time scale of the motion of the particles, the invariant is conserved. Violation of one or more of the adiabatic invariants can cause either a change in the pitch angle or acceleration of the particles.

Trapped particles bouncing between Earth's two hemispheres can be lost by collisions with neutrals in Earth's atmosphere if their mirror points lie below about $100km$ [*Baumjohann and Treumann*, 1996]. A key factor in determining whether a charged particle will be lost to the Earth's atmosphere is its pitch angle. A particle's pitch angle is the angle between the particle's velocity vector and the local magnetic field. A pitch angle of $0°$ is a particle whose parallel motion is along the magnetic

field line, while a particle with a pitch angle of 90° is a particle that is locally mirroring. Particles that are lost to the Earth's atmosphere must have equatorial pitch angles that fall within a solid angle known as the equatorial loss cone (see Figure 2.9). The width of the loss cone is a function of the field line radius. The loss of particles to the Earth's atmosphere is referred to as particle precipitation or that the particles precipitate.

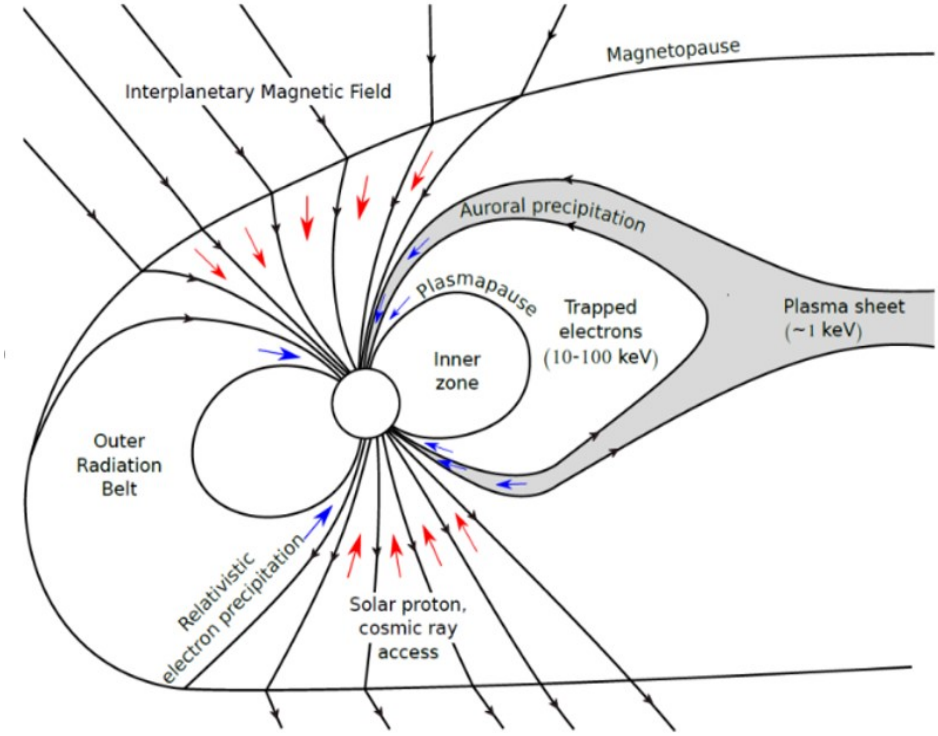

Figure 2.8: Illustration of the magnetosphere and dominant zones of particle precipitation adapted. From *Thorne* [1980] adapted by Linn-Kristine Glesnes Ødegaard.

The properties of the charged particles in the radiation belts vary according to solar activity. However, the very high energies, of several million eV, of the particles cannot be explained by solar wind activity alone. The particles are accelerated in the radiation belts. Variations in the radiation belt electrons are dependent on source and loss processes. These processes are caused by a violation of at least one of the adiabatic invariants associated with energy and momentum transfer during interactions with magnetospheric waves. Precipitation occurs when particles are scattered into the atmospheric loss cone. The scattering of keV to MeV electrons can be caused by different plasma waves: plasmaspheric hiss found inside the plasmasphere, whistler-mode chorus found outside the plasmasphere, and electromagnetic ion cyclotron (EMIC) waves found near dusk [*Millan and Thorne*, 2007]. The spatial distribution of these important inner magnetospheric waves is illustrated in Figure 2.10. The plasma waves are generated by instabilities in the plasma which redistributes free energy in the system. The disturbance is often associated with, e.g., a density gradient, temperature gradient, magnetic fluctuations, or pitch angle anisotropy [*Ødegaard et al.*, 2017]. During disturbed geomagnetic conditions plasma wave generation is naturally enhanced and particle precipitation is increased [*Ødegaard et al.*, 2017].

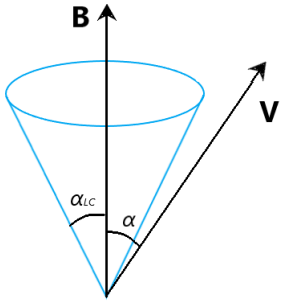

Figure 2.9: Illustration of the velocity, V, of a particle and its pitch angle α, relative to the magnetic field line B. Particles with pitch angles within the loss cone, $\alpha \leq \alpha_{LC}$, will be lost to the atmosphere.

Whistler-mode Chorus

The magnetosphere is predominantly collision-less which allows electromagnetic waves traveling through the plasma to interact with free charges. Electromagnetic waves, having both electric and magnetic fields, will attract/repel these charged particles and thereby changing their trajectories. Depending on the interactions, the waves will either lose energy to the particles and be damped, or extract energy from the particles and therefore be amplified. A common wave mode that is amplified by the plasma is the whistler-mode wave. These waves are right-hand circularly polarized electromagnetic waves, meaning that they are in a polarization state in which, at each point, the electromagnetic field of the wave has a constant magnitude while it's direction rotates at a constant rate in a plane perpendicular to the direction of the wave. These waves propagate at frequencies less than the local gyrofrequency. The plasma in the radiation belt can strongly and non-linearly amplify whistler-mode waves. The unstable system generates bursts of whistler-mode waves, known as chorus, that consist of ~ 0.1 second burst of electromagnetic waves.

Whistler-mode chorus waves occur in two distinct bands above and below 0.5 of the electron gyrofrequency [*Thorne*, 2010] and are believed to be generated by the electron-cyclotron instability near the equator which is associated with freshly injected plasma sheet electrons [*Millan and Thorne*, 2007]. Chorus waves are important because they are responsible for both loss and local acceleration of radiation belt electrons and are the dominant source of scattering processes leading to diffuse auroral precipitation [*Thorne*, 2010]. During enhanced substorm activity and the recovery phase of magnetic storms, the chorus intensity increases and is often most effective between 0300 and 1500 MLT (magnetic local time), accounting for significant losses [*Millan and Thorne*, 2007].

Plasmaspheric hiss

Plasmaspheric hiss is a broadband extremely low frequency (ELF) ($100Hz-$ few Hz) whistler-mode emission that is most intense between 0600 - 2100 MLT [*Millan and Thorne*, 2007]. The source of plasmaspheric hiss is not fully understood. Observations have indicated that lightning-generated whistlers may be a source, particularly at low L-values [*Millan and Thorne*, 2007]. However, *Millan and Thorne* [2007] also state that the stronger hiss emissions show no relationship to lightning and that their substorm dependence more likely supports a magnetospheric source. Plasmaspheric hiss is the mechanism that is primarily responsible for the formation of the slot region by pitch-angle scattering and dominates the loss processes in the outer portion of the slot region [*Millan and Thorne*, 2007]. The slot region can be partially filled with relativistic electrons during large storms and due to resonant interactions with hiss, the flux at $\sim MeV$ decays over a relatively long timescale

($\sim 10 - 100 days$) leading to well-defined loss cone distributions [*Millan and Thorne*, 2007].

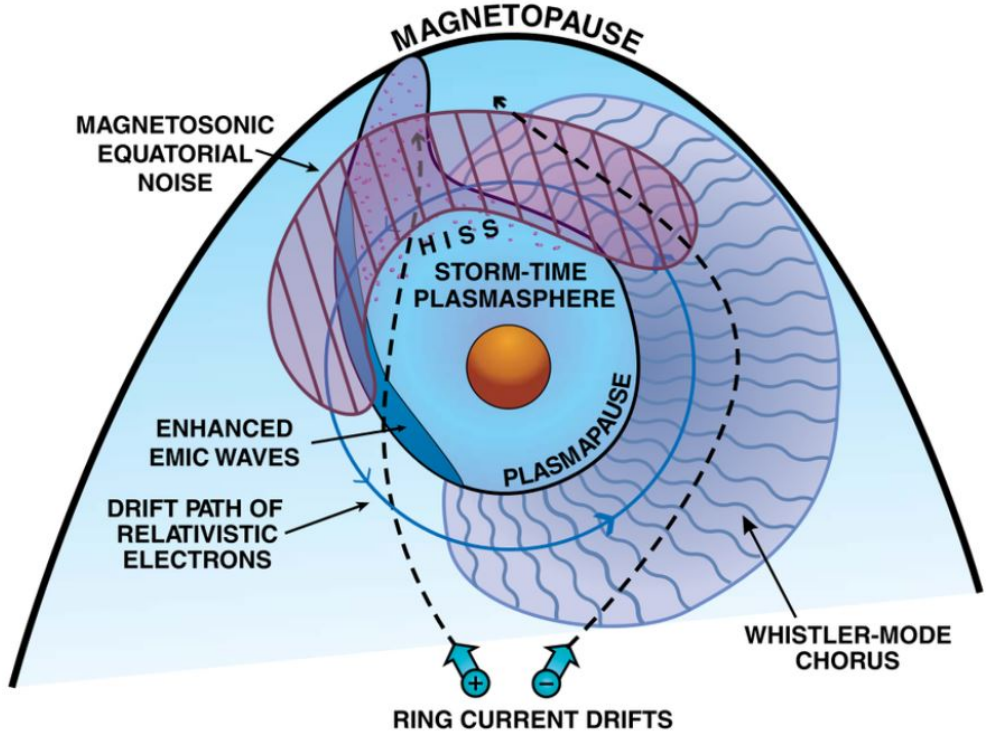

Figure 2.10: Schematic illustration of the spatial distribution of important waves in the inner magnetosphere. Source: [*Thorne*, 2010]

EMIC Waves

EMIC waves are discrete electromagnetic emission propagating at frequencies below the proton gyrofrequency. The source region for EMIC waves occurs near the equator where they are thought to be driven by the injection of ions from the ring current during magnetic storms [*Millan and Thorne*, 2007; *Thorne*, 2010]. EMIC waves usually occur on the dusk and day-side at high L-shells during high magnetic activity. The scattering by EMIC waves is expected to be very strong in a limited range of MLT near dusk [*Millan and Thorne*, 2007]. Observations have shown a distinct class of precipitation in these regions [*Millan and Thorne*, 2007].

2.2.5 Energy transfer within the magnetosphere

Energy from the solar wind can be transferred into the magnetosphere and then dissipated by several different processes in both the ionosphere and the magnetosphere. The energy input is described by a function depending on solar wind parameters and is a proxy for when and how the magnetosphere couples with the solar wind. The most important forms of ionospheric and magnetospheric energy dissipation are auroral particle precipitation (U_A), Joule heating of the atmosphere (U_J), and energy increase of the ring current U_R) [*Akasofu*, 1981], all of which can be estimated using ground-based magnetometer data. The energy budget can be evaluated by comparing energy sinks and sources [*Østgaard et al.*, 2002a].

Energy source

The IMF is a three-dimensional vector with components Bx, By, and Bz. When Bz has a negative orientation the coupling to the terrestrial field is strongest due to optimized re-connection conditions as Bz then points in the opposite direction of the terrestrial field. A commonly used estimation of the energy input from the solar wind to the magnetosphere can be calculated by using the *Akasofu* [1981] epsilon parameter, given in SI units by *Koskinen and Tanskanen* [2002]:

$$\epsilon[W] = \frac{4\pi}{\mu_0} V B^2 sin^4(\frac{\theta}{2}) l_0^2 \tag{2}$$

where $\frac{4\pi}{\mu_0} = 10^7$, V is the solar wind velocity, B is the total solar wind magnetic field, θ is the angle between the IMF vector and the Z-axis, projected into the GSM Y-Z plane, also known as the clock angle ($tan\theta = \frac{B_y}{B_z}$), and $l_0 = 7R_E$. Epsilon is measured in watt or, if accumulated over time, in joule.

Energy dissipation

As particles precipitating through ionization into the Earth's atmosphere result in disturbances of ionospheric currents which further affect the terrestrial field, the amount of energy dissipated due to auroral electron precipitation (U_A) is believed to be related to the AE (or AL) indices [*Akasofu*, 1981] described in section 2.4.1. This energy can be estimated with a nonlinear function of the form:

$$U_A[GW] = aAE^n + b, \tag{3}$$

where a, b, and n are constants, often with different values depending on the study. The constant b indicates that currents are flowing in the ionosphere even when there is no precipitation.

As mentioned in section 2.2.3, the open terrestrial magnetic field lines, having footpoints in the ionosphere, experience friction due to collision with ionospheric ions. This friction causes loss of energy due to heating, known as Joule heating (U_J). The energy dissipated through Joule heating has been found to closely relate to the AE index [*Akasofu*, 1981]. Different results may be applied for estimating the Joule heating from the AE index, but all are in the form:

$$U_J[GW] = aAE + b. \tag{4}$$

Different studies have arrived at different a and b values.

Particle injections from Earth's magnetic tail can lead to intensification of the ring current. The energy diffusion due to the ring current can be estimated using the Dst index described in section 2.4.1. The Dst index is sensitive to the ring current strength, which induces an additional horizontal magnetic field in the equatorial region. It is also sensitive to magnetopause currents, which occur due to day-side magnetosphere compression. A pressure corrected Dst index is therefore needed to get a more realistic value of the ring current. To estimate the ring current energy injection rate the empirical equations from *Akasofu* [1981] is commonly used:

$$U_R[GW] = -4 * 10^4(\frac{\delta Dst*}{\delta t} + \frac{Dst*}{\tau}), \tag{5}$$

where Dst* is the pressure corrected Dst and τ is the ring current particle lifetime in seconds.

The pressure corrected Dst is given by:

$$Dst * [nT] = Dst - \Delta H. \tag{6}$$

The pressure correction terms ΔH, adopted from *Siscoe et al.* [1968], used by *Akasofu* [1981], and updated by *Gonzalez et al.* [1994, & references therein], is given in SI units as:

$$\Delta H[nT] = 5 * 10^5 \frac{nT}{(Jm^{-3})^{\frac{1}{2}}} P^{\frac{1}{2}} - 20nT, \tag{7}$$

where P is the solar wind dynamic pressure or plasma flow pressure.

As energy must be conserved in a closed system, the energy coming into the system should equal the energy being lost. The total energy dissipation rate U_T is defined as the sum of particle precipitation, Joule heating, and ring current injections:

$$U_T \approx U_A + U_J + U_R. \tag{8}$$

It is expected that U_T approximately equals the estimated input energy as it includes the three most important energy sinks.

2.3 Earth's atmosphere

Solar variations present a driver for both global and local terrestrial climate variability. In this section, a brief introduction to the Earth's atmospheric structure is presented along with the main sources of solar forcing: total solar irradiance, solar spectral irradiance, and energetic particle precipitation.

2.3.1 Atmospheric structure

Earth's atmosphere is divided into a series of different layers each with their own traits. The separation of the different layers is based on the mean temperature gradient as it varies with altitude. Figure 2.11 illustrates the atmospheric temperature profile.

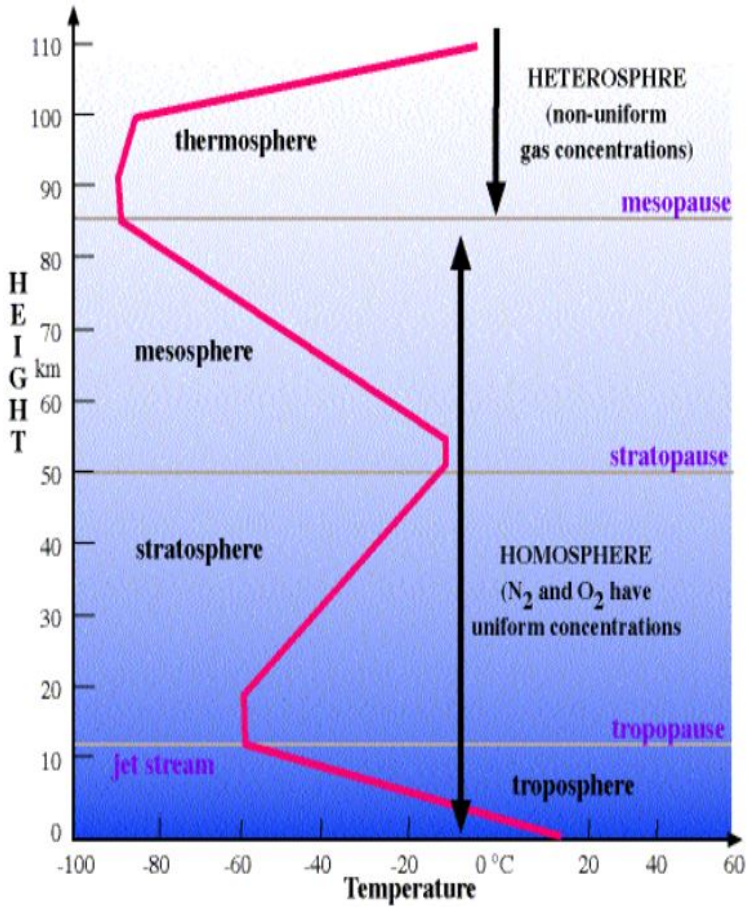

Figure 2.11: The temperature profile of the standard Earth atmosphere and the composition regions with respect to altitude.

The lowest layer is the troposphere. It extends to about $10km$ altitude and is where most weather phenomena occur. Characteristically the temperature in the troposphere decreases up to its boundary layer, called the tropopause. It is strongly affected by the Earth's surface properties and is highly variable on short time scales [*Smith*, 2012]. From the tropopause, up to about $50km$, the temperature profile starts to increase due to UV absorption by, e.g., ozone. This region is known as the stratosphere. Above the stratosphere is a region that extends up to about $85km$ called the

mesosphere. The temperature in the mesosphere decreases with altitude. The thermosphere is the region above the mesosphere. In this region, high-energy X-rays and UV radiation from the Sun are absorbed and lead to an increase in the temperature. The amount of energy absorbed from the Sun varies and because the absorption has a great influence on both the temperature and altitude of which the thermosphere reaches, the top of the thermosphere can be found anywhere between $500 - 1000km$.

The composition of the atmosphere can be divided into two regions; the homosphere and the heterosphere. The homosphere extends up to about $100km$ and consist of a homogeneous mixture of the atmospheric species found in this region. Chemically, the homosphere is composed of 78% nitrogen, 21% oxygen, and a trace of other molecules such as argon and carbon dioxide. The effective mixing of molecules in the homosphere has one large exception, the ozone layer. The ozone is mainly found in the lower part of the stratosphere at approximately $15 - 35km$. The temperature of the stratosphere is highly affected by the amount of ozone that is there. The absorption of high-energy UV radiation from the Sun by the ozone molecules functions as a shield against UV radiation penetrating further down into the atmosphere and is what causes the temperature increase in the stratosphere. Solar activity is therefore important for the chemical system in the stratosphere [*Smith*, 2012]. Ozone also radiates long wave radiation and is henceforth, a cooling factor in the dark winter polar stratosphere.

The heterosphere begins at about $100km$ and extends out to the outer regions of the Earth's atmosphere. In this layer, the gases are separated by molecular diffusion with increasing altitude which leads to a separation between heavier and lighter species. The heavier molecules (nitrogen and oxygen) tend to be present at lower altitudes compared to the lighter molecules (hydrogen and helium) usually found higher up. The density of the heterosphere is not entirely dependent on temperature due to its diffuse nature. Contributions to the density variations include day and night cycles, solar activity, and geomagnetic activity [*Jacchia*, 1965].

2.3.2 Solar forcing

Total solar irradiance (TSI) is the main source of solar forcing into the Earth's atmosphere [*Seppälä et al.*, 2014]. It is the value of the integrated solar energy flux over the entire spectrum that arrives at the top of the terrestrial atmosphere at the mean Sun-Earth distance and provides the energy needed for the climate system [*Seppälä et al.*, 2014]. It impacts the Earth's surface directly and influences the atmosphere above by the bottom-up mechanism [*Seppälä et al.*, 2014] described below. TSI is directly correlated to the Sun's activity.

Solar spectral irradiance (SSI) is a solar forcing that varies in a much larger degree with the solar cycle compared to TSI [*Seppälä et al.*, 2014]. SSI affects the atmospheric dynamics by heating the middle atmosphere and by interacting with ozone. It is one of the main drivers in the top-down mechanism [*Seppälä et al.*, 2014]. The top-down mechanism connects the stratosphere to the climate in the troposphere and surface. It originates where UV radiation heats the stratopause in the tropics, where it also affects the increase in ozone production. This heating in the equatorial plane affects the equator-to-pole, or meridional, temperature gradient [*Seppälä et al.*, 2014]. Thermal winds occur to stabilize the temperature gradient which results in modulation of the zonal wind. This is usually a west wind anomaly in the upper stratosphere [*Seppälä et al.*, 2014]. These winds can affect planetary waves which in turn can affect the tropospheric circulation patters and therefore the temperature on the surface.

Energetic particle precipitation (EPP) (protons and electrons) are guided into the Earth's polar atmosphere by the Earth's magnetic field lines. The precipitating electrons undergo a variety of inelastic collisions, including collisions that produce secondary electrons. The nominal penetration depth of electrons as a function of energy is illustrated to the left in Figure 2.12. The energy is not dissipated uniformly along with its range. As the atmospheric density increases with depth, the

different electron energies have a sharp lower altitude boundary as shown to the right in Figure 2.12. The precipitating electrons not only ionize the different atmospheric species but also dissociate and excite them. This affects the chemical reaction rates in the atmosphere. In particular, precipitating electrons produce odd hydrogen HO_x and odd nitrogen NO_x species in the upper atmosphere. These gasses have an important role in middle atmospheric ozone balance, which could influence the meridional temperature gradient, winds, and wave propagation. Hence, it also provides a potential Top-Down link between the atmospheric dynamics and regional climate [*Seppälä et al.*, 2014].

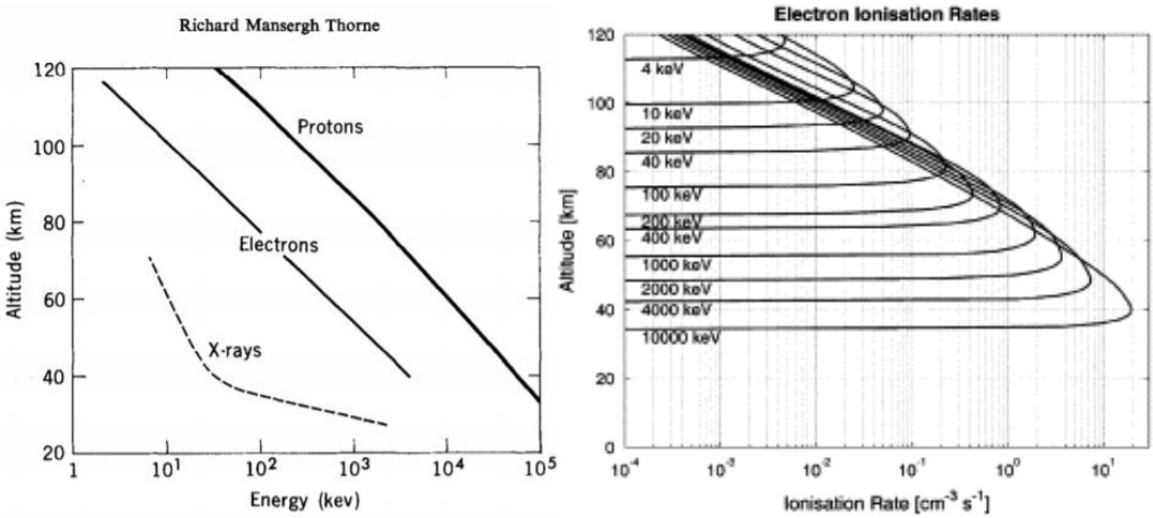

Figure 2.12: To the left: The nominal penetration depth of electrons and protons as a function of energy (from [*Thorne*, 1980]). To the right: the electron Ionization rate (from [*Turunen et al.*, 2009])

2.4 Geomagnetic storms

Short-term variations of the Earth's magnetic field, known as geomagnetic activity, are mainly due to the solar wind and interplanetary magnetic field. This coupling enables energy transfer from the ambient solar wind to the magnetosphere and drives different current systems in the magnetosphere and ionosphere [*Holappa et al.*, 2014]. These currents produce magnetic disturbances that can be measured on ground based magnetometers. As well as intensifying currents, geomagnetic storms may lead to dramatic changes in the relativistic electron fluxes in the Van Allen radiation belts [*Kilpua et al.*, 2017a]. Geomagnetic storms can last from hours to weeks and are responsible for the most severe space weather.

2.4.1 Geomagnetic indices

AE index

The AE (Auroral electrojet) index is derived from geomagnetic variations in the horizontal component of the Earth's magnetic field observed by up to 13 observatories along the auroral zone in the Northern Hemisphere [*Kyoto*, 2020a; *NOAA*, 2020]. The index is based on normalized data for each of the observatories. The base value for a specific observatory is calculated for each month by averaging all the data from that observatory on the five quietest days [*Kyoto*, 2020a]. The base value is then subtracted from each value of one-minute data obtained at that specific observatory during that same month [*Kyoto*, 2020a]. The largest and smallest values among the data from all the observatories at a given time (UT) are then selected to represent the AU and AL indices, respectively. The AU index can be used as an approximation of the strongest current intensity of the eastward auroral electrojet while the AL index represents the same just for the westward electrojet. The difference in the AU and AL indices defines the AE index: $AE = AU - AL$. The AE index represents the overall activity of the electrojets [*Kyoto*, 2020a].

The AE index has limitations. The eastward and westward electrojets do not necessarily increase and decay coherently and the currents measured may also be significantly separated in local time. This means that the AE does not reflect the total current flowing in the Northern Hemisphere. Therefore, it is questioned to which degree the AE index can be used as an approximation for the overall activity of the electrojets *Kamide and Rostoker* [2004].

Other problems that can occur are due to the location of the observatories used to derive the AU and AL indices. These two electrojet indices are well suited to give an overview of the current intensity in the auroral electrojets in moderate storms. Problems can occur when storms are either relatively weak or relatively strong. If a storm is weak, the variations in the electrojets might be too small for the observatories to detect. It is also possible that the small enhancements occurring during a weak storm are located in a narrow local time sector falling between observatories. Weak storms can, therefore, lead to underestimated values. During stronger storms, the electrojets may expand so far south that all the observatories used to find the AU and AL indices are too far north to detect the magnetic field from these currents. Again, the AU and AL indices will underestimate the maximum strength of the auroral electrojets.

Kp and ap indices

The Kp index describes the global geomagnetic activity by using three-hour measurements of the horizontal component of Earth's magnetic field from ground-based magnetometers around the world [*SpaceWeatherLive*, 2020]. The observatories each find a K-index ranging from 0 to 9 that describes the geomagnetic activity at a given location and time compared to a calm day curve. The digits

assigned to the K-index from the different observatories are chosen so that every observatory has approximately the same frequency distribution of K-indices. This means that observatories located near the auroral zones will need higher levels of fluctuations to reach a certain K-index level compared to observatories located in lower latitudes. The K-index is a three-hour-long quasi-logarithmic local index of the geomagnetic activity at a given observatory [*SpaceWeatherLive*, 2020].

The Kp index is derived by an algorithm that uses all the reported K-values from the different observatories so that it also ranges from 0 to 9. A value of 0 corresponds to little global geomagnetic activity and a value of 9 would correspond to extreme geomagnetic disturbances. Because the K-scale is a non-linear representation of magnetometer fluctuations, every three-hour K-value gets converted back into a linear scale, known as the ap index. ap is an average value of the irregular disturbance levels in the horizontal field components and has a three-hour resolution. The average from eight daily ap values gives the Ap index of a certain day. Particle precipitation is often parameterized by Ap in solar forcing models [*van de Kamp et al.*, 2016].

Dst index

The disturbance storm (Dst) index provides a quantitative measure of geomagnetic disturbance that can be correlated with other solar and geophysical parameters [*Kyoto*, 2020b]. The index is based on the average value of the horizontal component of the Earth's magnetic field and is measured in nT. The time resolution of the Dst index is one hour. Four magnetic observatories stationed near the equator are used to derive the Dst index. The observatories are distributed as evenly as possible in longitude and at latitudes where the impact from the auroral and equatorial electrojets are minimal. The Dst index in the Earth's horizontal component is a good indicator of magnetic storms and their severity and can also measure smaller disturbances in the magnetic field.

The use of the Dst index as an indicator of geomagnetic activity is possible because the strength of the surface magnetic field at low latitudes is inversely proportional to the energy content of the ring current which increases during geomagnetic storms [*Hamilton et al.*, 1988]. The Dst index does not take into account the quite-time disturbances from the ring current, as to give a better measure of the geomagnetic disturbance. Other currents also contribute to the Dst, e.g., the magnetopause current, which causes a positive disturbance.

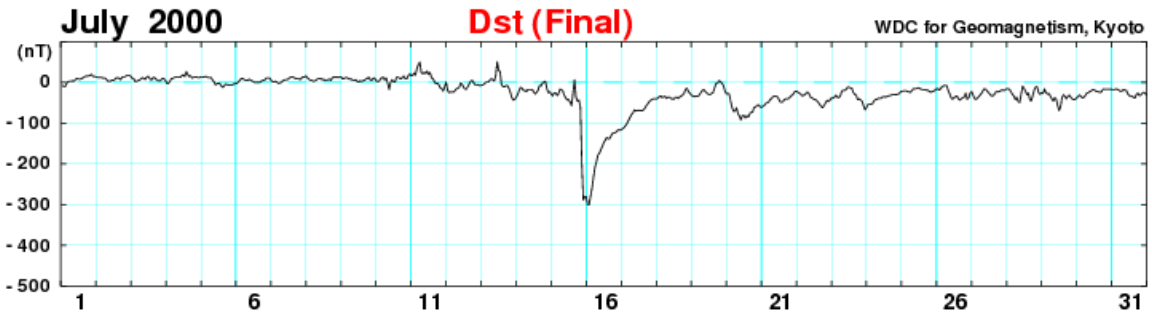

Figure 2.13: The Dst index during a classic storm in July 2000 [*Kyoto*, 2020c].

In the event of a classic geomagnetic storm, the Dst index will suddenly increase, indicating the storm sudden commencement (SSC). This is most likely due to the magnetopause being compressed. Being that the magnetic field induced by the magnetopause current is in the same direction as the terrestrial field, measurements will show an increase. Shortly after the SSC, the ring current will intensify leading to a sharp decrease in Dst. As the ring current starts to recover the Dst index will slowly return to its quite-time level. Figure 2.13 shows the Dst index during a classic geomagnetic storm. The classification of the intensities of geomagnetic storms are based on the maximum amplitude

of the main phase of the Dst index; weak $Dst \leq -30nT$, moderate $Dst \leq -50nT$, strong $Dst \leq -100nT$, severe $Dst \leq -200nT$, and great $Dst \leq -350nT$ [*Loewe and Prölss*, 1997].

2.4.2 CME- and CIR-driven storms

Different phenomena on the surface of the Sun lead to different solar wind properties. The most important large-scale solar wind structures that cause planetary-scale disturbances in the geomagnetic field are CMEs and corotating interaction regions (CIRs) associated with HSSs. These structures are shown schematically in Figure 2.14. When escaping the Sun, CMEs often have greater speed than the ambient solar wind ahead. If the speed difference of the CME and the ambient solar wind is larger than the local magnetosonic speed, a supersonic fast forward shock will propagate into the upstream solar wind ahead of the CME [*Kilpua et al.*, 2017a]. Downstream of the shock, a sheath region exists which is defined as a region between the shock and the corresponding CME where the plasma is turbulent. CIRs are compression regions that occur when HSSs catch up to the slower solar wind stream ahead. A CIR will seem to lead the coronal hole high-speed stream from the perspective of a fixed observer. The largest geomagnetic storms are usually associated with CMEs, while storms associated with HSSs and CIRs are less intense but can often deposit more energy into the Earth's magnetosphere over a longer time [*Borovsky and Denton*, 2006; *Kataoka and Miyoshi*, 2006]. Both CME- and CIR-driven storms can lead to magnetospheric processes that can accelerate low energy plasmas to higher energies.

Typical solar wind properties are shown schematically in Figure 2.14 for both CMEs and CIRs. In-situ measurements of CIRs are characterized by a gradual increase in the magnetic field strength and density. The stream interface is characterized by a sudden increase in temperature and velocity and a sudden decrease in density, as well as a decrease in magnetic field strength [*Kataoka and Miyoshi*, 2006]. Following the stream interface is usually a relatively long-lasting HSS where the solar wind speed gradually decreases. The oscillation of the magnetic field vector between negative and positive values is typical for the arrival of a CIR storm. Moderate ring current enhancements with a long-lasting recovery phase are also characteristic for CIR storms, as illustrated by the Dst index. The small energy injections, caused by the oscillating magnetic field, explain why CIR storms often accelerate electrons in the radiation belts to relativistic energies by causing asymmetric plasma distributions.

The shocks ahead of CMEs can be identified by a sudden increase in the IMF strength, solar wind speed, density, and temperature [*Kataoka and Miyoshi*, 2006]. The sheath region downstream of the shock is compressed, hot, and contains many discontinuities. Following the sheath region is the CME or magnetic cloud. This region contains relatively cold plasma that usually has a smoothly rotating IMF. Downstream from the CME the magnetic field strength, speed, and density drop. The temperature drops to a level below the initial ambient solar wind temperature before it gradually rises back up to normal levels. The smoothness of the magnetic field vector, which usually is negative over longer periods compared to CIRs, allows energy transfer between the solar wind and magnetosphere to happen more efficiently. For this reason, the largest geomagnetic storms are caused by CMEs, which usually can be seen by a larger decrease in the Dst index. Because storms driven by CMEs generally last only a couple of hours while CIR-driven storms can last several days, the total energy input might be comparable. The electron flux in the radiation belts during the recovery phase of a CME-driven storm has been found to take longer to recover to pre-storm values compared to CIR-driven storms and therefore, does not increase above pre-storm values to the same degree [*Kataoka and Miyoshi*, 2006].

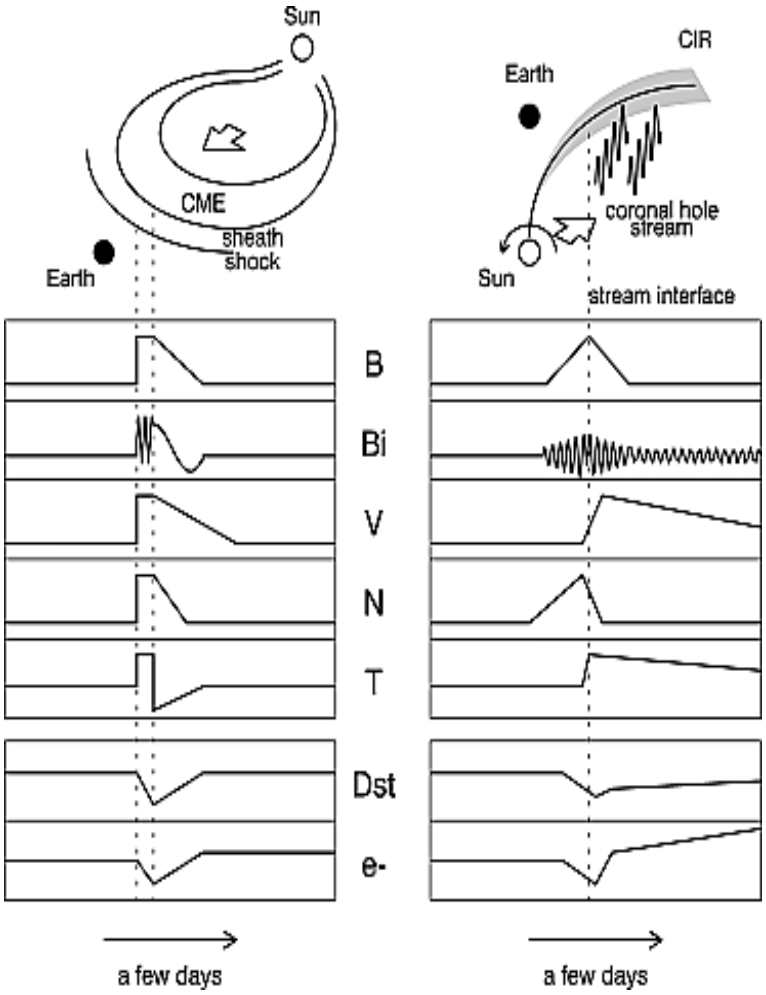

Figure 2.14: Schematic illustration of typical solar wind structures of CMEs and CIRs. From the top, the magnetic field strength B, one of the Cartesian components B_i, solar wind speed V, solar wind density N, solar wind temperature T, expected response of the Dst index, and $> 2.0MeV$ electron flux at geosynchronos orbit $e-$. Source: [*Kataoka and Miyoshi*, 2006]

2.5 Recent Research

Precipitation of energetic particles will increase the production of NOx and HOx gasses in the upper atmosphere, which in turn can catalytically destroy ozone. Ozone is a radiatively active gas which implies that changes could impact temperature. The thermal balance will then potentially affect atmospheric circulation, and it is hypothesized that this chain of reaction, initially triggered by energetic particle precipitation, can propagate all the way to ground level. However, to understand the impact, an estimate of the total energetic particle precipitation impact is required. While solar proton events and the low energy auroral electrons ($< 30keV$) have been widely studied and are well quantified, the amount of energetic electron precipitation ($> 30keV$) remains an outstanding question. How much energy they deposit, their variability, and the community's capability of parameterizing them is currently an active research field.

Magnetic storms and substorms associated with CMEs and HSSs/CIRs are drivers of severe space weather. An important aspect of these space disturbances is the acceleration of charged particles to high energies in the inner magnetosphere which often occurs during and after geomagnetic disturbances. Solar wind speed has been found to be of great importance when it comes to predicting flux variations [*Asikainen and Ruopsa*, 2016]. On average, CIR-associated storms, with their high speeds, fluctuating electric field, and long recovery phases, have appeared to be more effective in EEP flux enhancement than CME-driven storms [*Kilpua et al.*, 2017a; *Kataoka and Miyoshi*, 2006]. However, *Asikainen and Ruopsa* [2016] found that CMEs tend to have larger average fluxes in the radiation belts than HSSs, especially at energies $> 100keV$. This observation is consistent with *Yuan and Zong* [2012], who found that CME-storms produce more relativistic electrons than CIR-driven storms in the entire outer radiation belt, although the relativistic electron fluxes during CIRrelated storms are much higher than those during CMErelated storms at geosynchronous orbit. The effects of combined or superposed solar wind structures have not been thoroughly investigated. However, *Zhang et al.* [2008] found that CIRs following a CME cause relatively more relativistic electron precipitation than low energy fluxes compared to isolated CIRs. *Asikainen and Ruopsa* [2016] point out that solar wind speed during CMEs is the most important factor contributing to the average efficiency of CMEs to produce EEP. These findings indicate that CMEs combined with HSSs could be very efficient in enhancing EEP flux. CME- and CIR-driven storms are often associated with interplanetary shocks and stream interfaces, respectively, which have been found to be useful precursors for predicting flux enhancements [*Kilpua et al.*, 2017a]. Different responses in EEP are associated with different solar wind driver, but there is, however, a need for a better understanding of how and to what degree they are coupled to each other.

Due to the lack of long-term EEP forcing data that can be used in chemistry-climate models, variations in geomagnetic indices have been used to give estimates of EEP. One of the most recent models was developed by *van de Kamp et al.* [2016] and is used in the Coupled Model Intercomparison Project (CMIP) 6 (v3.2). The model is parameterized by the Ap index based on the 0° detector. However, *Tyssøy et al.* [2019] finds that the model falls short in reproducing flux levels and variability associated with strong geomagnetic storms as well as the duration of CIR-driven storms causing a systematic bias within a solar cycle. Another problem worth mentioning is that these models often do not take into consideration the conditions before the time of the input data. Hence, there is a need to find out more about how geomagnetic indices are correlated to EEP and how they depend on different solar wind drivers in order to get a better understanding of how to predict EEP.

Ødegaard et al. [2017] suggests that the epsilon parameter, a measure of the energy transferred from the solar wind to the magnetosphere, might be a good predictor for EEP ($> 30keV$). The energy transfer and how it is distributed throughout the magnetosphere-ionosphere system has been the topic of several studies focusing on auroral energies. Different geomagnetic indices are often used to estimate different energy sinks [*Akasofu*, 1981; *Østgaard et al.*, 2002a; *Tenfjord and Østgaard*, 2013]. So far only an estimate of the energy lost through low energy particle precipitation, U_A, has been made. Traditionally, the low energy electron precipitation has been considered to be most important

for the atmosphere. Recent research, however, points out the importance of electrons that have been accelerated to higher energies in the radiation belts. There is therefore a need for an estimation of the energy lost through high energy electron precipitation.

Different solar wind structures, geomagnetic indices, and the energy budget in the magnetosphere may help to give a better prediction of EEP. One of the main challenges is to unify different aspects of EEP into an overall picture. There are also other phenomena to take into account in order to get a full picture, e.g., wave-particle interactions and substorms, but that is out of the scope of this thesis.

3 Data and Methods

This data and methodology chapter introduces how different data sets and instruments are used in this thesis. The chapter is divided into three sections: 3.1 Solar wind observations, 3.2 Geomagnetic activity indices, and 3.4 Energetic electron precipitation observations.

3.1 Solar wind observations

Most of the solar wind data in this study are retrieved from the OMNIWeb database. OMNIWeb Data Documentation has a low resolution (LRO) data set which contains the hourly-average compilation of near-Earth solar wind magnetic field and plasma parameter data. The data is retrieved from several spacecraft in both geocentric orbits and L1 (Lagrange point) orbits. In this study, the solar wind parameters for the year 2010 were all downloaded from OMNI 2. The plasma parameters used were the IMF Bz (in GSM-coordinates), plasma flow speed, v, and plasma flow pressure, P, all with one-hour resolution.

3.1.1 Solar wind classification

Strucem.txt is a file containing the hourly solar wind structure from 1963 to 2011. It was created by Ian Richardson of the University of Maryland and NASA Goddard Space Flight Center to match the format of solar wind structure in the CEDAR Database. The near-Earth solar wind is classified into three basic flow types that are based on solar wind plasma and magnetic field parameters in the OMNI Database [*Richardson and Cane*, 2012]. Also, data such as geomagnetic indices, energetic particle, and cosmic ray observations were used to help classify the different solar wind flow types.

The three different solar wind flow types or structures, as classified in *Richardson and Cane* [2012] are: (1) High-speed streams associated with coronal holes at the Sun, (2) Slow, interstream solar wind, and (3) Transient flows originating with coronal mass ejections at the Sun, including interplanetary coronal mass ejections and associated upstream shocks and post-shock regions. In the Strucem file unclear data or "?" equals 0, CMEs equal 1, CIRs or high-speed solar wind streams equal 2, and slow speed wind equals 3.

The HSSs are classified as periods when the solar wind speed exceeds $\sim 450 km/s$ in approximately one day and then decreases slowly during the event [*Holappa et al.*, 2014]. The structures defined as CMEs include not only the cores of ICMEs but also the upstream shocks and sheath regions associated with them [*Holappa et al.*, 2014].

3.1.2 Epsilon

In this study, we gratefully acknowledge the SuperMAG collaborators (http://supermag.jhuapl.edu/info/?page=acknowledgement) that have provided the epsilon parameter for the year 2010 [*Gjerloev*, 2012]. The data was retrieved with one-minute resolution. By finding the average value of the epsilon parameter for every 60 minutes, a one-hour resolution epsilon parameter was calculated and used in this study.

3.1.3 Shocks

This study uses data from the Heliospheric Shock Database, generated and maintained at the University of Helsinki. An interplanetary shocks list was retrieved from IPShocks.if that included both fast-forward and fast-reverse shocks for the year 2010 with one-second resolution. The shocks are used to give context to the different phenomenon happening throughout the year.

3.2 Geomagnetic activity indices

The LRO data from OMNIWeb also provides a wide range of geomagnetic indices. The geomagnetic indices for the year 2010 were all downloaded from OMNI 2. In this study, the geomagnetic indices used were the Dst and AE indices, with an hourly resolution, and the Kp*10 and ap indices, with a three-hour resolution. The standard Kp values look like 0, 0+, 1-, 1, 1+, 2-, ... but are stored as Kp = 0, 3, 7, 10, 13, 17, ... in the OMNI data set. They have been mapped as follows; 0+ to 3, 1- to 7, 1 to 10, 1+ to 13, 2- to 17, etc. ap is deduced from Kp. Hence, a certain Kp value will give a specific ap value. While Kp is on a quasi-logarithmic scale, ap is a linear transformation of Kp. All parameters and indices where accumulated over time to get the daily average as a running mean with a 24-hour resolution.

3.3 Energy dissipation

To explain where the energy input to the magnetosphere from the solar wind is being lost, calculations of the three previously mentioned energy sinks (U_A, U_J, and U_R) was done. Other energy sinks such as ion outflow, and auroral emissions, and magnetospheric energy dissipation processes such as plasmoid ejection and plasma sheet heating are neglected because of negligible size or that they are not part of the closed magnetospheric system of interest [*Tenfjord and Østgaard*, 2013]. This study uses the relation between the AE index and the deposited energy by particle precipitation found by *Østgaard et al.* [2002b]:

$$U_A = 4.6AE^{\frac{1}{2}} - 23. \tag{9}$$

As high energy loss to the atmosphere is not part of the typical assessment of the energy budget ([*Akasofu*, 1981; *Østgaard et al.*, 2002b]), we assume that it is scaled to U_A, which represents energy loss through auroral particle precipitation (low energy particles). This implies that we indirectly assume that AE is scaled to EEP, which is only partly true.

To estimate the Joule heating rate from the AE index this study uses the conclusion found and reasoned for in *Østgaard et al.* [2002a]. In their paper results from both summer and winter were used to get the Joule heating in both hemispheres:

$$U_J = 0.54AE + 1.8. \tag{10}$$

To estimate the ring current energy injection rate equation 5, with the help of the pressure correction term ΔH (equation 7) and the pressure corrected Dst* (equation 6) was used. The ring current particle lifetime (τ) was adopted from *Lu et al.* [1998]: $\tau = 4, 8$ or 20 hours depending on if $Dst* < -50, < -30$ or > -30, respectively. All geomagnetic indices used were retrieved from OMNIWeb with a one-hour resolution. All energy rates were multiplied with 3600 seconds. Equation 8 was used to find the total energy dissipation rate.

3.4 Energetic electron precipitation observations

The National Oceanic and Atmospheric Administration (NOAA) has Polar Orbiting Environmental Satellites (POES) that carry instruments that measure the influx of energetic ions and electrons precipitating into the Earth's atmosphere and the particle radiation element at the satellite's altitude. These phenomena vary according to solar and geomagnetic activity. The Medium Energy Proton and Electron Detector (MEPED) on POES monitor the intensities of protons and electrons from 30 keV to more than 200 MeV [*Evans and Greer*, 2004]. Particles with these energies include the radiation belt populations, which are of interest in this study. MEPED is also mounted on the Meteorological Operational Satellite Program of Europe (MetOp).

3.4.1 NOAA/POES satellites

The first launch of a satellite containing the MEPED instrument was in 1978. Since then the instrument has been launched on 14 different satellites, where 12 were part of the NOAA/POES program and two were part of MetOp. Figure 3.1 shows the operational lifetime of the MEPED instruments onboard NOAA/POES and MetOp. In the period of interest, the year 2010, six satellites were operational: NOAA 15 - 19 and METOP-02, all carrying the newest instrument package, SEM-2. The NOAA/POES and Metop satellites are Sun-synchronous low-altitude polar-orbiting spacecrafts. They are orbiting at $\sim 850km$ with a period of $\sim 100min$, resulting in 14 orbits per day [*Evans and Greer*, 2004]. The satellite coverage and the number of data points that were collected by the NOAA/POES satellites for each latitude and MLT during the year 2010 are shown, respectively, to the left and right in Figure 3.2.

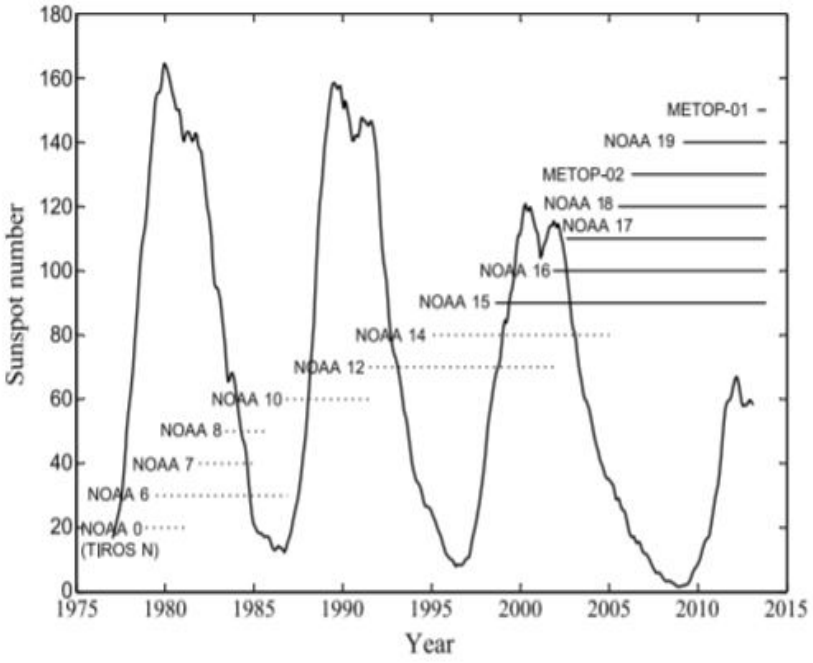

Figure 3.1: Operational periods of the NOAA/POES and MetOp satellites with MEPED instruments. Satellites with the SEM-1 and SEM-2 instrument package are displayed using dotted and solid lines, respectively. From [*Sandanger et al.*, 2015].

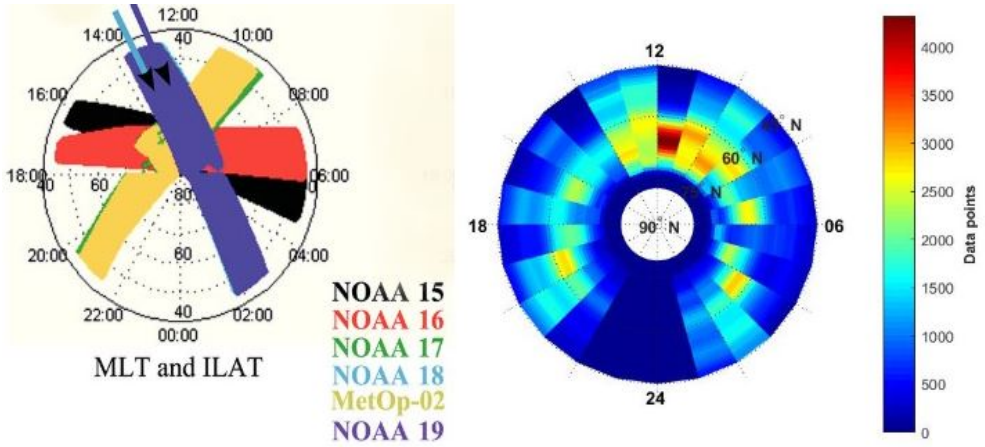

Figure 3.2: To the left: footprints of the NOAA/POES and MetOp spacecraft given as invariant latitude and MLT in the Northern Hemisphere in 2009 when NOAA 19 newly launched and calibrates NOAA 18. From [*Sandanger et al.*, 2015]. To the right: the number of data points collected by all available NOAA/POES satellites in the ear 2010 for each corrected geomagnetic latitude and MLT.

3.4.2 MEPED intrument

MEPED includes eight separate particle detector systems. Two are identical proton solid-state detector telescopes, monitoring the intensity of protons in six energy bands over the range $30keV$ to $6.900keV$, and two are identical electron solid-state detector telescopes that monitor the intensity of electrons in three energy bands in the range $30keV$ to $2.500keV$ [*Evans and Greer*, 2004]. Table 1 shows an overview of the nominal energy ranges of the different electron and proton channels used in this study. The highest MEPED proton channel (P6) gets contaminated by relativistic electrons. It can, therefore, be used to extract relativistic electron fluxes in periods of little or no high energy proton fluxes. The four detectors are arranged in a 0° and 90° telescope, each consisting of one proton and one electron detector. The solid-state detector telescopes are included in SEM-2 [*Evans and Greer*, 2004].

Table 1: Nominal detector responses in the three electron channels (E1, E2, E3) and the highest proton channel (P6) of the SEM-2 MEPED electron and proton detectors [*Evans and Greer*, 2004]. The optimized integral energy limit for the different channels are noted in brackets [*Ødegaard et al.*, 2017]. Column three shows the energy ranges of contaminating protons for the electron detectors [*Yando et al.*, 2011]. The last column shows the geometric factor [*Ødegaard et al.*, 2017].

Energy Channel	**Nominal Range [keV]**	**Contaminating Energy Range [keV]**	**Geometric Factor** $[cm^{-2}sr]$
E1	$> 30 (> 43)$	210-2600	0.0101
E2	$> 100 (> 114)$	280-2600	0.0112
E3	$> 300 (> 292)$	440-2600	0.00808
P6	$> 6900 (> 756)$	-	0.00739

The 0° telescopes are oriented so that they point radially outward along the Earth-satellite connecting axis. The 90° telescopes are oriented so that they are perpendicular to the 0° telescopes and anti-parallel to the satellite's velocity vector. Both telescopes are rotated away from the described axis by 9° to ensure a clear field of view [*Evans and Greer*, 2004]. Figure 3.3 shows the opening angle and direction of the 0° and 90° detectors, together with the atmospheric loss cone at a specific latitude with respect to the background geomagnetic field. As precipitating charged particles gyrate about the magnetic field lines, the 0° telescopes will mainly measure atmospheric loss cone parti-

cles when traveling across high geomagnetic latitude, while the 90° telescopes will mainly measure high-latitude trapped radiation belt particles and equatorial loss cone particles.

The two telescopes do not give a realistic estimate of the loss cone fluxes. The orientation of the 90° telescope will lead to an overestimate of the bounce loss cone (BLC) electron flux, while the orientation of the 0° telescope will lead to an underestimation. This is because the energetic electron fluxes are often strongly anisotropic with decreasing fluxes towards the center of the loss cone [*Tyssøy et al.*, 2016]. In rare cases of strong pitch angle diffusion and an isotropic distribution, the two telescopes can give a relatively good estimate of the precipitating flux, but a more realistic estimate is needed. *Tyssøy et al.* [2016] constructed a complete BLC flux for each of the four-electron energy channels by combining measurements from both telescopes with electron pitch angle distributions from theory of wave-particle interactions in the magnetosphere. A more detailed description on the construction of the BLC fluxes can be found in *Tyssøy et al.* [2016]. It is worth noting that *Tyssøy et al.* [2016] cautions against using the estimated BLC fluxes during quiet times because when the 0° detector measures fluxes close to the noise level of the instrument, the uncertainty in the estimated BLC fluxes will increase. No filter on low fluxes was applied in this study.

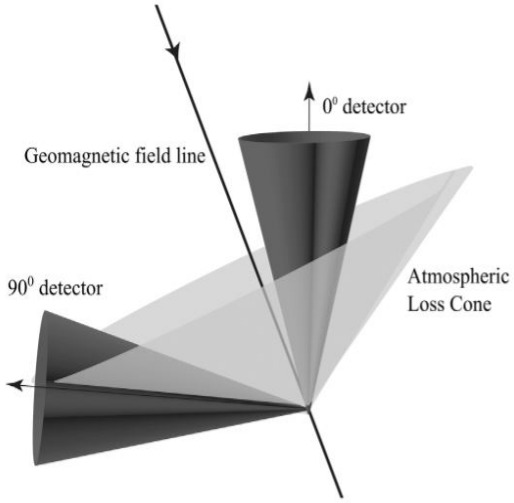

Figure 3.3: The opening angle and direction of the 0° and 90° detectors, together with the atmospheric loss cone at a specific latitude. From: [*Søraas et al.*, 2018].

The left side of Figure 3.4 shows a cross-section schematic of the proton solid-state detector telescope. To prevent electrons with energies less than $\sim 1.000keV$ from entering the aperture and reaching the solid-state detectors a magnetic field of $\sim 0.2T$ is applied across the entrance aperture and collimator. To prevent electrons of energies $< 6.000keV$ or protons of energies $< 90MeV$ from reaching the detectors, the detectors, with an exception of the entrance aperture, are surrounded by a combination of aluminum and tungsten shielding. The remaining flux of protons and ions fall upon the detector stack.

The solid-state detectors are both $200microns$ thick totally depleted silicon surface barrier detectors. The front surface of each detector is with an aluminum film used to reduce light sensitivity and provide electrical contact. Protons stopped by the first detector are sorted into five energy ranges according to their energy loss in the detector. The energy loss is determined by electronic pulse height analysis. The sixth proton energy band is sorted by protons that pass through the front detector and are stopped by the back detector which produces a coincident response in both the front and back detectors. A full data set from both proton telescopes require $2.0sec$ to acquire.

The design of the electron telescope instrument is similar to that of the proton telescope (see right

hand side of Figure 3.4). The basic geometry and collimation angles are the same, but there is no magnetic field applied across the collimator. Incident protons are absorbed by a nickel foil that also reduces light sensitivity. The electron telescope has only one solid-state electron detector which is $700microns$ thick and absorbs electrons of energies up to $\sim 2500keV$ in the three previously mentioned ranges.

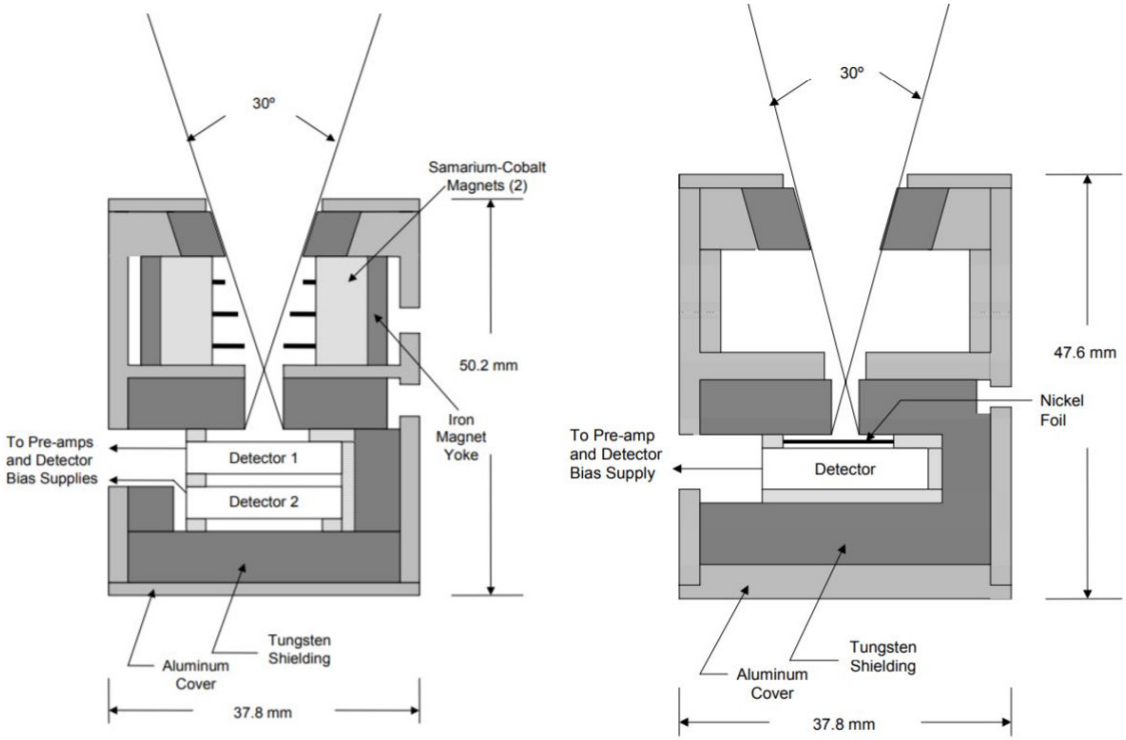

Figure 3.4: A cross-section schematic of the proton solid-state detector telescope (left) and electron solid-state detector telescope (right). From [*Evans and Greer*, 2004].

4 Results

To understand the link between solar wind and electron precipitation, a comparison of solar wind structures to different solar wind measurements (Section 4.1), geomagnetic indices (Section 4.2), and energetic electron precipitation (Section 4.3) has been done. The study is limited to the year 2010. All observations presented are sorted into periods dominated by CMEs or HSSs according to the definitions from *Richardson and Cane* [2012].

The different solar wind structures for the year 2010 are presented in Figure 4.1. Periods for when CMEs are present are shown as red shaded boxes, while periods when HSS and their associated CIRs are present are shown as blue shaded boxes (from now on CIRs and HSS will be referred to as just CIRs). Times with slow or ambient solar wind and times with unclear data or no data are shown by the areas without any shading.

The percentage in which the different solar wind structures occur in the year 2010 is 5.97% for CMEs, and 35.63% for CIRs. From Figure 4.1 it can be seen that there are 11 CME events and 38 CIR events. In May, there are two cases where CMEs occur right before CIR events, in February there is a case where a CIR occurs before a CME, and in April and August, there are two cases where a CME ends up between two CIR events. The rest of the events occur individually.

In Section 4.4, both isolated events and combinations of events will be investigated in more detail in order to understand how similar solar wind structures can lead to different electron precipitation responses. The energy budget in the magnetosphere will also be considered. A comparison of events of the type: (1) isolated CIRs (Oct vs Nov), (2) CMEs occurring ahead of CIRs (May vs Jun), and (3) CMEs occurring between two CIRs (Apr vs Aug) is performed.

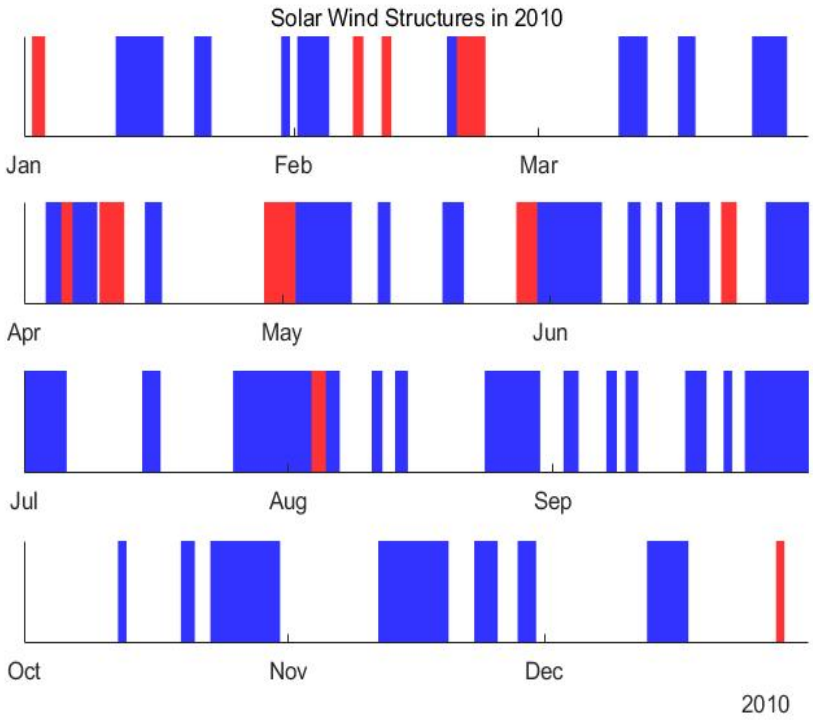

Figure 4.1: Solar wind structures for the year 2010. The red shaded boxes indicate times when CMEs are present, blue indicate times when CIRs are present, and areas without shading indicate slow solar wind or times with unclear data.

4.1 Solar wind measurements

4.1.1 IMF Bz

The IMF Bz is one of the most important parameters to determine the geoeffective structure of the solar wind. Figure 4.2 shows the solar wind component Bz with an hourly resolution. There are some fundamental differences between the different solar wind structures and the behavior of Bz. Although there are large variations in the Bz components, CMEs typically show a steady increase or decrease, as seen in the event at the end of May. The CIR events, however, are usually associated with strong oscillations, as in the following event in June.

Figure 4.3 shows Bz as a running mean with a 24-hour resolution. It reveals if the oscillation occurs around a negative or positive Bz. For example, the CIR event in May does not have a large decrease in the Bz component, but it still oscillates about a negative Bz which implies that it will give rise to significant amounts of energy coupling. The CMEs with a prominent negative Bz occur only in April ($-5.5nT$ and $-2.9nT$), June ($-9.0nT$), and August ($-2.0nT$). The longest CIR events where Bz oscillates around a negative value for a relatively long period are found in April, May, and June.

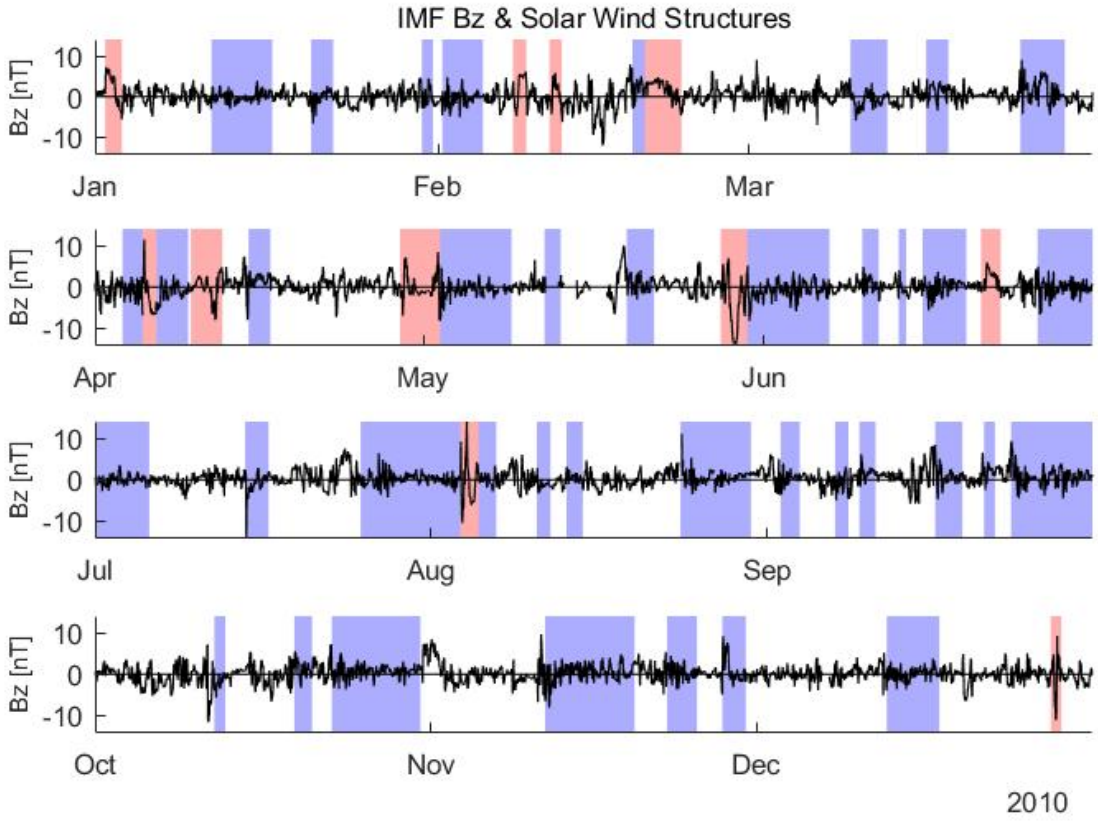

Figure 4.2: The IMF component Bz $[nT]$ with an hourly resolution, together with different solar wind structures (CMEs in red, CIRs in blue).

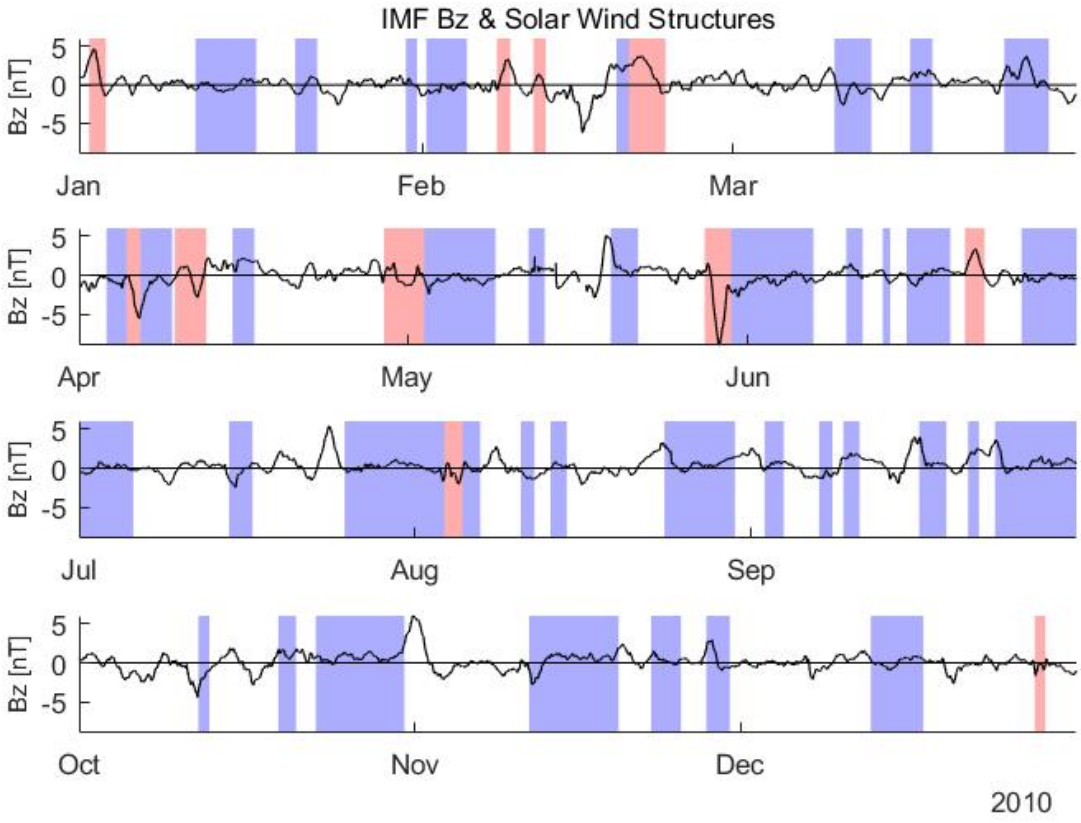

Figure 4.3: The IMF component Bz $[nT]$ with a daily resolution together with different solar wind structures (CMEs in red, CIRs in blue).

4.1.2 Solar wind flow pressure and speed

Figure 4.4 shows the hourly resolution of the solar wind speed (v) and the solar wind flow pressure (P). During all CIRs the solar wind speed is high due to the classifications made in *Richardson and Cane* [2012] which are based on speed. Strongly elevated values of v are found during CIR events in May, June, July, August, September, and October, where the largest speed is measured in May ($718km/s$). The speed peaks at the beginning of most CIR events and then slowly decreases, as seen in May and July. Some CIR events, however, have more than one peak, as seen in June and November. During the CMEs, the solar wind speed is relatively low. There are two exceptions, found in April ($814km/s$) and August ($598km/s$), both where a CME occurs between two CIR events. In these cases, the speed is quite high during the start of the CME and then shows a close to linear decrease throughout the event.

The pressure is a function of speed and density. As both CMEs and CIRs have a leading compressed region of high density, a peak in the pressure can be found at the beginning of most events. For the events in April and August the pressure peaks ($13.4nPa$ and $9.8nPa$, respectively) when the CME occurs and is relatively low during the CIRs before and after. The two events in May and June, where a CME occurs before a CIR, show some differences in the behavior of the pressure. In May the pressure peaks as the CIR occurs ($10.9nPa$), while in June, the pressure is relatively low throughout the entire event but has a peak at the beginning of the CME ($5.9nPa$). In some cases, there is a peak in pressure at the end of an event, as in the second CME in April and the last CIR in October.

There are in total 62 shocks in 2010. The data is received from the Heliospheric Shock Database, generated and maintained at the University of Helsinki. CME related shocks are expected to be fast forward, as they often exceed the speed of the ambient solar wind ahead. The apparent random timing of the CME related shocks might be explained by the shock waves having a larger spatial extent than the interplanetary structures. In theory, near-Earth orbit CIRs are typically bounded by fast forward-fast reverse shock pairs. In 2010 there are 22 fast forward and 16 fast reverse shocks.

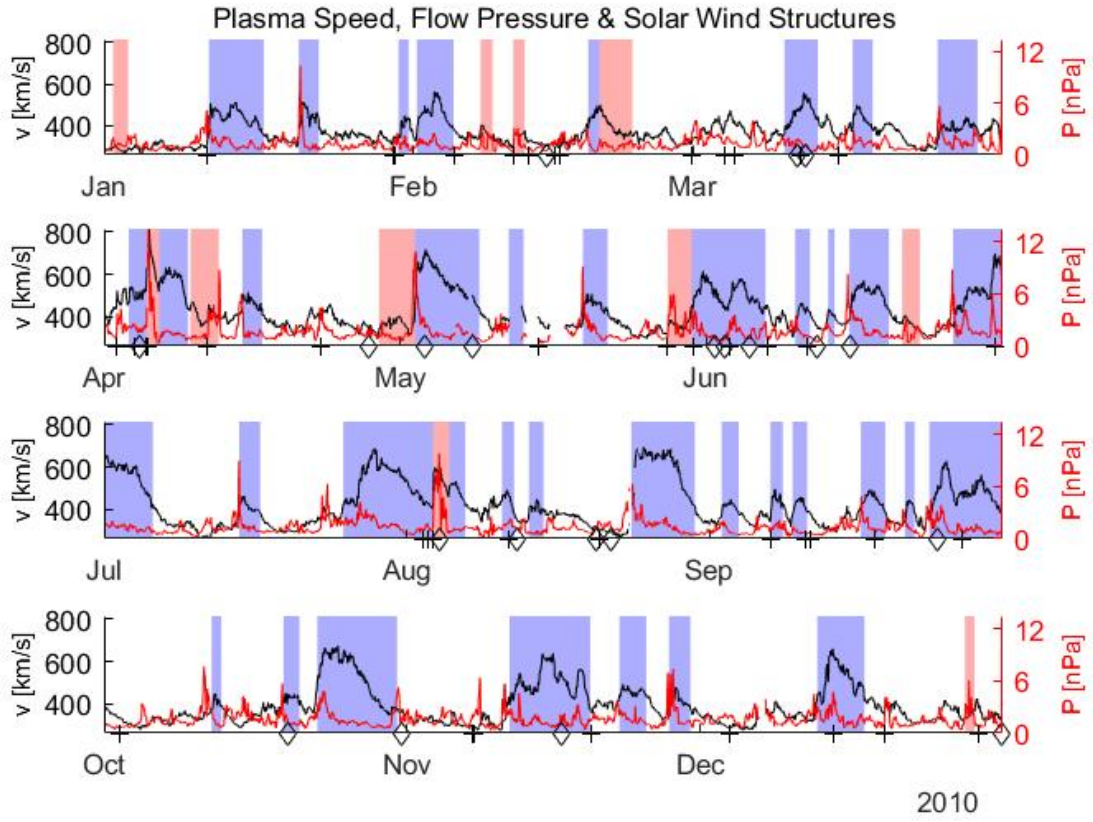

Figure 4.4: Plot of the solar wind speed $v[km/s]$, flow pressure $P[nPa]$, and fast forward (+) and fast reverses ($\Diamond$) shocks.

4.1.3 Epsilon

The epsilon parameter, retrieved from the SuperMAG database [*Gjerloev*, 2012], is an estimate of the energy input from the solar wind to the magnetosphere. The hourly resolution of epsilon is shown in Figure 4.5. Epsilon peaks during the CME events in April, end of May, August, and December. It is largest during the CMEs in April and August, with values reaching $1.8e12W$ and $1.6e12W$, respectively. The hourly energy input during the rest of the CMEs is relatively low, as it is during most of the CIR events. However, the CIR events in May and in the middle of July have strong estimated energy inputs, both reaching $1.8e12W$.

The total energy input throughout an event is presented in Figure 4.5 as a number at the beginning of that particular event. The event that has the largest total energy input is the CME in May/June ($10.40e16J$), followed by the pursuing CIR ($8.08e16J$) and the CME in April ($7.93e16J$). The combined events (CME + HSS) in May and June, have a total energy input of $9.28e16J$ and $18.48e16J$, respectively. And the combined events in April and August (HSS + CME + HSS)

have a total energy input of respectively $13.42e16J$ and $11.79e16J$.

The energy transfer to the magnetosphere is expected to be low during positive Bz and higher the more negative oriented the component is. Figure 4.2 shows only a few cases that include both strong solar wind activity and a significant negative value in the Bz component. At the beginning of the year, from January to April, the negative oscillations in Bz are weak during the solar wind events. This explains the low epsilon values found during this period. The combined events in April and June both have a strong negative value in Bz during the CMEs and an overall negative value of Bz throughout the event. Looking at epsilon, these are the periods with the strongest energy input. During the combined event in May, the energy input stays quite low during the CME, but peaks when the CIR hits. This may be explained by the weak oscillations in Bz during the CME, and the clearer drop in Bz when the CIR occur.

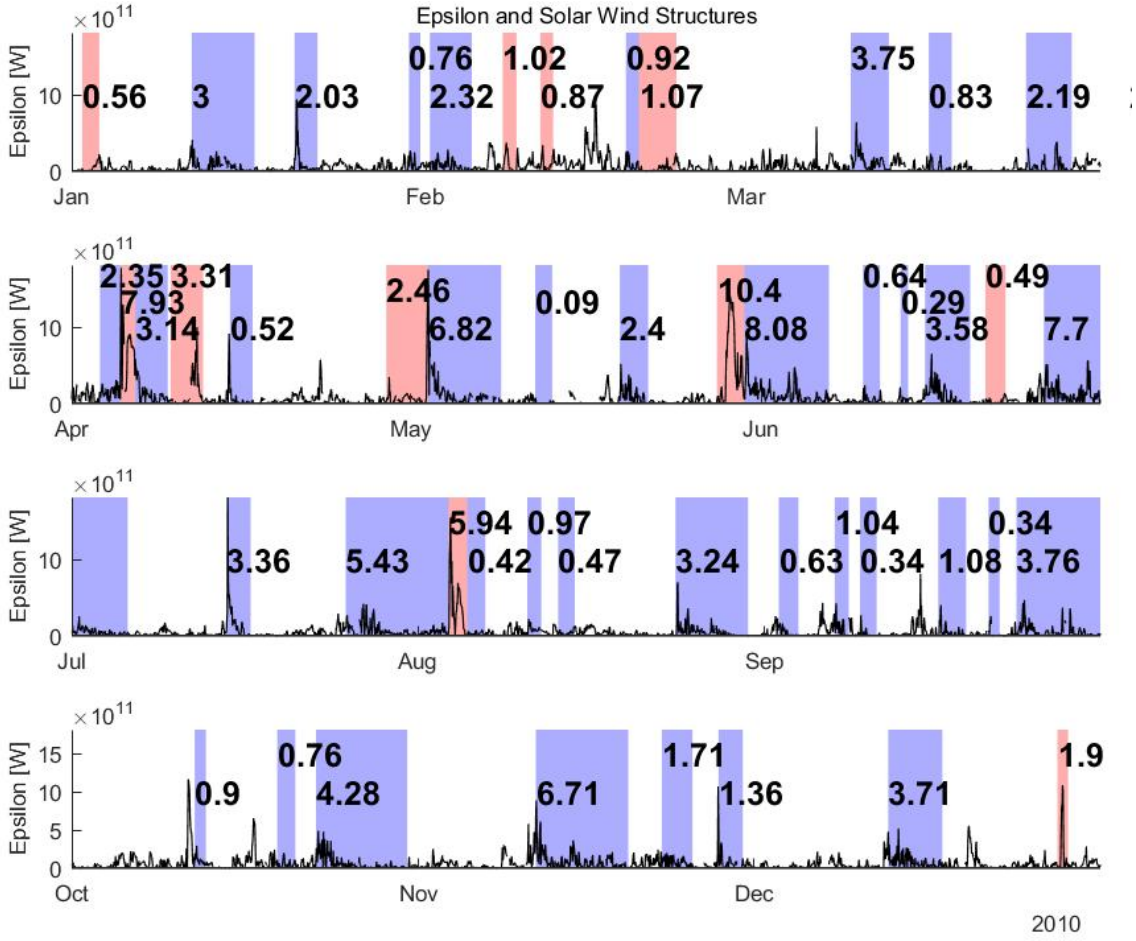

Figure 4.5: Plot of the hourly energy input to the magnetosphere, epsilon [W], and the total energy input throughout an event numbered at the beginning of each particular event. The total energy is given in $[e16J]$ and is rounded up to two decimal places.

4.2 Geomagnetic activity indices

4.2.1 ap and AE

AE represents the overall activity of the auroral electrojets in the northern hemisphere. ap, being derived from the Kp index, is an average value of the irregular disturbance levels in the horizontal field components at mid-latitude magnetometer stations. The AE index has a one-hour resolution, while the ap index has a three hour-resolution. Figure 4.6 shows the two indices as a running mean with a 24-hour resolution. Both the ap and AE follow the evolution of epsilon (shown in Figure 4.5). When the energy input to the magnetosphere is large, so are the values of ap and AE. This is clear during the CMEs in April, June, and August, and during the CIR at the beginning of May.

Both indices are affected by magnetic disturbances caused by magnetic storms. Their behavior is therefore quite similar, but because they are derived from measurements obtained at different latitudes, disturbances may appear shifted or vary in amplitude relative to the index itself. A shift is seen during the CME at the beginning of April, where the peak in ap occurs 19 hours before the peak in AE. During the CME at the end of May, the relative increase in AE is larger compared to the one in ap. The opposite happens during the CME in August, where the relative increase in ap is greater than in AE.

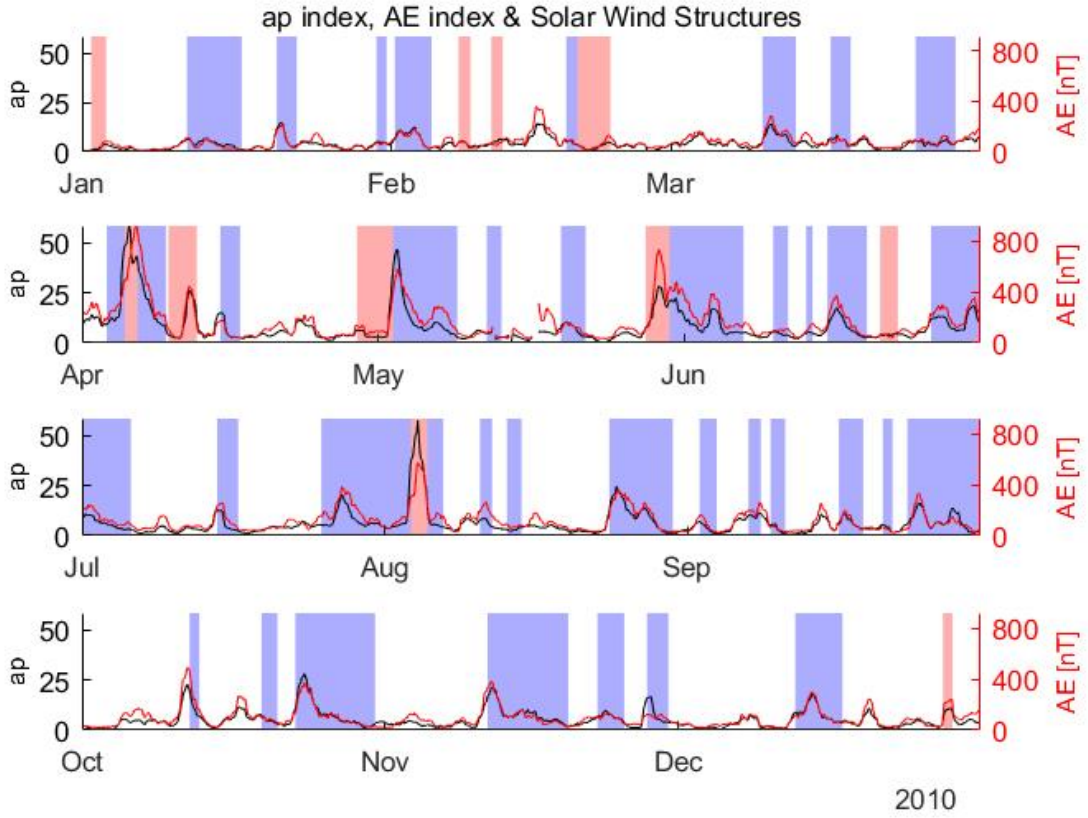

Figure 4.6: Plot av the geomagnetic indices ap and AE [nT].

4.2.2 Kp and Dst

The Dst index is a measure of the overall geomagnetic disturbance and is retrieved from four observatories around the equator. A plot of Dst and Kp*10 as a running mean with a 24-hour resolution is shown in Figure 4.7. Large disturbances of the Dst index are found during the CMEs in April, May, and August, where the largest disturbance happens in April ($-69.3nT$). Two CIR events show substantial disturbances in the Dst, one in May ($-53.9nT$) and one in the middle of October ($-49.4nT$). In some cases, a SSC occurs, as seen during the CME and the first CIR in May.

The largest disturbances in the Kp*10 index occur at the same time as the largest disturbances in the Dst index, exceeding 43 during the CMEs in April and August and during the CIR in May. It also shows a substantial increase at the beginning of many of the CIR events, e.g., at the end of October and middle of November. After the peak in Kp*10, it then proceeds to slowly decrease, maybe with another small peak, as in the CIR event at the end of August.

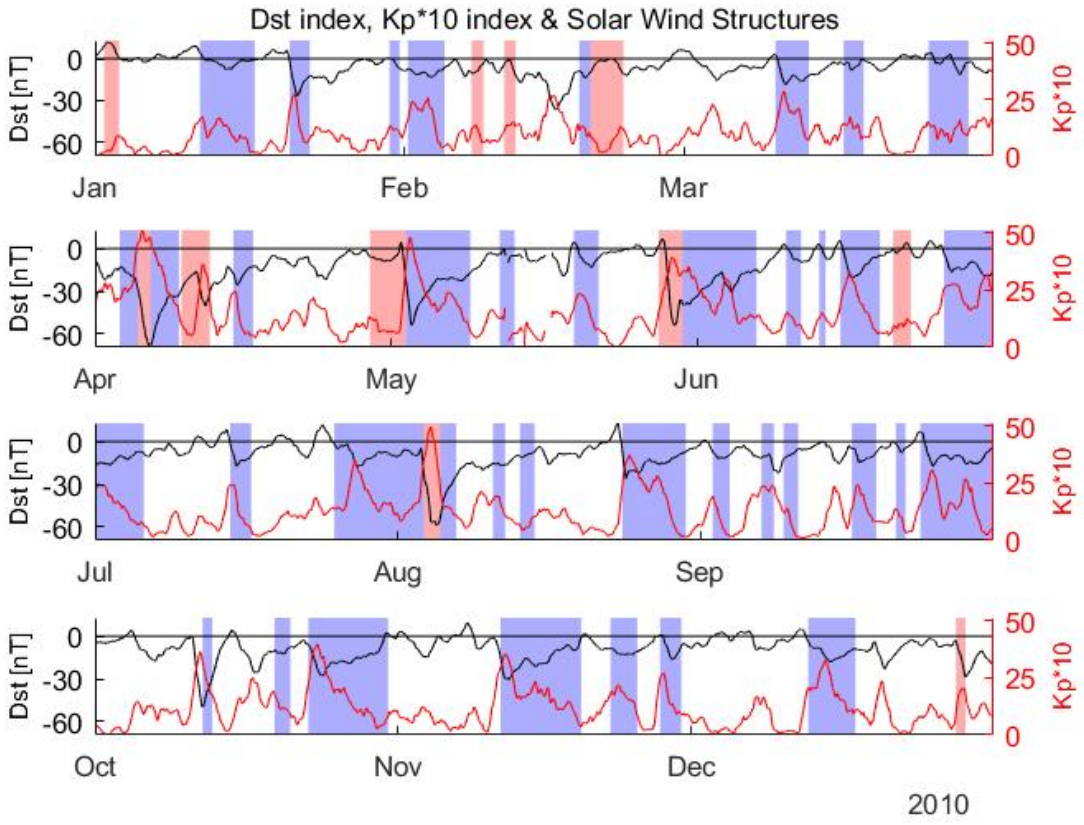

Figure 4.7: Plot of the geomagnetic indices Dst [nT] and Kp*10.

The strength of a geomagnetic storm is often defined based on the hourly value of the Dst index. The events in 2010 that can be categorized as a geomagnetic storm according to *Loewe and Prölss* [1997] ($Dst < -30nT$) are presented in Table 2. There are in all 16 storms, five moderate and the rest week. The strongest storms are all combined events, except for the isolated CME in April. During these moderate storms, the hourly value of the other magnetic indices (ap, Kp*10, and AE) are also at their strongest. Three other CIR events towards the end of the year, including the CME in December, also show a relatively large disturbance in AE. Epsilon is relatively high during the periods of moderate storms. Looking at the number of days a storm lasts, epsilon is quite high for all events lasting up to four days or more.

Table 2: Events and combined events with hourly Dst $< -30nT$: (from the left) the event, the period in which the event occurs, the minimum hourly Dst value, the maximum hourly values of the ap, Kp*10 and AE indices, and the combined energy input to the magnetosphere during the event (Epsilon).

Event	**Period (2010)**	**Max AE [nT]**	**Max ap/Kp*10**	**Min Dst [nT]**	**Epsilon** $[10^{16}J]$
CIR	20.Jan - 22.Jan	674	27/40	-35	2.03
CIR	10.Mar - 13.Mar	557	22/37	-30	3.75
CIR+CME+CIR	03.Apr - 09.Apr	1345	179/77	-81	13.42
CME	09.Apr - 12.Apr	855	67/57	-67	3.31
CIR	15.Apr - 16.Apr	444	22/37	-35	0.52
CME+CIR	28.Apr - 08.May	867	80/60	-71	9.28
CME+CIR	28.May - 06.Jun	1293	56/53	-80	18.48
CIR	15.Jun - 19.Jun	726	22/37	-36	3.58
CIR	26.Jun - 05.Jul	755	23/43	-31	7.70
CIR+CME+CIR	25.Jul - 06.Aug	1088	111/67	-74	11.79
CIR	24.Aug - 30.Aug	824	39/47	-34	3.24
CIR	23.Sep - 30.Sep	683	32/43	-32	3.76
CIR	12.Oct	577	22/37	-48	0.90
CIR	22.Oct - 30.Oct	851	48/50	-41	4.28
CIR	11.Nov - 19.Nov	850	39/47	-45	6.71
CME	28.Dec - 29.Dec	938	27/40	-43	1.90

4.3 Energetic electron precipitation

To examine how different solar wind structures impact energetic electron precipitation, observations of electron fluxes from the multiple POES satellites have been investigated. First, the spatial and temporal evolution of EEP will be discussed, followed by the evolution of energy. Lastly, the relationship between trapped particles and particles lost to the atmosphere will be presented. The focus will be on electrons precipitating in the E1 and E3 energy channels. This is because E3 measures energies an order of a size larger than E1. Hence, it might reflect a different nature than E1 as the magnetospheric acceleration and pitch angle scattering processes are energy-dependent. We choose E3 over P6 due to statistics as the low counts in P6 will be more influences by the noise floor.

4.3.1 Spatial and temporal variations in EEP

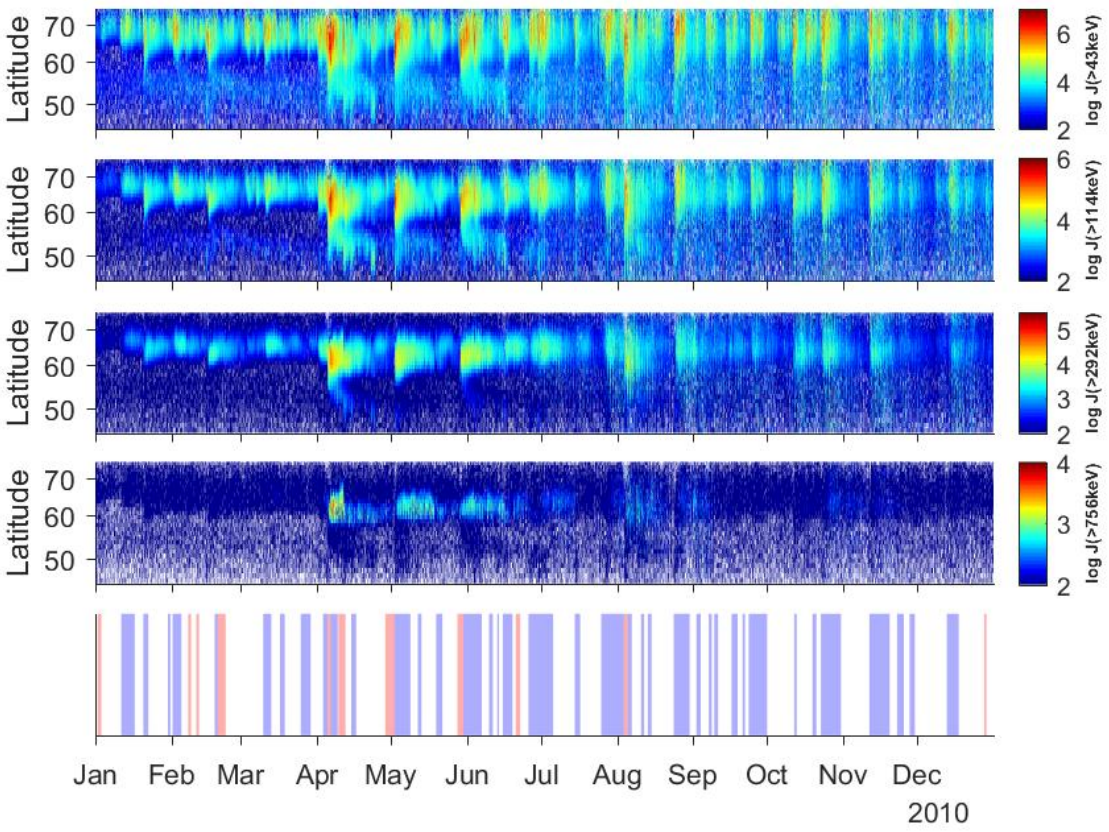

Figure 4.8: A logarithmic color scale plot of the average loss cone fluxes for the year 2010 from 45° to 75° corrected geomagnetic latitude. (top to bottom) E1, E2, E3, and P6 flux channels from the POES satellites. The fifth panel shows the corresponding solar wind structures (CMEs in red, CIRs in blue). The range of the colorbar is different for the four channels. All available NOAA/POES satellites were used.

Figure 4.8 shows radiation belt fluxes for the loss cone in the year 2010 as a function of time and geomagnetic latitude. The four first panels show the different energy channels in ascending order; E1 ($> 43keV$), E2 ($> 114keV$), E3 ($> 292keV$), and P6 ($> 756keV$). The color scale is logarithmic and is different for each energy channel. The fifth panel shows the solar wind structures throughout the year. The largest precipitation for all the energy channels occurs in the outer radiation belt

($\sim 60° - 75°$).

The beginning of the year is characterized by weak activity, both in terms of maximum flux strength and the latitudinal coverage of the precipitation region. The strongest event throughout the year is found in April where high fluxes are evident in all energy channels. During this period, the flux is distributed in a broadband. Here the region between the outer and inner radiation belts has been filled with electrons during the main phase of the storm, which is known as a "slot filling event". As the event evolves, the slot is again carved out leading to a double structure in the recovery phase of the storm. The event in May has the same tendencies as in April with a flux increase in all energy channels and a broad oval, but with the overall intensity being smaller. The same goes for the events in June, July, and August. At the end of the year, the events are short and less intense.

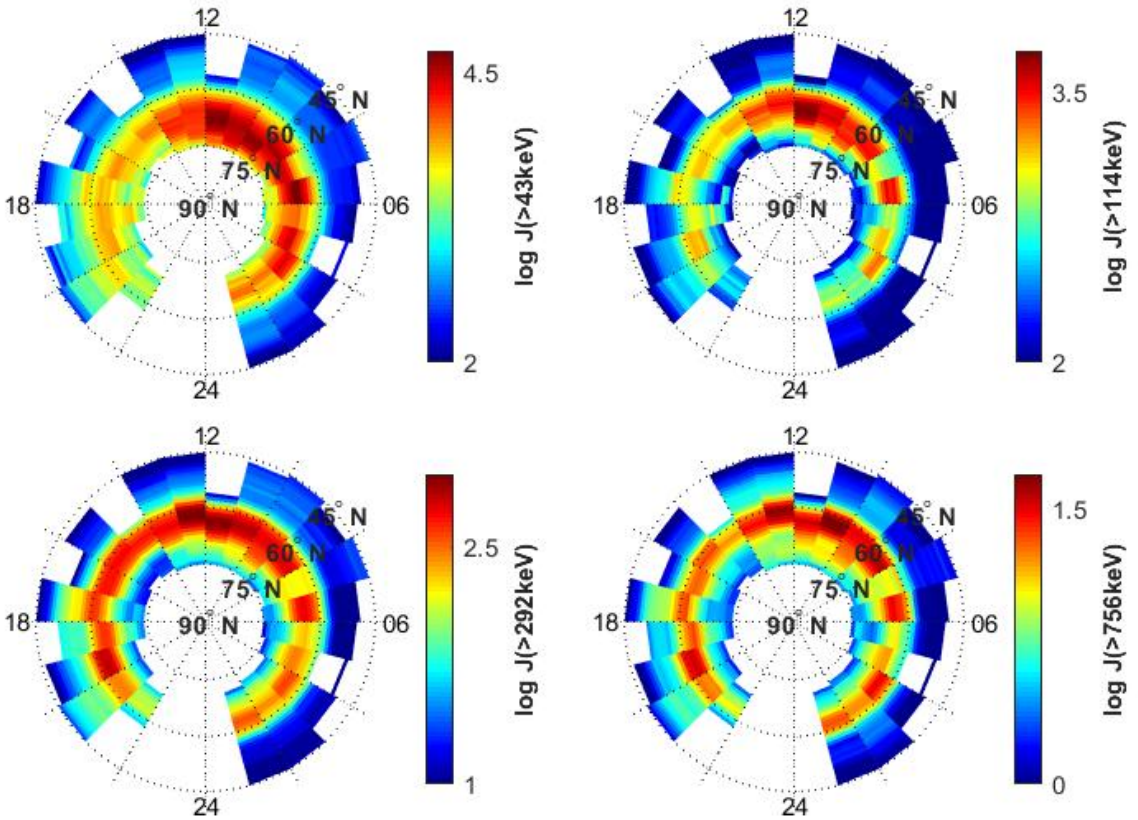

Figure 4.9: A logarithmic color scale plot of the average loss cone fluxes for the year 2010 from 45° to 80° corrected geomagnetic latitude for all MLT. (From the top, left to right) E1, E2, E3, and P6. The range of the colorbar is different for the four channels. All channels have a threshold of 500 data points to be acceptable data. All available NOAA/POES satellites were used.

Consistent with the geomagnetic activity, summarized in Table 2, the complex CIR+CME+CIR event in April is the strongest precipitation event in all energy channels. Despite being built up of the same solar structures and similar energy input, the event in August is significantly weaker. The two CME+CIR storms in May and June seem to be quite similar in intensity and duration, which is to be expected from the findings in Table 2. The two CIR events in October and November, however, do not seem to correspond well with the observations in Table 2. Both events last for nine days and have a significant energy transfer to the magnetosphere. They display similar features in the precipitation, however, based on Figure 4.8, these periods do not seem to be of great relevance when it comes to EEP. This is especially clear when looking at the higher energy channels, or by

comparing these events to the events in April, May, and June.

Figure 4.8 gives a nice overview of the latitudinal flux variations for all energy channels, but information about the variations in MLT is also needed to better understand the spatial variations. The average loss cone fluxes for the different energy channels throughout the year 2010 are shown in Figure 4.9 as a function of corrected geomagnetic latitude and MLT. Areas with less than 500 data points were discarded in the plots. The four different energy channels have different magnetic latitude and MLT characteristics. E1 has a relatively broad flux distribution that is dominant on the morning side. E2 fluxes are also dominant on the morning side but reach moreover towards the evening side. The latitudinal distribution of the E2 flux does not reach the same pole-ward boundary as the lower energy channel. The two higher energy channels have a much more uniform distribution for all shown MLT covering more equator-ward latitudes compared to E1. The MLT variation makes sense in the way that higher energy electrons travel faster, reaching all the way around the Earth, before getting lost to the Earth's atmosphere. The latitudinal coverage implies that the higher energy electrons are found closer to Earth deeper into the magnetosphere.

4.3.2 Energy variations in EEP

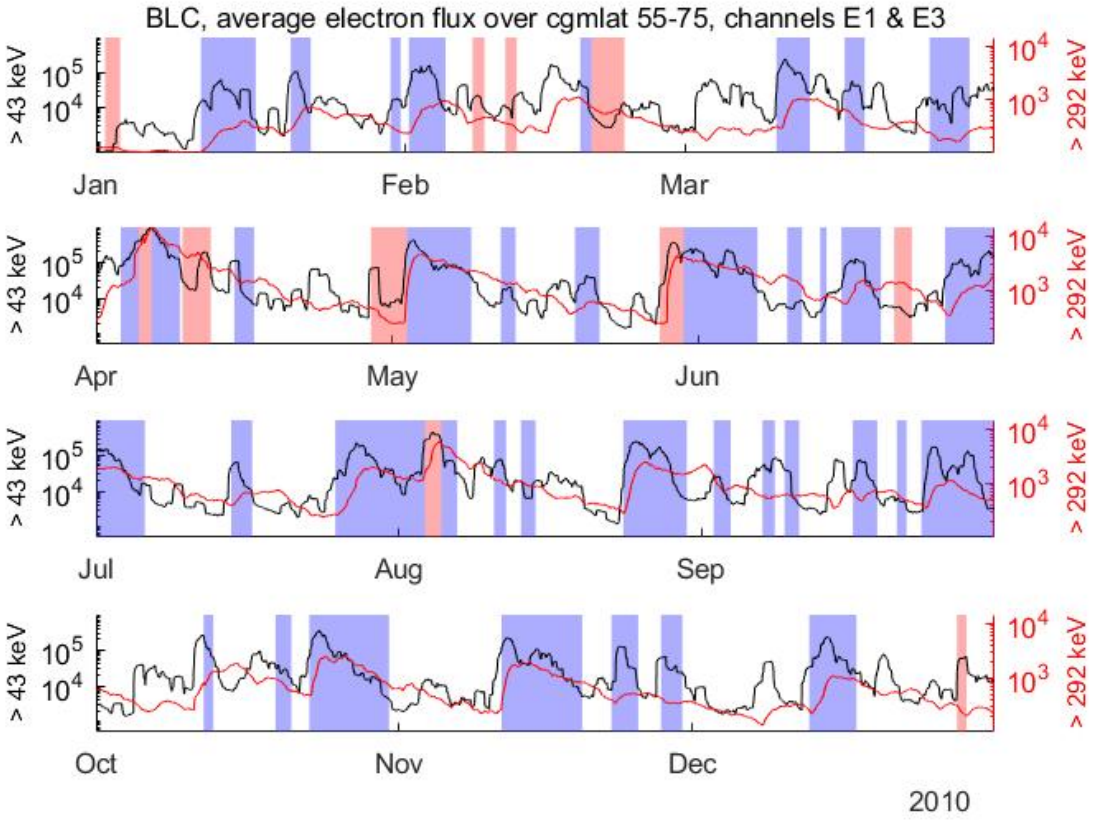

Figure 4.10: Logarithmic line plot of the daily running mean electron flux over Corrected GeoMagnetic (CGM) latitude 55-75 for the E1 (black) and E2 (red) channels during the year 2010. Note that the range differs between the two channels.

To examine the evolution of the lower and higher energies, Figure 4.10 shows a running mean with a 24-hour resolution of the electron fluxes, E1 and E3, in the BLC for the year 2010. Due to most of the precipitation being associated with the outer radiation belt, the following flux plots are given as the

average flux over the latitude band $55° - 75°$. The line plots are on logarithmic scales with different ranges. Throughout the entire year, the electron flux in channel E1 is more variable compared to the flux in E3. The sudden increase in flux found at the beginning of many events is slightly shifted in time for the two energy channels. The E1 flux increases before the flux in E3 does. This is visible, e.g., during the active periods in August, October, and November, where the delay in E3 is 34 hours, 26 hours, and 20 hours, respectively.

The highest flux, in both channels, occurs during the combined storm in April where it peaks at the end of the CME. The combined storm in August, having the same structure, shows two high peaks: one at the beginning of the first CIR and one during the CME. During this storm, the difference in increase between the two channels is larger, with the flux in the lower energy channel increasing relatively more. For the storm in May, where little geomagnetic activity happens during the CME, there is a brief increase in flux for the lower energy channel. The flux in both channels increases substantially when the CIR occurs. For the storm in June, the fluxes increase and peak during the CME and stay high throughout the storm. During the CIR storms, the fluxes increase and peak at the beginning of the storm and then decrease slowly after, for instance, seen during the storms at the end of August, October, and November. The relative E3 flux increase is higher compared to the lower energy channel.

4.3.3 Trapped and lost electrons

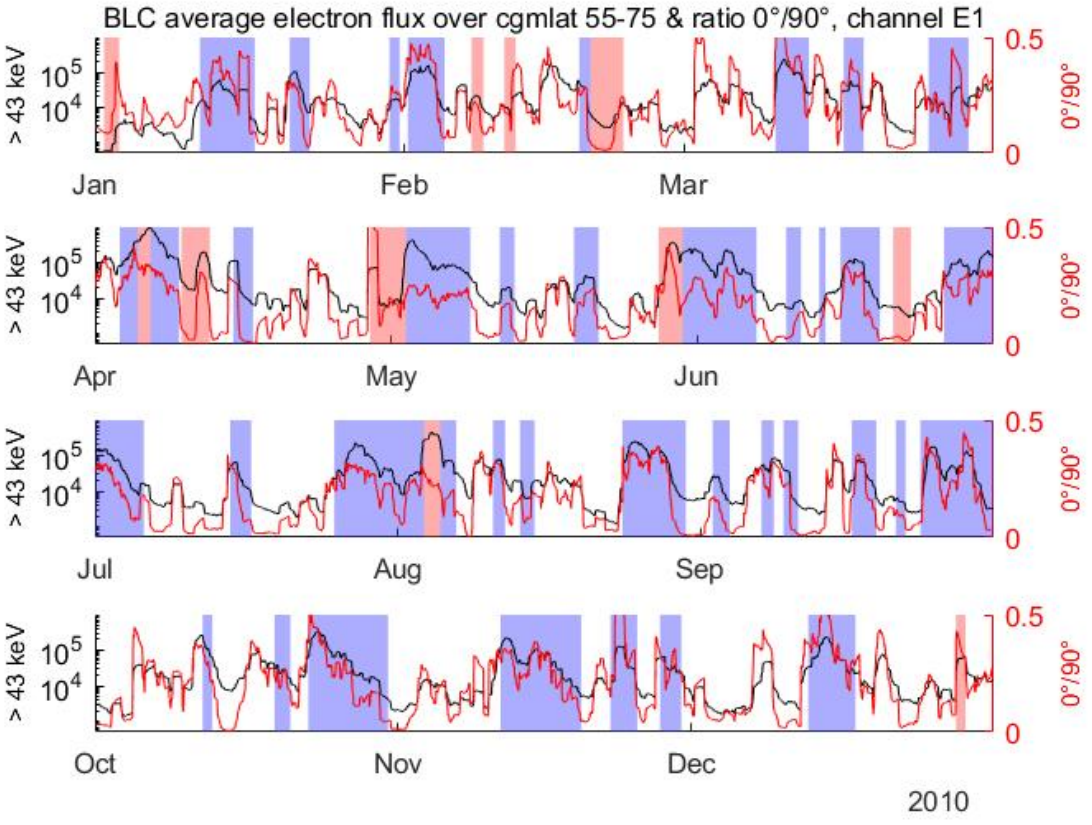

Figure 4.11: Logarithmic line plot of the daily running mean electron flux over CGM latitude 55-75 (black) and the ratio between the 0° and 90° detectors (red) for the E1 channel.

The ratio between the electron flux measured by the 0° detector and the 90° detector can be used

as a proxy for the rate in which trapped particles are being pushed into the loss cone and are precipitating and getting lost to the Earth's atmosphere. The closer to one the ratio between the two measurements of fluxes is, the higher the rate of which particles are being lost.

Figures 4.11 and 4.12 show the 24-hour running mean of the loss cone fluxes together with the ratio of which particles are being lost for the E1 and E3 energy channels, respectively. Looking at these two figures, it is evident that the level of anisotropy varies significantly with geomagnetic activity. The E3 energy channel has a weaker ratio implying a more anisotropic pitch angle distribution compared to the E1 channel. This means that more of the trapped particles in the lower energy channel are being lost to the atmosphere compared to the trapped particles in the higher energy channel.

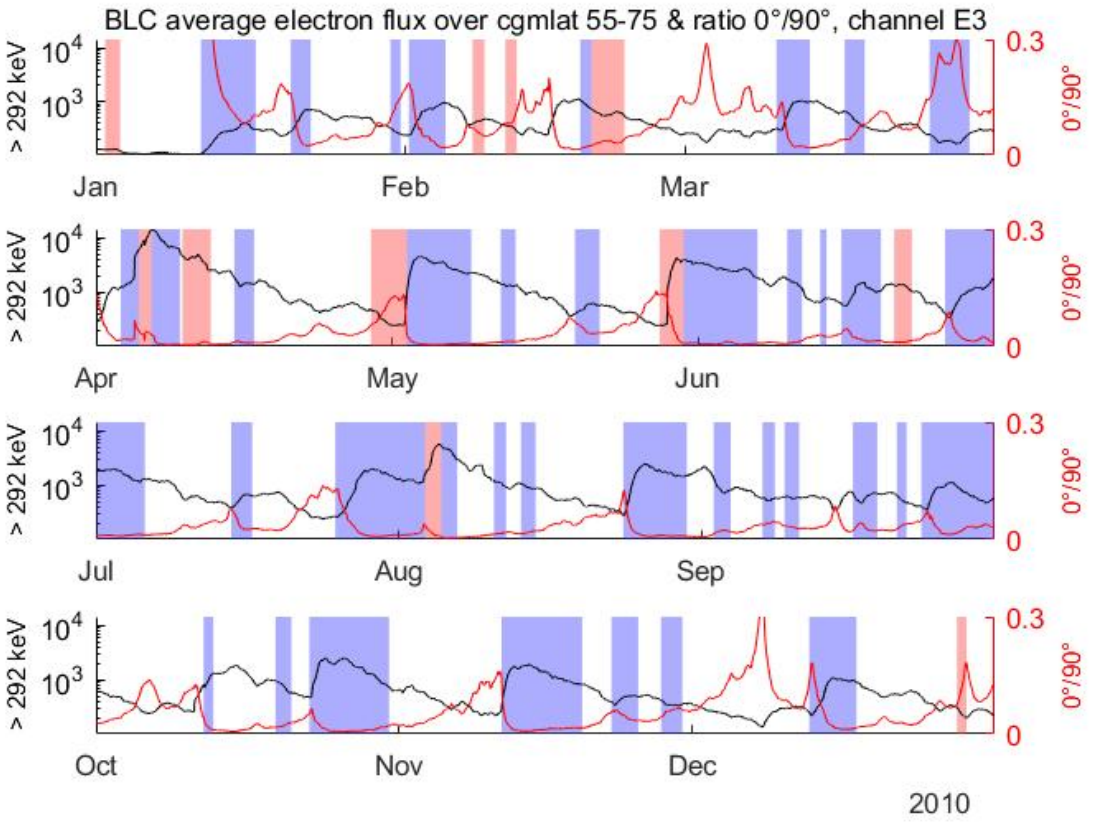

Figure 4.12: Logarithmic line plot of the daily running mean electron flux over CGM latitude 55-75 (black) and the ratio between the 0° and 90° detectors (red) for the E3 channel.

The 90° telescope estimates the number of particles that are trapped close to the edge of the loss cone. Focusing on the storm time evolution, the ratio of the lost and trapped particles for the E1 electrons increases with increasing flux. This relationship appears, however, to change for the higher energies in channel E3. To explore this feature in more detail, Figure 4.13 shows a scatter plot of the ratio over the flux measured by the 90° telescope for channels E1 and E3. The figure shows that when the trapped low energy electron flux increases, corresponding to the main phase of the events, the ratio of particles being lost to the atmosphere also tends to increase. For the higher energy electrons, the ratio decreases as the number of trapped particles grow.

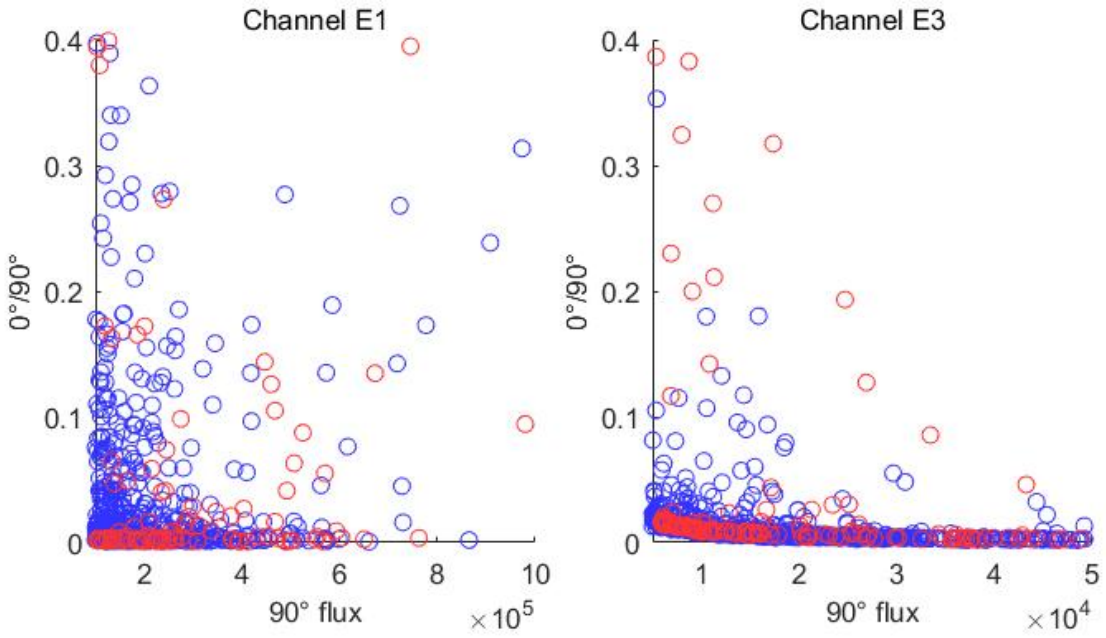

Figure 4.13: Scatter plot of the ratio of the two detectors (0° and 90°) over the electron flux measured by the 90° telescope for channels E1 and E3. The ratio is not calculated from a running mean of the fluxes. Plotted from log-1

4.4 Case study

In this section, we look further into both isolated events and combined events throughout the year 2010. The goal is to get a better understanding of how similar structures and their geoeffectiveness can lead to different responses in EEP. Section 4.4.1 compares the two isolated CIR events in October and November, section 4.4.2 compares the CME+CIR events in May and June, and section 4.4.3 compares the CIR+CME+CIR events in April and August. As ap is deduced from Kp, only the Kp*10 index is presented in this section.

4.4.1 CIRs

The two CIR events in October and November are presented in Figure 4.14. The top panel shows the epsilon parameter, followed by the AE index, the Kp*10 index, the Dst index, and the two energy channels E1 and E3. The time starts and ends 3 days before and after the structure period as indicated by the x-axis where 0 denotes the onset of the CIR events. The two electron flux channels also show the FF and FR shocks occurring during the given period.

Both the October and November events last for about eight days (196 hours and 198 hours, respectively). The energy input to the magnetosphere during the CIR in October is relatively high the first 40 hours after onset, reaching its maximum six hours into the event. Before the onset of the CIR in November, the response in epsilon is relatively strong compared to the October event, and peaks only one hour after onset, after which the energy input continues to stay relatively high for 24 hours. The maximum/minimum values for all the geomagnetic indices are very similar for the two events, as is shown in Table 2: in November and October AE reaches a maximum of $851nT$ and $850nT$, max Kp*10 is 50 and 47, and min Dst is $-41nT$ and $-45nT$, respectively. The response in the geomagnetic indices compared to onset are, however, faster during the event in November. The Kp*10 index is the first to be affected by any geomagnetic disturbances (-17 hours and -21 hours for the October and November events, respectively). During October, the peaks in AE and Kp*10 happen simultaneously (18 hours after onset), while the trough in Dst occurs nine hours later. For the event in November, the AE index peaks about nine hours before the relatively simultaneous peak in Kp*10 and trough in Dst at 10 and 12 hours, respectively. After the minimum trough in Dst, it slowly recovers back to pre-storm values throughout both CIR events.

During both events, the E1 flux increases significantly within the first 24 hours, while the E3 flux is somewhat delayed in comparison. After increasing, the E3 flux, as the E1 flux, decreases slowly throughout the events, but with fewer fluctuations. Looking at Figure 4.14, the E1 fluxes for both events correspond fairly well with the AE and Kp*10 indices. During October, the E1 flux peaks only one hour after the peak in these indices (at 19 hours), while during November, though E1 is relatively high during the peaks of AE and Kp*10, it does not peak until 82 hours after onset. The flux variations in the E3 energy channels during both events do not correspond as well with the different indices.

Figure 4.15 shows a plot of both energy channels on a linear scale. The solid horizontal lines indicate the mean of the flux, while the horizontal dashed lines show the second standard deviation from the mean. The figure also shows the total flux before, during, and after the events indicated by the numbers in the plot. The time lag between the two energy channels during October is 12 hours (E1 peaks at seven hours and E3 at 19 hours). Looking at Figure 4.15 the first significant peak in E3 during November seems to correspond to the second significant peak in E1 at 12 hours, resulting in a time lag of 10 hours. The different shocks do not seem to have any significant impact on any of the parameters presented in Figure 4.14.

Table 3 shows the epsilon parameter for the two CIR events along with the energy dissipation due to Joule heating, energy increase of the ring current, and particle precipitation. The total amount of

energy dissipation (U_T) is presented as the sum of these three energy sinks. There is little difference between the distribution of energy within the magnetosphere (which is based on AE) between the two events. The major difference is seen in the epsilon parameter. The total energy input to the magnetosphere is significantly lower during the CIR in October compared to November ($4.3e16J$ and $6.7e16J$, respectively). Based on this, we would expect the November storm to have higher fluxes. What we see is, however, the opposite.

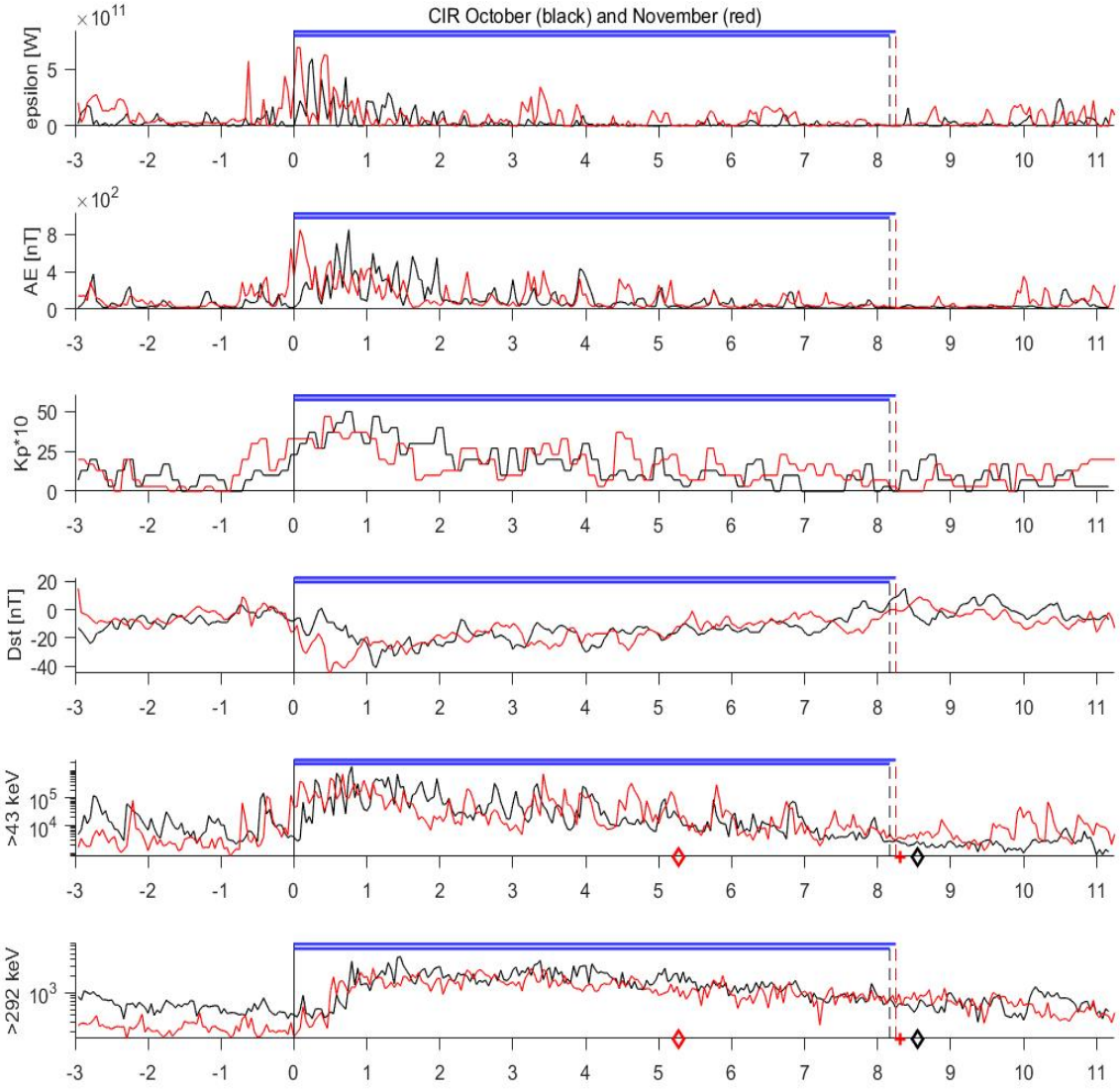

Figure 4.14: From the top all with a one-hour resolution: the epsilon parameter, AE index, Kp*10 index, Dst index, E1 flux, and E3 flux during the two CIR events in October (black) and November (red). 0 indicates the onset of the CIR structure. All panels show the parameters and indices 3 days (72 hours) before and after the CIR event. The two electron flux channel plots show fast forward (+) and fast reverses (◊) shocks during this period.

Neither the indices nor the energy transfer of dissipation provides an obvious reason for the differences in the observed fluxes. Looking at the pre-storm conditions the total flux in both energy channels is higher before the storm in October (see Figure 4.15). This indicates that the difference in particle flux between the two events might be due to pre-storm conditions, and only by knowing the history of the system, a correct storm time flux can be estimated.

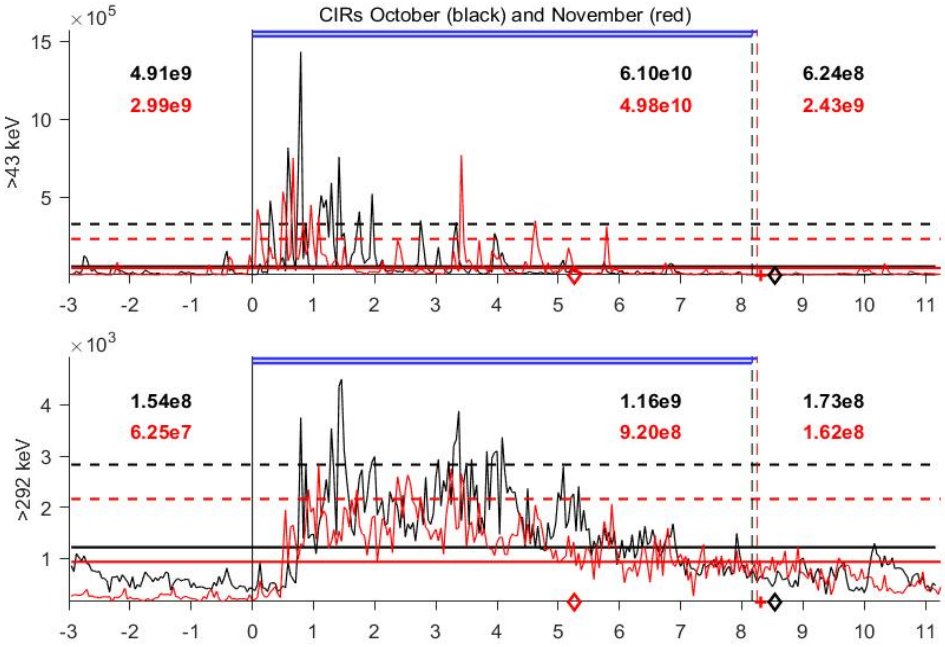

Figure 4.15: The E1 and E3 flux on linear scales for the two CIR events in October (black) and November (red). Same indications as in Figure 4.14. The solid line indicated the mean of the flux while dashed lines indicated the second standard deviation from the mean. This is to highlight differences in timing between the two events and between the two energy channels. The numbers in the text indicate the total amount of electrons precipitating before, during, and after the event.

Table 3: The epsilon parameter, the calculated time-integrated energy depositions (U_A, U_J, and U_R), and the total energy disposition (U_T). The percentage of which the different energy dispositions contribute to U_T is shown in parentheses.

Events	**Epsilon** $[10^{16}J]$	U_A $[10^{16}J]$ (%)	U_J $[10^{16}J]$ (%)	U_R $[10^{16}J]$ (%)	U_T $[10^{16}J]$
CIR					
Oct	4.284	1.596 (20.0)	5.064 (63.6)	1.305 (16.4)	7.965
Nov	6.709	1.674 (20.7)	5.129 (63.3)	1.299 (16.0)	8.102
CME+CIR					
May	9.281	3.255 (20.2)	9.883 (61.2)	3.012 (18.7)	16.150
Jun	18.480	4.265 (19.6)	13.966 (64.1)	3.543 (16.3)	21.775
CIR+CME+CIR					
Apr	13.421	3.468 (17.7)	12.327 (63.0)	3.763 (19.2)	19.558
Aug	11.787	3.960 (19.6)	12.143 (60.1)	4.104 (20.3)	20.207

4.4.2 CME+CIR

The combined events in May and June (CME+CIR) both last for about 10 days in total (244 hours and 238 hours, respectively). In May, the CME is longer and the CIR shorter (88 hours and 156 hours,respectively) compared to the CME and CIR in June (88 hours and 180 hours, respectively). The two combined storms are presented in Figure 4.16 in the same manner as the CIR events in Figure 4.14.

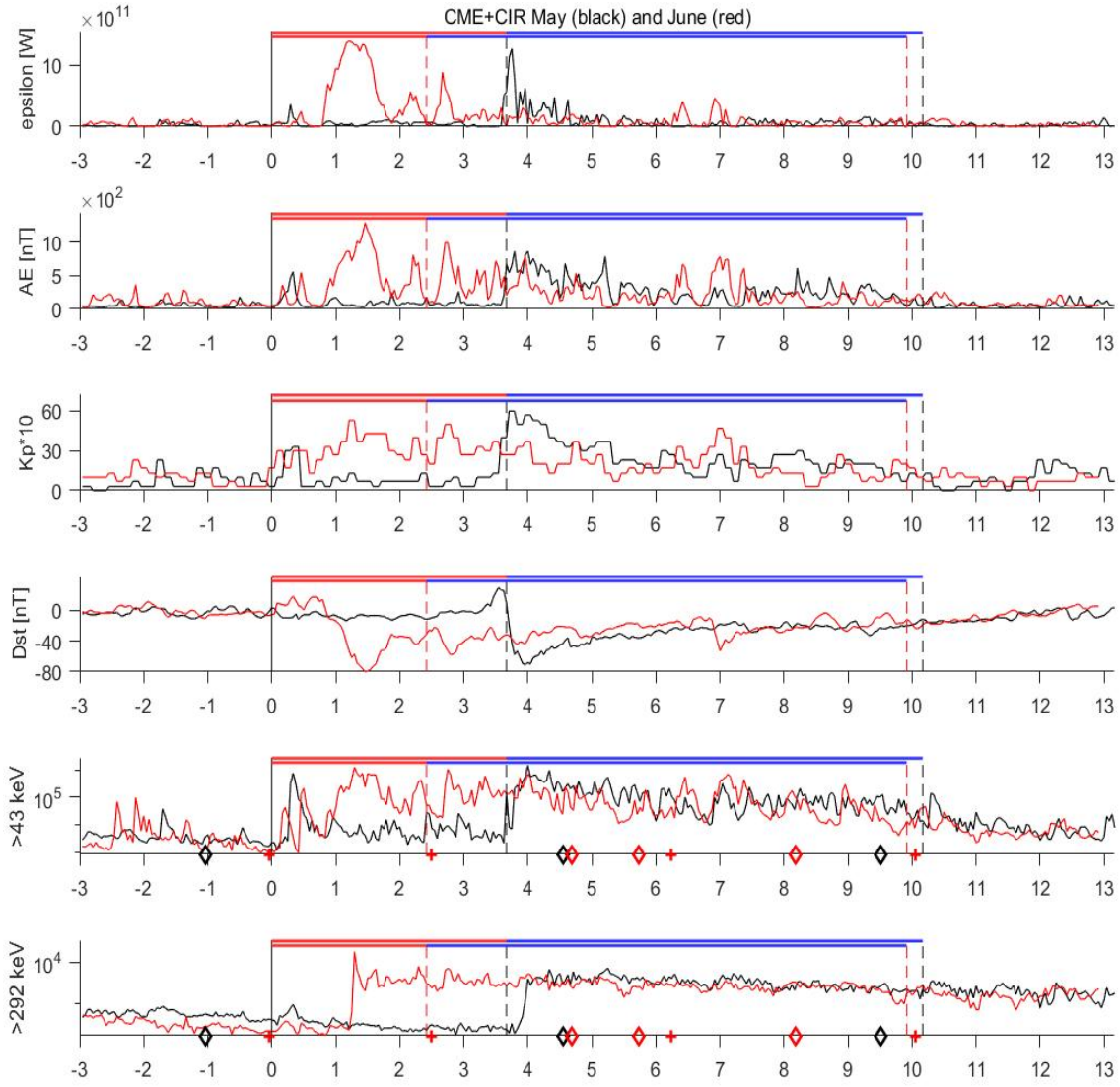

Figure 4.16: Same as Figure 4.14 but for the two combined events (CME+CIR) in May (black) and June (red).

The main difference between the two CME+CIR events is that the CME in June is geoeffective, while the CME in May is not. Except for a small peak in epsilon at 8 hours, the epsilon parameter during May does not increase significantly until the CIR arrives at 88 hours, where it then continues to rise and peak two hours later. During June, three relatively large peaks are found: two during the CME at 29 and 52 hours, and one during the CIR at 64 hours. The largest responses for all the geomagnetic indices are different for the two events, but not in a systematic way: the AE

index is higher in June compared to May (1293 nT and 867 nT, respectively), while the Kp*10 and Dst indices are weaker (53 and -36 nT during June, and 60 and -71 nT during May, respectively). Generally, the magnetic indices correspond well with the variations in epsilon. During both events, the Kp*10 index is the first to respond to any geomagnetic disturbances and the first to reach its maximum peak at 89 and 20 hours during May and June, respectively. The largest responses in AE and Dst occur at 91 and 95 hours during May and 35 and 36 hours during June, respectively. In both cases, the largest response in Dst occurs last, however the SSCs visible during both storms show a relatively early response in Dst.

The E1 flux during both events follows responses in the indices well. In May, E1 increases around the time the CIR arrives and peaks concurrently with a second peak in AE (at 96 hours). A peak is also found at 8 hours which coincides with small peaks in all the other parameters except Dst. In June, there are five separate peaks within the first three days in all indices which can also be seen in E1. The main peak occurs at 31 hours. The E3 flux does not fluctuate as much as the lower energy channel. During both storms, E3 increases sharply, peaks, and then slowly decreases throughout the event. The increase in May at 91 hours coincides with a peak in AE, and the increase in June, with a peak in Kp*10 at 29 hours. The maximum E3 peak in May (at 126 hours), however, does not coincide with any of the other parameters, while the E3 maximum peak in June occurs concurrently with the maximum peak in E1. Once both storms are geoeffective, the fluxes in both energy channels look relatively similar. The time delay between an increase above two standard deviations from the mean flux in the two energy channels during June is zero while in May there is a time lag of 9 hours. The significant peak in E3 during May does, however, coincide with the second peak in E1 (see Figure 4.17). The shocks that occur in May and June do not seem to have an impact on the different parameters or fluxes.

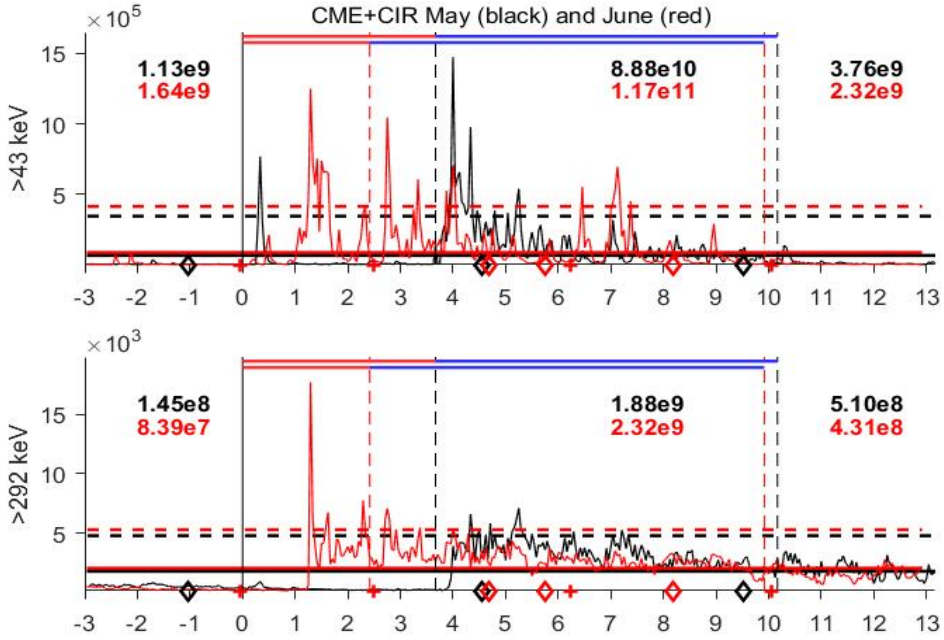

Figure 4.17: Same as Figure 4.15 but for the two CME+CIR events in May (black) and June (red).

The amount of energy coming into the magnetosphere from the solar wind is twice as high in June compared to May. Looking at Figure 4.17, the total average flux is also higher in June, but not by much. This seems to mainly be because the CME in May is not geoeffective. When the flux during May first does increase, however, the number of electrons precipitating is slightly higher in May: ~ 1.4 and ~ 1.2 times more electrons in channel E1 and E3, respectively, during May, compared to

June (within the time frame 96 hours to 243 hours). Looking back at Table 3, the different energy sinks are higher and the amount of energy lost through precipitation is ~ 1.31 times larger in June compared to May.

The cause of the relatively similar flux responses once both storms become geoeffective is not obvious from any of the indices or the energy budget during the events. Looking at the pre-storm conditions, the total flux in the E3 channel during May is significantly higher than that in June which might contribute to enhancing the fluxes once the storm in May becomes geoeffective. However, the pre-storm E1 flux is 1.45 times higher in June compared to May. The non-systematic responses in the indices and the similarities between the fluxes are hard to explain. Defining the onset based on the geomagnetic responses in, e.g., Dst, might help explain some of these features.

4.4.3 CIR+CME+CIR

The two CIR+CME+CIR events in April and August have very different duration: April lasts for six days (144 hours) and August for over 12 days (300 hours). The first CIR is five times longer in August compared to April (221 and 44 hours, respectively). The CMEs and second CIRs have a more similar duration (CMEs 31 and 40 hours, and CIRs 69 and 39 hours for April and August, respectively). The two combined storms are presented in Figure 4.18 in the same manner as the CIR events in Figure 4.14.

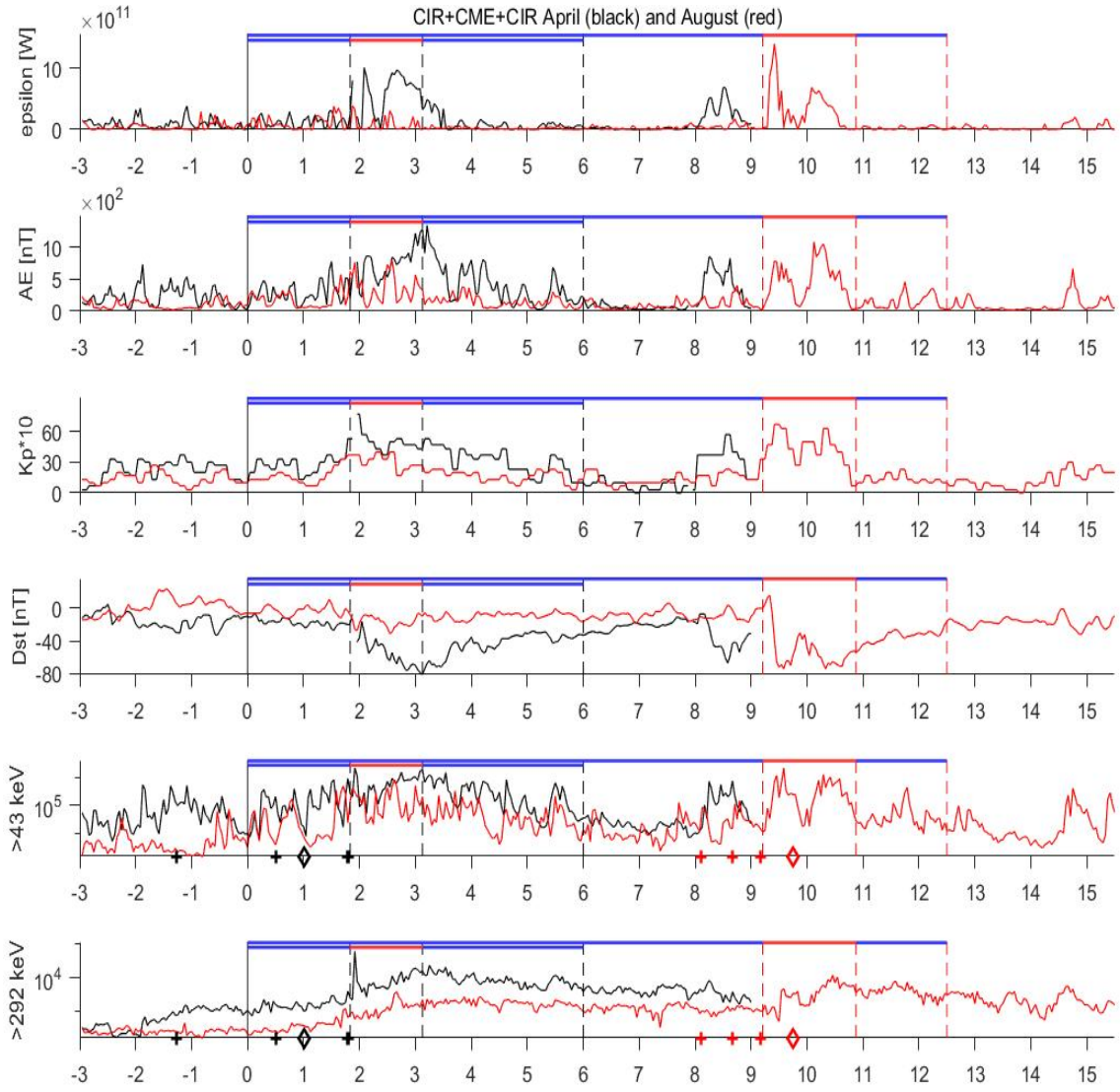

Figure 4.18: Same as Figure 4.14 but for the two combined events (CIR+CME+CIR) in April (black) and August (red).

The main difference in epsilon between the two storms in April and August is that August has a period of very low energy transfer towards the end of the first CIR. Both events show that epsilon peaks twice during the CME (during April epsilon peaks at 50 and 64 hours, and in August at 226 and 242). The increase in epsilon when the CME occurs during April might indicate another peak, but due to lack of data, it is not visible. The geomagnetic responses are stronger in April compared

to August, but not my much: in April and August AE reaches a maximum of $1345nT$ and $1088nT$, max Kp is 77 and 57, and min Dst is $-81nT$ and $-74nT$, respectively. The geomagnetic responses during August all follow the epsilon parameter well. An increase in activity takes place around the time the CME occurs. During the CME, all indices show two peaks/troughs corresponding to the two peaks in epsilon. The first peak in AE and Kp*10 coincide with epsilon (at 226 hours), while Dst reaches its minimum 4 hours later. Some geomagnetic activity during the beginning of the first CIR event is visible before it subsides. In April, the two peaks in epsilon do not cause as clear responses in the indices. A reaction in all indices is, however, found when the CME arrives. During April, the Kp*10 index is the first to peak (at $\sim$ 47 hours), while the maximum responses in AE and Dst are delayed in comparison (77 and 72 hours, respectively). A SSC is visible during the CME in August but is inconclusive during April (due to lack of data).

The E1 electron flux coincides well with the fluctuations in the indices, as does the E3 flux but with fewer variations. It is clear from Figure 4.19 that in April, both the E1 and E3 fluxes peak simultaneously at 46 hours. As the other parameters all increase significantly up to the point of no data it is safe to assume a high peak in these parameters occurs simultaneously as the peaks in flux. During August, E1 peaks around the same time as the largest responses in Dst (at 230 and 247 hours), which is four hours after the peaks in AE and Kp*10. Two small peaks in the E3 flux during the CME (at 230 and 251 hours) are also found. The time delay between an increase above two standard deviations from the mean flux in the two energy channels during April is zero. The following significant responses show a time delay between the two energy channels of about five hours. One of the reasons that the responses in the fluxes during April are so coherent around 46 hours could be due to the FF shock that occurs right before the CME. In August, the responses in E3 barely exceed two standard deviations from the mean. Comparing the second significant response in E1 with the first in E3 there is a time delay of about four hours between the two channels in August. The shocks during the event in August do not seem to have any effect on the parameters or fluxes.

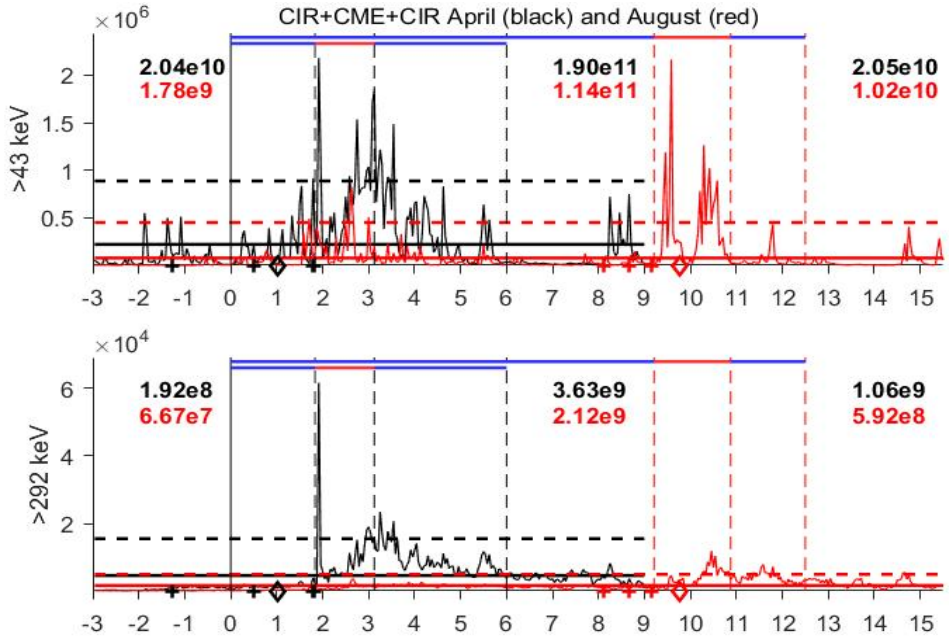

Figure 4.19: Same as Figure 4.15 but for the two CIR+CME+CIR events in April (black) and August (red).

The total amount of energy transferred to the magnetosphere during the event in April is slightly

higher than the event in August (August 88% av April). Table 3 shows that the total amount of energy dissipated throughout the events is very similar. Hence, the depositions of energy do not explain the higher electron flux found in April.

In August, the input energy and all the maximum responses in the indices are $\sim 80 - 90\%$ of what they are in April. Therefore, it is expected that August has a slightly lower flux response (about 80-90% of April). However, the total amount of electron precipitation in August for the two energy channels E1 and E3 is only $\sim 60\%$ of what it is in April. Pre-storm values show that the event in April has substantially more particles that might contribute to the large values in particle flux during the event. Another difference between the two storms is the timing of the CME. In April, the CME occurs when the fluxes are rising, while in August the flux has started decreasing before the CME arrives. Hence, the pre-storm fluxes and timing of the CME are important to take into consideration when predicting EEP responses during these two storms.

5 Discussion

Over the years, while the auroral electron fluxes have been extensively studied, the more energetic electron precipitation has been harder to capture with simple models. Single solar wind variables as well as geomagnetic indexes have been suggested as predictors (e.g., *van de Kamp et al.* [2016]). The following discussion addresses to which extent EEP in the year 2010 complies with previous results with a particular focus on the higher energies. The key questions are: - To what extent do different solar wind structures and their associated shocks affect EEP? - How do geomagnetic indices predict EEP and is the correlation dependent on solar wind structure? - How does the energy transfer to the magnetosphere and the distribution within scale to EEP variations?

5.1 The solar wind structures as predictors for EEP

For simplicity, considering that we are only evaluating one year of data, the category CME-driven includes driving by ejecta, CME sheaths, and magnetic clouds. The category CIR-driven also includes driving by the high-speed streams that follow the CIRs. As the solar wind structures of CMEs and CIRs/HSSs are very different, so is the geomagnetic activity that they drive. CMEs often contain a strong southward Bz, high velocity, and dense plasma, and are therefore known to be related to the strongest geomagnetic storms. CIRs and their associated HSSs typically cause only modest magnetic storms with long recovery periods. In the following, we discuss to what extent different solar wind structures and their associated shocks affect EEP.

Table 4 shows an overview of the average electron flux during the different geomagnetic storms in both the E1 and E3 energy channels. The table also shows the ratio between the two channels as a percentage. The strongest geomagnetic storms in 2010 were associated with CMEs. However, the year was dominated by CIRs/HSSs, which contributed to most of the total EEP throughout the year. This is consistent with what *Asikainen and Ruopsa* [2016] found, who studied solar wind drivers and their annual effects on EEP from 1979 to 2013 and concluded that HSSs nearly always contribute to the largest amount of annual electron flux.

As there are few isolated CME-driven storms in the year 2010, it is hard to compare the CMEs within combined events, to isolated ones. However, we do have two isolated geoeffective CMEs: one in April, and one in December. The isolated CME-associated storm in April occurs only seven hours after an intense combined storm. The average electron flux in the E3 energy channel during this period is significantly higher compared to other CME-driven storms throughout the year. The average E1 flux is, however, relatively low compared to other geoeffective CMEs within combined events. The pre-storm conditions likely contribute to the efficiency that this CME has on the E3 flux as it occurs right after the combined April storm. Looking at the isolated CME in December, which does not have any high geomagnetic activity before the storm, the amount of EEP is noticeably low compared to all other storms.

Considering the CME-driven storms within combined events, the CMEs occurring between two CIRs seem to be associated with the highest average electron fluxes in both energy channels compared to all other storms. These periods are also associated with high solar wind velocity and a strong negative Bz component. Based on the limited data, it appears that CMEs associated with CIRs, especially preceding CIRs, lead to higher average electron fluxes.

Relative to the number of electrons precipitating in the E1 energy channel during a storm, the percentage in which the number of electrons precipitating in the E3 energy channel is generally largest during CIR-driven storms. This is consistent with *Kataoka and Miyoshi* [2006] who found that, on average, CIR-associated storms are more effective in $> 300keV$ flux enhancement at geosynchronous orbit than CME-associated storms.

Table 4: Events and the average hourly electron flux during the events for the energy channels E1 and E3. The last column shows the percentage of the ratio E3/E1. The events marked with purple show the different solar wind structures associated with the combined events.

Event	Period (2010)	E1	E3	E3 / E1 * 100
CIR	20.Jan - 22.Jan	5.87e4	533	0.91
CIR	10.Mar - 13.Mar	1.12e5	752	0.67
CIR	03.Apr - 05.Apr	1.79e5	1.60e3	0.89
CME	05.Apr - 06.Apr	7.17e5	1.04e4	1.45
CIR	06.Apr - 09.Apr	3.25e5	8.92e3	2.74
CIR+CME+CIR	03.Apr - 09.Apr	3.65e5	6.99e3	1.92
CME	09.Apr - 12.Apr	8.04e4	3.92e3	4.88
CIR	15.Apr - 16.Apr	3.43e4	1.38e3	4.02
CME	28.Apr - 02.May	2.57e4	312	1.21
CIR	02.May - 08.May	1.44e5	3.16e3	2.19
CME+CIR	28.Apr - 08.May	1.01e5	2.14e3	2.12
CME	28.May - 30.May	1.87e5	2.29e3	1.22
CIR	30.May - 06.Jun	1.20e5	2.85e3	2.38
CME+CIR	28.May - 06.Jun	1.36e5	2.71e3	1.99
CIR	15.Jun - 19.Jun	6.25e4	1.03e3	1.65
CIR	26.Jun - 05.Jul	8.29e4	1.29e3	1.56
CIR	25.Jul - 03.Aug	6.38e4	1.23e3	1.93
CME	03.Aug - 05.Aug	3.90e5	4.03e3	1.03
CIR	05.Aug - 06.Aug	5.36e4	3.97e3	7.41
CIR+CME+CIR	25.Jul - 06.Aug	1.06e5	1.96e3	1.85
CIR	24.Aug - 30.Aug	1.10e5	1.63e3	1.48
CIR	23.Sep - 30.Sep	5.59e4	708	1.27
CIR	12.Oct	1.03e5	982	0.95
CIR	22.Oct - 30.Oct	8.64e4	1.64e3	1.90
CIR	11.Nov - 19.Nov	6.98e4	1.29e3	1.85
CME	28.Dec - 29.Dec	6.07e4	231	0.38

The combined events show large values of average electron fluxes in both the E1 and E3 energy channels compared to all isolated events. Naturally, the individual events within the combined storms, when geoeffective, show large values in EEP as well. Even when the preceding CME in May is not geoeffective, the following CIR has greater effects on the magnetic indices (except AE) compared to the isolated CIRs, and a relatively large impact on electron precipitation. In fact, all CIR events that follow CMEs have a distinctly higher ratio between the E3 and E1 energy channels compared to the isolated CIR events. Hence, it appears that the preceding CME provides a favorable premise for the relativistic electron flux precipitation.

Zhang et al. [2008] found similar results evaluating the geoeffectiveness of CIRs. They identified 345 CIRs during Solar Cycle 23 (1996-2005). 157 were pure CIRs, which caused mainly weak and moderate storms, while the 188 combined events could drive significantly stronger geomagnetic responses. The mechanism why CIRs following a CME will cause relative more relativistic electron precipitation compared to low energy fluxes is not readily evident. One possibility is that the trapped electrons have a favorable energy distribution. Another option is that there already exist numerous seed particles. The strong response after the not geoeffective CME in May might support the latter. *Borovsky and Denton* [2013] points out that a positive Bz is associated with a buildup of the outer plasma sheet due to the larger solar wind density. As the plasma sheet provides the seed particles that are accelerated to higher energies, the filling of the plasma sheet might offer a favorable precondition. Most of the combined CIR events, however, follow a geoeffective CME which might also provide plasma sheet seed particles and/or a radiation belt with elevated energies.

These findings indicate that different solar wind structures do have different effects on EEP. To get a clearer picture of these differences one would need better statistics on both isolated and combined events. We can, however, conclude that knowing what solar wind drivers are present during a storm and before a storm is important in order to fully understand the nature of EEP.

5.1.1 The role of shocks

In general, we do not find a large impact from shocks. The FR shocks give no measurable responses in any of the EEP parameters presented in this study. However, the FF shock during the CME in April resulted in a relatively simultaneous, sudden increase in EEP in all energy channels. This is the storm that had the highest solar wind velocity throughout the entire year. *Kataoka and Miyoshi* [2006] found that during solar cycle 23 from January 1996 to December 2004, 96% of isolated CME-driven storms with $Dst < -100nT$ had shocks associated with the arrival of the CME. The geomagnetic storms during the year 2010 were categorized as either weak or moderate, and most of them had relatively low solar wind speed associated with them. This might be one of the reasons for the low occurrence of shocks during the CMEs in 2010, as 2010 is at the start of the inclining phase of the solar cycle. *Kilpua et al.* [2017b] found that CME-driven fast shocks are particularly important structures in the collisionless solar wind plasma and effective accelerators of charged particles. In this study, no such conclusion can be made due to a lack of isolated CMEs and associated FF shocks. Further research on CMEs and FF shocks is therefore necessary for understanding the effects they have on EEP.

5.2 The geomagnetic indices as predictors for EEP

In previous studies (e.g., *van de Kamp et al.* [2016]) geomagnetic indices have been used to predict particle precipitation. The following discussion addresses hoe geomagnetic indices predict EEP and if the correlation is dependent on solar wind structure. Looking back at Figures 4.15, 4.17 and 4.19, there is an apparent correlation between the particle fluxes and the different geomagnetic indices. The linear Pearson's correlation coefficient, r, between the different geomagnetic indices and the particle precipitation in the E1 and E3 energy channels throughout the entire year of 2010 is shown in Table 5. With a high number of data points (n=8760), we get a p-value close to zero. This means the correlation was considered significant in all cases.

For the particles precipitating in the E1 energy channel, the highest correlation is with the AE index (0.71), and the lowest with the Dst index (-0.54), meaning that 50% of the variation in E1 can be explained by the variation in AE, and 20% by Dst. As for the particles precipitating in the E3 energy channel the correlation to any of the indices is relatively low compared to that of E1. The highest correlation in E3 is, however, found to be with the Dst index (-0.53). The reduced correspondence is likely due to the time lag between precipitation of E1 and E3 particles.

Table 5: The linear Pearson's correlation coefficient r (percentage in brackets) between the geomagnetic indices and the particle precipitation in the E1 (r1) and E3 (r3) energy channels throughout the year 2010.

	r1 (%)	r3 (%)
AE	0.71 (50%)	0.44 (19%)
ap	0.66 (44%)	0.45 (20%)
Kp	0.58 (34%)	0.36 (13%)
Dst	0.54 (29%)	0.53 (28%)

Looking at the different solar wind structures that were geoeffective (see Table 6), a higher correlation between the fluxes and AE is found during CME-associated storms: 1.1 and 1.4 times larger in the E1 and E3 energy channels, respectively, compared to CIR-associated storms. In general, CME-driven storms seem to give the highest correlation between fluxes and all the indices. One exception is in the E3 channel where CIR-associated storms have a higher correspondence with the Dst index.

Table 6: Same as in Table 5 but for the different solar wind structures that were geoeffective.

	CIR r1 (%)	CME r1 (%)	CIR r3 (%)	CME r3 (%)
AE	0.69 (48%)	0.75 (56%)	0.37 (14%)	0.51 (26%)
ap	0.63 (38%)	0.62 (38%)	0.29 (8%)	0.48 (23%)
Kp	0.60 (36%)	0.63 (40%)	0.27 (7%)	0.40 (16%)
Dst	0.50 (25%)	0.63 (40%)	0.60 (36%)	0.45 (20%)

For the year 2010, the ap index can account for 44% of the yearly E1 EEP variability, but only 20% of the variability in E3. *van de Kamp et al.* [2016] developed a model for $30 - 1000keV$ EEP, based on precipitation data from the 0° detector on the low Earth orbiting POES satellites in the period $2002 - 2012$, which was scaled to the daily resolution of the geomagnetic index Ap. The model parameterized by the Ap index has been recommended as part of the solar forcing for Coupled Model Intercomparison Project (CMIP) 6 (v3.2; *Matthes et al.* [2017]). To assess the accuracy of the Ap model, *Tyssøy et al.* [2019] compares the modeled electron fluxes with estimates of the loss cone fluxes, also used in this study. They found that, in general, the AP model fails to reproduce the flux level variability associated with the strongest CME storms ($Ap > 40$) and the duration of the CIR storms, as the model generally captures the initial phase of the CIR storm fluxes, but falls short in respect to reproducing elevated flux levels during the recovery phase. Considering the line

plots of the ap index and the E1 flux in Figure 5.1, we can see some of the same tendencies in the recovery phase of storms during the year 2010, especially during the high responses in April, July, and November (E1 (black) lingers after it peaks).

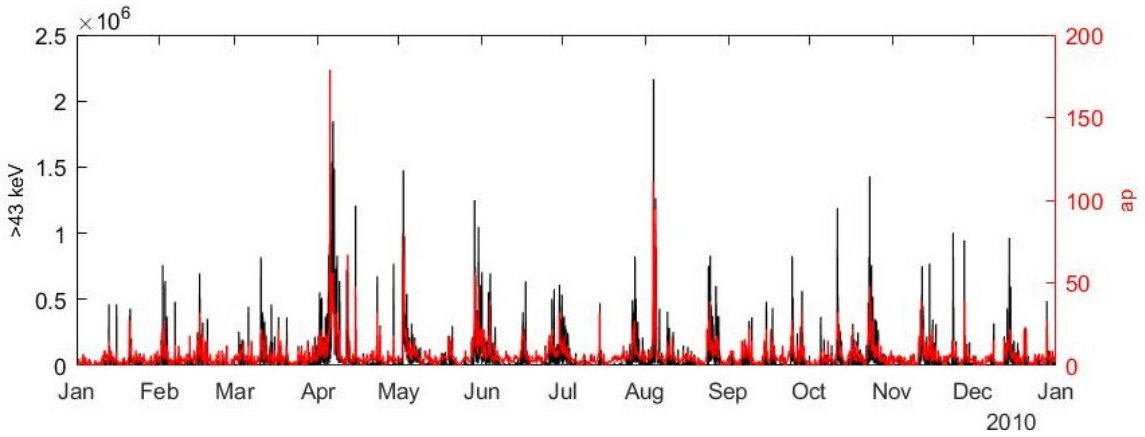

Figure 5.1: A line plot of the hourly ap index and the hourly flux in the E1 energy channel. It illustrates that while the E1 flux and ap index peak at approximately the same time, the ap index falls more abruptly compared to the flux.

The Dst index can account for $\sim$ 30% of the yearly E1 and E3 variability. *van de Kamp et al.* [2016] also developed a Dst-dependent EEP model. Though they evaluate that the models perform almost equally well, the Ap model was found to have an advantage over the Dst model. One of the disadvantages mentioned in the Dst model was the zero flux values arising during quiet times ($Dst \geq 0nT$) and sudden storm commencements. Table 6 shows that the Dst index has a higher correlation with CME-associated storms in E1, but a stronger correlation with CIR-driven storms in E3. This could be due to the long recovery phase found for several geomagnetic storms. While AE and ap fall relatively fast to quiet levels in the recovery phase of a storm, the Dst shows weak disturbances for a longer period. Hence, the correlation increases for the CIR storms which are known for their long recovery phases. *van de Kamp et al.* [2016] also point out that both the Ap and Dst models measure relatively inaccurately for low flux levels, this could affect the result in this study as the year 2010 is during solar minimum. In general, for the entire year 2010, the geomagnetic indices fall short in predicting the E3 fluxes, at least without considering time lag.

To work around the delayed response in the E3 fluxes, Table 7 shows the average hourly values of the AE, ap, Kp*10, and Dst indices for all geomagnetic storms in 2010, including the individual solar wind drivers associated with the combined events (purple). The average fluxes in the E1 and E3 energy channels are also presented. In general, strong (weak) responses in the geomagnetic indices lead to strong (weak) responses in electron precipitation. As the average electron precipitation is generally relatively strong during combined events compared to isolated events, so is the average electron flux.

The strongest average geomagnetic responses occur during the CMEs between two CIR events in April and August. This is also the period where the average electron flux in both the E1 and E3 energy channels is highest. The main difference between these two storms, when considering the geomagnetic responses, is the AE index, as it is 1.6 times larger during April compared to August. The EEP response is also found to be stronger in April where the average flux in E1 and E3 are 1.8 and 2.6 times larger than August, respectively. This fits well with AE having a high correlation with the fluxes during CME-driven storms.

Geomagnetic storms with approximately the same responses in the geomagnetic indices, e.g., the two CIRs in June and July or the two CIRs in October and November, do not have the same responses in electron precipitation. The geomagnetic indices, in general, have relatively weak correspondence

with the fluxes during CIR-driven storms, and therefore, might not be adequate in predicting the differences in flux between them. The CIRs in July and October have stronger responses in both the E1 and E3 energy channels compared to the CIRs in June and November, respectively. Looking back at Figure 4.15, pre-storm conditions could contribute to the difference in particle precipitation between the two CIR events in October and November, as the total number of pre-storm electron precipitation is higher in October.

Table 7: The average hourly response in the geomagnetic indices, Dst, ap, Kp*10, and AE, and the electron flux in the E1 and E3 energy channels during the events of 2010. Events marked with purple show the different solar wind structures associated with the combined events.

Event	Period (2010)	AE [nT]	ap/Kp*10	Dst [nT]	E1	E3
CIR	20.Jan - 22.Jan	124	9/17	-18	5.87e4	533
CIR	10.Mar - 13.Mar	165	8/19	-13	1.12e5	752
CIR	03.Apr - 05.Apr	291	15/28	-17	1.79e5	1.60e3
CME	05.Apr - 06.Apr	775	56/50	-54	7.17e5	1.04e4
CIR	06.Apr - 09.Apr	399	19/30	-43	3.25e5	8.92e3
CIR+CME+CIR	03.Apr - 09.Apr	447	26/34	-37	3.65e5	6.99e3
CME	09.Apr - 12.Apr	186	11/17	-27	8.04e4	3.92e3
CIR	15.Apr - 16.Apr	75	6/11	-19	3.43e4	1.38e3
CME	28.Apr - 02.May	104	5/10	-4	2.57e4	312
CIR	02.May - 08.May	285	15/25	-30	1.44e5	3.16e3
CME+CIR	28.Apr - 08.May	220	11/19	-21	1.01e5	2.14e3
CME	28.May - 30.May	439	19/32	-26	1.87e5	2.29e3
CIR	30.May - 06.Jun	253	11/22	-25	1.20e5	2.85e3
CME+CIR	28.May - 06.Jun	299	13/24	-25	1.36e5	2.71e3
CIR	15.Jun - 19.Jun	188	9/19	-11	6.25e4	1.03e3
CIR	26.Jun - 05.Jul	188	9/20	-13	8.29e4	1.29e3
CIR	25.Jul - 03.Aug	167	8/18	-9	6.38e4	1.23e3
CME	03.Aug - 05.Aug	476	44/43	-51	3.90e5	4.03e3
CIR	05.Aug - 06.Aug	141	5/13	-34	5.36e4	3.97e3
CIR+CME+CIR	25.Jul - 06.Aug	205	12/20	-18	1.06e5	1.96e3
CIR	24.Aug - 30.Aug	189	11/21	-15	1.10e5	1.63e3
CIR	23.Sep - 30.Sep	114	7/16	-10	5.59e4	708
CIR	12.Oct	242	11/23	-38	1.03e5	982
CIR	22.Oct - 30.Oct	130	9/18	-16	8.64e4	1.64e3
CIR	11.Nov - 19.Nov	130	9/18	-17	6.98e4	1.29e3
CME	28.Dec - 29.Dec	232	11/20	-14	6.07e4	231

Figures 5.2 and 5.3 show a scatter plot of the average hourly geomagnetic indices and electron fluxes in the E1 and E3 energy channels as presented in Table 7, respectively. The blue circles indicate CIR-driven storms, the red CME-driven storms, and the yellow combined events. Individual solar wind structures part of combined events are indicated by solid circles. The upper right plot shows that the correlation between the AE and E1 flux is relatively linear. The same goes for the ap index. The correlation between the Dst index and E1, however, is more scattered.

Using the average values of the fluxes eliminates the effects of the delay between the E1 and E3 energy channels. From Figure 5.3 the relationship between E3 and the AE and ap index is not as clear. Focusing only on the CIR-associated storms, the correspondence appears closer to linear. This could be due to the duration of CME-driven storms not being long enough to enhance particles to relativistic energies.

These findings indicate that there is, to some degree, a correlation between the geomagnetic indices and EEP. As the correlation does seem to depend on different solar wind drivers, including them in a possible prediction model would be necessary. The findings in this thesis indicate that knowing the pre-storm conditions would also help evaluate the correlations between indices and fluxes. Again, to get a clearer picture of how the geomagnetic indices scale to EEP, better statistics on geomagnetic

storms would be needed. Storms during different periods of the solar cycle would also be of interest as *Tyssøy et al.* [2019] mentions that the degree to which the Ap model can reproduce general flux levels and short term variability is dependent on the chosen phase of the solar cycle.

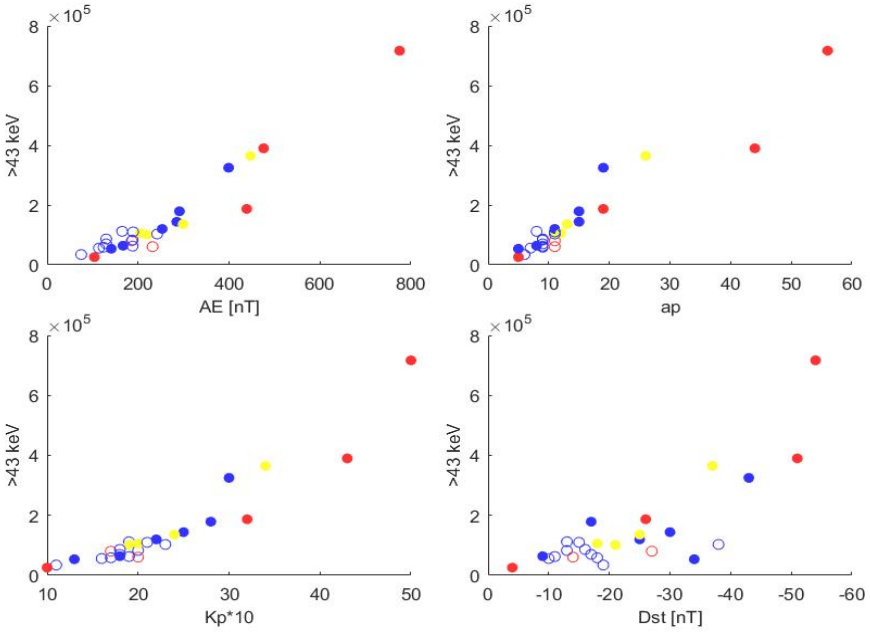

Figure 5.2: A scatter plot of the average hourly geomagnetic indices and electron fluxes in the E1 energy channel for all geomagnetic storms in 2010. Blue indicated CIRs, red CMEs, yellow combined events, and filled inn circles indicate the individual solar wind structures that are part of the combined events.

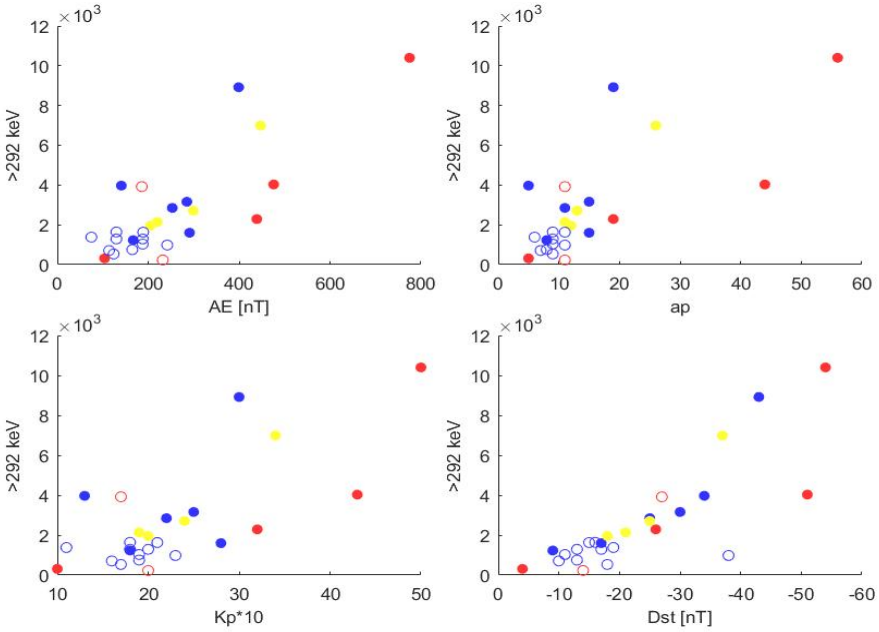

Figure 5.3: Same as in Figure 5.2 for the E3 energy channel.

5.3 The energy budget as a predictor for EEP

The energy that accelerates and scatters the magnetospheric electrons into the atmosphere ultimately comes from the solar wind. The single most important parameters to describe the efficiency of this coupling is the solar wind speed and direction of the northward component of the IMF, expressed as the solar wind electric field. A more accurate description of the energy input, given in SI units, is the epsilon parameter. In the following, we discuss how the energy transfer to the magnetosphere and the distribution within scales to EEP variations?

Ødegaard et al. [2017] investigated 41 geomagnetic storms caused by isolated CIRs from 2006 to 2010. They found that storms with increased precipitation of $>\sim 300keV$ and $>\sim 750keV$ fluxes have higher energy input from the solar wind quantified by the epsilon parameter and corresponding higher geomagnetic activity. Comparing pre- and post-storm fluxes, they showed that the energy input from the solar wind to the magnetosphere was larger for storms where the post-storm $>\sim 750keV$ flux was more than twice as large as the pre-storm $>\sim 750keV$ flux. Together with the longer duration of enhanced solar wind velocity, the solar wind electric field stands out as a possible parameter to predict whether a storm will cause enhanced precipitation with relativistic energy in the recovery phase. However, the two isolated CIR events in October and November do not appear to follow this hypothesis considering absolute values. The epsilon parameter was ~ 1.57 times higher in November compared to October. The average fluxes, on the other hand, were ~ 1.25 and ~ 1.27 times higher for the E1 and E3 energy channels in October compared to November. We note that *Ødegaard et al.* [2017] discussed changes in flux and not absolute values. The pre-storm conditions show that the amount of electron precipitation is higher before the event in October in both energy channels. This indicates that the pre-storm conditions might be the pre-requisite factor of the larger electron flux in October.

The epsilon parameter was largest during the combined event in June, reaching $18.480e6J$ within the ~ 10 days of the event. The combined event in April, lasting ~ 6 days, came in second to largest with epsilon reaching $13.421J$. However, the flux of precipitating electrons was higher during April. Hence, based on the observations in 2010, the epsilon parameter alone is not a sufficient predictor for EEP.

The total energy, U_T, shared between the auroral flux (U_A), Joule heating (U_J), and ring current injection (U_R), appears to be fairly equal in all storms: 19.6%, 62.6%, and 17.8%, respectively. *Østgaard et al.* [2002a] found the total time-integrated energy dissipation over the duration of the substorms in their paper from U_A, U_J, and U_R on average to be 29%, 56%, and 15%, respectively, while *Tenfjord and Østgaard* [2013] found the following distributions: 23%, 47.5%, 29.5%, respectively. The 2010 storms support that U_J acts as the main energy sink, but the degree in which it contributes to U_T exceeds that of both *Østgaard et al.* [2002a] and *Tenfjord and Østgaard* [2013]. Unlike in these papers, we find that the contribution of U_A is weaker. Looking back at Table 3, the extent to which U_A throughout an event is scaled to E1 and E3 is low, even though it is based on the AE index which is found to have the highest correspondence to EEP. The highest (lowest) value of U_A during the combined events do not correspond to the events with the highest (lowest) total/average electron flux.

Østgaard et al. [2002b] presents two equations for calculating U_A; one with the AE index, and one with the AL index. In this paper, the AE index was used, while *Tenfjord and Østgaard* [2013] and *Østgaard et al.* [2002a] used the expression with AL. It has been recommended ([*Ahn et al.*, 1999]) to use the AU and AL indices separately rather than the combined AE index as AU and AL seem to be governed by different physical processes (see *Østgaard et al.* [2002b]). The values used for calculating U_A in *Østgaard et al.* [2002b] are only valid when the stations used for calculating the geomagnetic indices are well located due to the regions of intense precipitation. In this study, this was not checked. Also, the data in *Østgaard et al.* [2002b] was from summertime conditions, while in this paper storms throughout an entire year were considered. Hence, U_A might not give an accurate

representation of the energy lost through particle precipitation as it is a rough estimate. It is worth mentioning that *Østgaard et al.* [2002b] conclude that the AL index, and not the AE index, should be used to estimate U_A.

Table 3 shows that the epsilon parameter is underestimated being that U_T, on average, is ~ 1.53 times larger. That the epsilon parameter does not provide enough energy to balance U_T is similar to what *Østgaard et al.* [2002a] found but in contrary to what *Akasofu* [1981] and *Lu et al.* [1998] reported. According to *Østgaard et al.* [2002a], the main reason for this difference is that the U_A (and U_J) estimated in these studies is 2-4 times smaller compared to their study. It is also argued that because the magnetosphere stores energy from the solar wind, the two values do not necessarily need to balance each other out. Hence, the comparison of the epsilon parameter to U_T might further support the hypotheses of a pre-storm premise.

Another possibility is that the epsilon parameter presented here inaccurately describes the solar wind energy transfer to the magnetosphere. *Kilpua et al.* [2017a] mentions the importance of the Alfvèn Mach number as a parameter for controlling the coupling efficiency. *Tenfjord and Østgaard* [2013] found that, in general, the epsilon parameter underestimates the energy input when looking at long time series (days - 13 years). They conclude that the dynamic coupling function presented in their paper, being dependent on the Alfvèn Mach number, to perform better than the epsilon parameter.

These findings indicate that the epsilon parameter alone is not a sufficient predictor for EEP as higher energy transfer during one storm compared to a similar storm does not guarantee higher fluxes. Pre-storm conditions might be a pre-requisite factor as higher pre-storm fluxes seem to highly affect the flux responses during a storm. In this study, U_A is poorly scaled to EEP which further strengthens the need for a new energy sink estimation for EEP.

6 Conclusion and future work

CME- and CIR-driven geomagnetic storms have different effects on EEP. Combined events result in the greatest electron fluxes. Even when a CME preceding a CIR is not geoeffective, the flux during the following CIR is high compared to isolated events. Though CIR-associated storms are generally more efficient in enhancing E3 fluxes, the CME-driven geomagnetic storms occurring between CIR events result in the highest E1 and E3 electron fluxes. The impact from shocks during 2010 was minimal, but the storm in April indicates that FF shocks could have a greater impact during highly active CMEs.

The correlation between geomagnetic indices and EEP during geomagnetic storms in 2010 is dependent on solar wind drivers. The best correlation was found between AE and the E1 flux during CMEs. Generally, the correlation between the indices and both the E1 and E3 flux was highest during CME-associated storms. Overall, the geomagnetic indices fall short in predicting the E3 flux. Averaging the fluxes eliminates the time-lag between E1 and E3 and shows that the correlations between the indices and the higher energy flux during CIR-associated storms are higher compared to CME-driven storms.

The epsilon parameter is somewhat scaled to EEP (minimum (maximum) values correspond to minimum (maximum) values of EEP flux). However, it is not sufficient to look at the epsilon parameter alone as higher energy transfer during one storm compared to a similar storm (same driver with relatively equal duration and geomagnetic responses) does not guarantee higher fluxes. The extent to which the energy disposition U_A throughout an event is scaled to E1 and E3 was found to be low, even though it is based on the AE index which had the strongest correlation to EEP. The highest (lowest) value of U_A during the combined events did not correspond to the events with the highest (lowest) total/average electron flux.

Knowing the solar wind drivers, geomagnetic responses, and energy transfer during a geomagnetic storm are often used separately for EEP prediction. However, we have found that they are not sufficient to predict EEP flux responses and that they should be used combined. The order of events and pre-storm flux conditions were found to be of great importance as they contribute to the efficiency of flux enhancements during geomagnetic storms. Knowing the pre-storm conditions also helps evaluate the correlation between geomagnetic indices and EEP as storms with relatively equal geomagnetic responses give different flux responses. This means that the chemistry-climate models used today lack the knowledge they need to accurately predict EEP and that better estimations of energy transfer and sinks, especially energy lost through particle precipitation, is needed.

To get a clearer picture of how different solar wind structures, geomagnetic indices, and EEP are linked to one another, one would need better statistics on both isolated and combined events, as well as knowledge of pre-storm conditions. However, the parameters looked at in this study do not give the entire picture of what is happening from particles coming into the magnetosphere to them being lost in the Earth's atmosphere. Other potential phenomena that should be investigated simultaneously are magnetospheric particle acceleration through wave-particle interactions, substorms, and the initial state of the radiation belts. Further research on CMEs and FF shocks during more active periods is also of interest. Researching all these phenomena over a longer time, e.g., an entire solar cycle, will lead to a more accurate EEP parameterization. This is left for future research.

7 Abbreviations

BLC	Bounce Loss Cone
CIR	Corotating Interaction Region
CME	Coronal Mass Ejection
EEP	Energetic Electron Precipitation
ELF	Extremely Low Frequency
EMIC	Electromagnetic Ion Cyclotron
EPP	Energetic Particle Precipitation
EUMETSAT	European Organization for the Exploitation of Meteorological Satellites
CGM	Corrected GeoMagnetic
GSM	Geocentric Solar Magnetospheric
HCS	Heliospheric Current Sheet
HSS	High Speed Solar Wind Stream
ICME	Interplanetary Coronal Mass Ejection
IMF	Interplanetary Magnetic Field
LRO	Low Resolution
MEPED	Medium Energy Proton and Electron Detector
METOP	Meteorological Operational Satellite Program of Europe
MLT	Magnetic Local Time
NOAA	National Oceanic and Atmospheric Administration
POES	Polar Orbiting Environmental Satellite
SSC	Storm Sudden Commencement
SSI	Solar Spectral Irradiance
TSI	Total Solar Irradiance

8 Bibliography

References

Ahn, B. H., et al. (1999), Climatological characteristics of the auroral ionosphere in terms of electric field and ionospheric conductance, *Journal of Geophysical Research: Space Physics*, *104*, doi: 10.1029/1999JA900043.

Akasofu, S. I. (1981), Energy coupling between the solar wind and the magnetosphere, *Space Science Reviews*, *28*, doi:10.1007/BF00218810.

Asikainen, T., and M. Ruopsa (2016), Solar wind drivers of energetic electron precipitation, *Journal of Geophysical Research: Space Physics*, *121*, doi:10.1002/2015JA022215.

Bame, S. J., et al. (1976), Solar cycle evolution of high-speed solar wind streams, *Astrophysical Journal*, *207*, 977–980.

Baumjohann, W., and R. A. Treumann (1996), *Basic Space Plasma Physics*, Imperial College Press.

Borovsky, J. E., and M. H. Denton (2006), Differences between cme-driven storms and cir-driven, *Journal of Geophysical Research: Space Physics*, *111*, doi:10.1029/2005JA011447.

Borovsky, J. E., and M. H. Denton (2013), The difference between storms driven by helmet streamer cirs and storms driven by pseudostreamer cirs, *Journal of Geophysical Research: Space Physics*, *118*, doi:10.1002/jgra.50524.

Carrigan, C. R., and D. Gubbins (1979), The source of the earth's magnetic field, *Scientific American*, *240*(2), 118–133.

Evans, D. S., and M. S. Greer (2004), Polar orbiting environmental satellite space environment monitor - 2: Instrument descriptions and archive data documentation, *NOAA Technical Memorandum version 1.4*.

Forsyth, B. (2001), Ulysses and the reversal of the solar magnetic field, http://www.sp.ph.ic.ac.uk/ forsyth/reversal/, Accessed 2020-06-15.

Gjerloev, J. W. (2012), The supermag data processing technique, *J. Geophys. Res.*, *117, A09213*, doi:10.1029/2012JA017683.

Gonzalez, W. D., et al. (1994), What is a geomagnetic storm?, *Journal of Geophysical Research: Space Physics*, *99*, doi:10.1029/93JA02867.

Hamilton, D. C., et al. (1988), Ring current development during the great geomagnetic storm of february 1986, *Journal of Geophysical Research: Space Physics*, *93*, doi: 10.1029/JA093iA12p14343.

Holappa, L., et al. (2014), Annual fractions of high-speed streams from principal component analysis of local geomagnetic activity, *Journal of Geophysical Research: Space Physics*, *119*, doi: 10.1002/2014JA019958.

Horne, R. B., et al. (2005), Wave acceleration of electrons in the van allen radiation belts, *Nature*, *437*, 227–230, doi:doi.org/10.1038/nature03939.

Jacchia, L. G. (1965), Density variations in the heterosphere, *SOA Special Report*, *184*.

Kamide, Y., and G. Rostoker (2004), What is the physical meaning of the ae index?, *American Geophysical Union*, *85*(19).

Kataoka, R., and Y. Miyoshi (2006), Flux enhancement of radiation belt electrons during geomagnetic storms driven by coronal mass ejections and corotating interaction regions, *Space Weather*, *4*, doi:10.1029/2005SW000211.

Kilpua, E., et al. (2017a), Geoeffective properties of solar transients and stream interaction regions, *Space Science Reviews*, *212*, doi:10.1007/s11214-017-0411-3.

Kilpua, E., et al. (2017b), Coronal mass ejections and their sheath regions in interplanetary space, *Living Reviews in Solar Physics*, *14*, doi:10.1007/s41116-017-0009-6.

Koskinen, H. E. J., and E. I. Tanskanen (2002), Magnetospheric energy budget and the espilon parameter, *Journal of Geophysical Research: Space Physics*, *107*, doi:10.1029/2002JA009283.

Kyoto (2020a), Auroral Electrojet (AE) Indices, http://wdc.kugi.kyoto-u.ac.jp/aedir/ae2/onAEindex.html, Accessed 2020-06-15.

Kyoto (2020b), On dst index, http://wdc.kugi.kyoto-u.ac.jp/dstdir/dst2/onDstindex.html, Accessed 2020-06-15.

Kyoto (2020c), Final Dst Index Monthly Plot and Table, http://wdc.kugi.kyoto-u.ac.jp/dst_final/200007/index.html, Accessed 2020-06-15.

Loewe, C. A., and G. W. Prölss (1997), Classification and mean behavior of magnetic storms, *Journal of Geophysical Research: Space Physics*, *102*, doi:10.1029/96JA04020.

Lu, G., et al. (1998), Global energy deposition during the january 1997 magnetic cloud event, *Journal of Geophysical Research: Space Physics*, *103*, doi:10.1029/98JA00897.

Matthes, K., et al. (2017), Solar forcing for cmip6, *Geoscientific Model Development*, *10(6)*, 22472302, doi:10.5194/gmd-10-2247-2017.

Millan, R. M., and R. M. Thorne (2007), Review of radiation belt relativistic electron losses, *Journal of Atmospheric and Solar-Terrestrial Physics*, *69*, 362–377, doi:10.1016/j.jastp.2006.06.019.

NOAA (2020), Auroral Electrojet (AE, AL, AO, AU) - A Global Measure of Auroral Zone Magnetic Activity - Data.gov, https://catalog.data.gov/dataset/auroral-electrojet-ae-al-ao-au-a-global-measure-of-auroral-zone-magnetic-activity, Accessed 2020-06-15.

Ødegaard, L.-K. G., et al. (2017), Energetic electron precipitation in weak to moderate corotating interaction region driven storms, *Journal of Geophysical Research: Space Physics*, *122*, doi:10.1002/2016JA023096.

Onsager, T. G., et al. (2001), Reconnection at the high-latitude magnetopause during northward interplanetary magnetic field conditions, *Journal of Geophysical Research: Space Physics*, *106*, doi:10.1029/2000JA000444.

Østgaard, N., et al. (2002a), Energy analysis of substorms based on remote sensing techniques, solar wind measurements, and geomagnetic indices, *Journal of Geophysical Research: Space Physics*, *107*, doi:10.1029/2001JA002002.

Østgaard, N., et al. (2002b), A relation between the energy deposition by electron precipitation and geomagnetic indices during substorms, *Journal of Geophysical Research: Space Physics*, *107*, doi:10.1029/2001JA002003.

Richardson, I. G., and H. V. Cane (2012), Near-earth solar wind flows and related geomagnetic activity during more than four solar cycles (1963-2011), *J. Space Weather Space Climate*, *2*, doi:10.1051/swsc/2012003.

Russell, C. T. (1993), Magnetic fields of the terrestrial planets, *Journal of Geophysical Research: Planets*, *98*, doi:10.1029/93JE00981.

Sandanger, M. I., et al. (2015), In-flight calibration of noaa poes proton detectors - derivation of the meped correction factors, *Journal of Geophysical Research: Space Physics*, *120*, 9578–9593, doi:10.1002/2015JA021388.

Seppälä, A., et al. (2014), What is the solar influence on climate? overview of activity during cawses−||, *Progress in Earth and Planetary Science*, *1*, doi:10.1186/s40645-014-0024-3.

Siscoe, G. L., et al. (1968), Relation between geomagnetic sudden impulses and solar wind pressure changes - an experimental investigation, *Journal of Geophysical Research*, *73*, doi:10.1029/JA073i015p04869.

Smith, A. K. (2012), Interactions between the lower, middle and upper atmosphere, *Space Sci Rev*, *168*, doi:10.1007/s11214-011-9791-y.

Smith, E. J. (2001), The heliospheric current sheet, *Journal of Geophysical Research: Space Physics*, *106*, doi:10.1029/2000JA000120.

Søraas, F., et al. (2018), Noaa poes and metop particle obervations during the 17 march 2013 storm, *Journal of Atmospheric and Solar-Terrestrial Physics*, *177*, 115–124, doi:10.1016/j.jastp.2017.09.004.

SpaceWeatherLive (2020), The kp-index, https://www.spaceweatherlive.com/en/help/the-kp-index, Accessed 2020-06-15.

Tanskanen, E. I., and Ilmatieteen laitos (Finland) (2002), *Terrestrial substorms as a part of global energy flow.*, Finnish Meteorological Institute.

Tenfjord, P., and N. Østgaard (2013), Energy transfer and flow in the solar wind-magnetosphere-ionosphere system: A new coupling function, *Journal of Geophysical Research: Space Physics*, *118*, doi:10.1002/jgra.50545.

Thorne, R. M. (1980), The importance of energetic particle precipitation on the chemical composition of the middle atmosphere, *Pure and applied geophysics*, *118*, 128–151, doi:https://doi.org/10.1007/BF01586448.

Thorne, R. M. (2010), Radiation belt dynamics: The importance of wave-particle interactions, *Journal of Geophysical Research: Space Physics*, *37*, doi:10.1029/2010GL044990.

Turunen, E., et al. (2009), Impact of different energies of precipitation particles on no_x generation in the middle and upper atmosphere during geomagnetic storms, *Journal of Atmospheric and Solar-Terrestrial Physics*, *71*, 1176–1189, doi:10.1016/j.jastp.2008.07.005.

Tyssøy, H. N., et al. (2016), Energetic electron precipitation into the middle atmosphere - constructing the loss cone fluxes from meped poes, *Journal of Geophysical Research: Space Physics*, *121*, doi:10.1002/2016JA022752.

Tyssøy, H. N., et al. (2019), Intercomparison of the poes/meped loss cone electron fluxes with the cmip6 parametrization, *Journal of Geophysical Research: Space Physics*, *124*, doi:10.1029/2018JA025745.

van de Kamp, M., et al. (2016), A model providing long-term data sets of energetic electron precipitation during geomagnetic storms, *Journal of Geophysical Research: Atmospheres*, *121*, doi:10.1002/2015JD024212.

Yando, K., et al. (2011), A monte carlo simulation of the noaa poes medium energy proton and electron detector instrument, *Journal of Geophysical Research: Space Physics*, *116*, doi:10.1029/2011JA016671.

Yuan, C. J., and Q. Zong (2012), Quantitative aspects of variations of 1.5 - 6.0 mev electrons in the outer radiation belt during magnetic storms, *Journal of Geophysical Research: Space Physics*, *117*, doi:10.1029/2011JA017346.

Zell, H. (2015a), What is a solar flare?, https://www.nasa.gov/content/goddard/what-is-a-solar-flare, Accessed 2020-06-15.

Zell, H. (2015b), What is a coronal mass ejection or CME?, https://www.nasa.gov/content/goddard/what-is-a-coronal-mass-ejection, Accessed 2020-06-15.

Zhang, Y., et al. (2008), Statistical analysis of corotating interaction regions and their geoeffectiveness during solar cycle 23, *Journal of Geophysical Research: Space Physics*, *113*, doi: 10.1029/2008JA013095.